Measurement of Electron Parameters using Thomson Scattering

Dissertation
zur Erlangung des Doktorgrades
an der Fakultät für Mathematik, Informatik und Naturwissenschaften
Fachbereich Physik
der Universität Hamburg

vorgelegt von

Simon Gerd Bohlen

Hamburg

2020

Gutachter der Dissertation:	Dr. Jens Osterhoff Prof. Dr. Brian Foster
Zusammensetzung der Prüfungskommission:	Dr. Jens Osterhoff Prof. Dr. Brian Foster Dr. Bernhard Schmidt Prof. Dr. Gudrid Moortgat-Pick Prof. Dr. Daniela Pfannkuche
Vorsitzende der Prüfungskommission:	Prof. Dr. Daniela Pfannkuche
Datum der Disputation:	20.11.2020
Vorsitzender Fach-Promotionsausschuss PHYSIK:	Prof. Dr. Günter H. W. Sigl
Leiter des Fachbereichs PHYSIK:	Prof. Dr. Wolfgang Hansen
Dekan der Fakultät MIN:	Prof. Dr. Heinrich Graener

"Ich habe intensiv meine Zeit wirklich im letzten Jahr dem gewidmet, einen guten Überblick zu bekommen und intensiv die Themen auch aufzunehmen, die diese umtreiben."

– Anja Karliczek, Bundesministerin für Bildung und Forschung

Abstract

Laser-plasma acceleration (LPA) [1] offers acceleration gradients several orders of magnitude higher than in conventional radio-frequency accelerators, enabling the acceleration of electrons to hundreds of MeV in just a few millimetres. These small-scale accelerators and in particular X-rays generated from LPA electron beams could potentially be used in material science or medicine [2]. However, LPAs are not commercially used yet, partly because repetition rate and shot-to-shot beam stability are not sufficient for industrial or medical applications and the investigation of the long-term stability on the order of several hours required for the industrial use of LPA has only just started [3, 4].

In this thesis, an electron source was developed to match parameters required for the use of LPA in X-ray fluorescence imaging experiments [5–7]. To generate stable electron beams, self-truncated ionisation injection using a weakly relativistic laser was experimentally implemented for the first time [8]. The long-term stability of these beams was investigated in an 8 hour run at a repetition rate of 2.5 Hz, resulting in a total of 72000 acceleration events. During this time, the average charge stayed constant while the mean energy decreased by 7 percent, showing the necessity to further investigate long-term stability LPA, as such a drift would likely not have been detectable from the only tens to hundreds of shots that are usually considered.

Furthermore, a new diagnostic technique based on Thomson scattering [9] was developed, which offers the first in-situ measurement of electron parameters during the acceleration inside the wakefield. Using this technique, the electron-energy evolution was measured inside the plasma, showing an energy increase from 35 MeV to 61 MeV over a distance of 400 µm. The results agree well with particle-in-cell simulations and were used to study the dephasing of the electron bunch inside the accelerator. By combining measurements and simulations, the influence of the laser strength parameter on the dephasing length could be isolated, showing the power of this method.

This newly developed diagnostic technique could be transferred to other electron parameters such as divergence or emittance [10–12] to obtain a full picture of the electron bunch during acceleration. This could help to study experimentally issues of LPA such as emittance growth and increase the stability of electron beams from plasma accelerators. In combination with further long-term stability studies, these measurements could help to transfer LPA from proof-of-principle experiments to X-ray sources for a broad range of applications.

Zusammenfassung

Laser-Plasma-Beschleunigung (LPB) [1] erlaubt Beschleunigungsgradienten, die mehrere Größenordnungen höher sind, als in konventionellen Hochfrequenzbeschleunigern. So ermöglicht sie die Beschleunigung von Elektronen auf mehrere hundert MeV in wenigen Millimetern. Diese Miniaturbeschleuniger und insbesondere Röntgenstrahlung, die von LPB stammt, könnten für verschiedenste Anwendungen in der Materialwissenschaft oder der Medizin genutzt werden [2]. Allerdings wird LPB noch nicht kommerziell genutzt, unter anderem, weil die Wiederholungsrate und Strahlqualität noch nicht für industrielle oder medizinische Anwendungen ausreicht. Zudem haben Untersuchungen der Langzeitstabilität über mehrere Stunden, die für die industrielle Nutzung von LPB benötigt wird, gerade erst begonnen [3, 4].

Im Rahmen dieser Thesis wurde eine Elektronenquelle entwickelt, die genutzt werden kann, um LPB für Röntgenfluoreszenzbildgebung zu testen [5–7]. Um stabile Elektronenpakete zu erzeugen, wurde zum ersten Mal selbstkürzende Ionisierungsinjektion mit einem schwach relativistischen Laser experimentell umgesetzt [8]. Die Langzeitstabilität der Elektronen wurde über einen Zeitraum von acht Stunden bei einer Wiederholungsrate von 2.5 Hz untersucht. Die Durschnittsladung dieser 72 000 Strahlen blieb dabei konstant, während die mittlere Energie um sechs Prozent abgesunken ist. Dies zeigt die Notwendigkeit weiterer Langzeitstudien auf, da diese Verringerung der Energie nicht mit einigen zehn oder hundert Schüssen messbar gewesen wäre, die normalerweise betrachtet werden.

Zudem wurde eine neue Elektronendiagnostik auf Basis von Thomson-Streuung [9] entwickelt, die als erste die Messung von Elektronenparametern während der Beschleunigung im Kielfeld ermöglicht. Mit dieser Methode konnte die Entwicklung der Elektronenenergie über eine Länge von 400 µm im Plasma gemessen werden, die sehr gut mit Simulationen übereinstimmt. Die Messung wurde genutzt, um die Dephasierung des Elektronenstrahls im Beschleuniger zu untersuchen, was die Nützlichkeit der Methode aufzeigt.

Die neu entwickelte Diagnosetechnik könnte auch auf andere Elektronenparameter wie die Divergenz oder die Emittanz [10–12] erweitert werden, um ein ganzheitliches Bild des Elektronenstrahls während der Beschleunigung zu erhalten. Dies könnte helfen, um Probleme von LPB wie Emittanzsteigerung experimentell zu untersuchen und so die Stabilität der Elektronenstrahlen von Kielfeldbeschleunigern zu erhöhen. Zusammen mit weiteren Langzeitstabilitätsstudien könnte dies helfen, LPB für eine Vielzahl von industriellen und medizinischen Anwendungen zu nutzen.

Contents

List of Figures

Chapter 1

Introduction

People-made particle accelerators have been around for more than 150 years when *cathode rays* were first generated in vacuum tubes such as the Geissler or Crookes tubes [13]. While only reaching electron energies of tens of kiloelectronvolts or less, these accelerators were immediately used for new scientific advances such as the discovery of X-rays by Röntgen in 1895 [14] or the discovery of the first fundamental particle - the electron - by Thomson in 1897 [15]. While accelerators have increased in size and complexity, they still enable such important discoveries in physics today. State-of-the-art radio-frequency (RF) particle accelerators such as the LHC at CERN or XFEL at DESY use acceleration gradients on the order of tens of megavolts per metre to accelerate protons or electrons over several kilometres to detect new fundamental particles such as the Higgs boson, or to produce ultra-brilliant X-ray beams, respectively. In addition to their use in fundamental research, particle accelerators are now widely used in medical and industrial applications, for example in the form of X-ray tubes, which have the same fundamental working principle as the tubes used by Röntgen.

As the maximum acceleration gradient achievable using RF technology is currently limited to about 100 MV/m [16], further increases in energy require alternative acceleration techniques to limit the cost and size of new accelerators. In 1979, laser-plasma acceleration (LPA) was proposed by Tajima and Dawson [1], predicting acceleration gradients in excess of 100 GV/m in a plasma. Advances in laser technology in the following years such as the development of chirped-pulse-amplification (CPA) [17] enabled to reach laser intensities required for this acceleration technique.

Since the first demonstration of quasi-monoenergetic electron beams using LPAs in 2004 [18–20], the field of plasma acceleration has made a lot of progress. The energy-frontier has been pushed further and further [21–23], now reaching energies of almost 10 GeV in only 27 cm of acceleration distance [24]. The electron beams and X-rays generated from LPA sources have large potential for applications in many fields [2]. An example is Thomson scattering (TS) [9], the scattering of an electron and a low-energy photon (in the rest frame of the electron) resulting in an X-ray, which can be used with LPA electrons for X-ray fluorescence imaging (XFI) [25]. In XFI, characteristic fluorescence photons are detected to identify elements such as gold within an object. As conventional X-ray tubes cannot provide the narrow bandwidths required for XFI it is currently investigated using

large synchrotrons [5]. The use of LPA could therefore substantially shrink the size of an accelerator required for this medical-imaging technique, offering the possibility to install such a device at any hospital [6, 7].

Despite the potential for LPA in many fields, the technology is not yet used industrially. A main reason is that the stability of LPA sources on long and short timescales needs improvement. Long-duration stability studies of LPAs required for applications have only just started [3, 4] and further work on this topic is required. In addition, the shot-to-shot stability of plasma accelerators does not yet match the stability of conventional accelerators. Here, more research of the processes inside the plasma is required. Currently, this is done using particle-in-cell simulations, as available diagnostic techniques only measure the final state of the accelerated electron bunches [26]. To study the electron bunches experimentally during the acceleration inside the wakefield, new diagnostic techniques need to be developed.

In this thesis, the long-term and shot-to-shot stability of LPA electrons is investigated. In an 8 hour test with a total of 72000 consecutive shots, the stability of an electron source optimised for the operation of XFI was monitored. In addition, a non-invasive measurement of the electron energy using Thomson scattering was used for the first time in the context of plasma accelerators to study the electrons inside the wakefield. This technique was then extended to measure the electron energy evolution inside the plasma without changing the final state of the produced electron bunches.

The thesis is structured as follows. In Chapter 2, the basics of plasmas and the fundamental principles of LPA are described. Afterwards, the FLASHForward project is described in Chapter 3 with a focus on the laser system and the BOND laboratory used for the LPA experiments. An optimisation of the electron bunches towards parameters required for XFI and results of the 8 hour stability test are presented in Chapter 4. The development of a non-invasive electron diagnostic based on Thomson scattering and the in-situ measurement of the electron evolution inside the wakefield are described in Chapter 5. Finally, a summary of the work and an outlook for further experiments based on the results can be found in Chapter 6.

Chapter 2

Plasmas and acceleration

In this chapter, the foundations of plasmas and the basics of plasma acceleration are described. This is done with respect to theoretical considerations required for the understanding of this thesis. The theory of plasma acceleration presented here is therefore restricted to laser-plasma acceleration and to the parameter space used for the described experiments. For a more complete theory of plasmas and plasma acceleration please refer to standard textbooks and journal articles such as [1, 27–32], which were also used for the writing of this chapter.

2.1 Basics of plasmas

In the most general terms, a plasma is defined as an overall electrically neutral gas in which ions and electrons exist separately [27]. For the use of plasmas as an accelerator, a more strict definition of a plasma is needed, which is presented in this section. This section closely follows previous work done on the topic [33].

2.1.1 Debye length and plasma parameter

An important parameter for the length scales of plasmas is the Debye length, a measure of the length at which charges shield each other and the electric potential drops to $1/e$ [28]. The Debye length is defined as [29]

$$\lambda_D = \sqrt{\frac{\epsilon_0 k_B}{e^2}\left(\frac{n_e}{T_e} + \sum_i^N \frac{Z_i n_i}{T_i}\right)^{-1}}, \tag{2.1}$$

where ϵ_0 is the vacuum permittivity, e is the elementary charge and k_B is the Boltzmann constant. The parameters n_e and T_e and n_i and T_i are the density and temperature of the electrons and ions respectively and N is the number of ion types. The charge of the ions is given by Z_i.

Using the Debye length, we can give a measure for the number of particles of species x with density n_x in a Debye sphere as [27]

$$\Lambda = \frac{4\pi}{3} n_x \lambda_D^3. \tag{2.2}$$

The parameter Λ is called the plasma parameter and allows two cases to be distinguished. First, for $\Lambda \ll 1$, the particles are strongly coupled and there is no collective behaviour, as the motion of particles is dominated by scattering. In the second case of $\Lambda \gg 1$, the Debye sphere is densely populated and collective behaviour is more important than scattering events. Only in this second, weakly coupled case, it is possible to speak of a plasma [28, 34].

2.1.2 Plasma frequency

A small displacement $\delta\vec{x}$ of an electron slice with an area A_{dis} against the ion background will result in a restoring force on these particles. This has the form $\vec{F_r} = -q_{dis}\vec{E_r} = -m_{dis}\ddot{\delta\vec{x}}$, where $q_{dis} = -en_eA_{dis}|\delta\vec{x}|$ is the displaced charge, and m_e is the rest mass of the electron,such that $m_{dis} = m_en_eA_{dis}|\delta\vec{x}|$is the total displaced mass. According to Gauss' Law it follows that $|\vec{E_r}| = \epsilon_0^{-1}\sigma$, with $\sigma = -en_e|\delta\vec{x}|$ being the surface charge density. This leads to the following equation of motion:

$$\frac{d^2}{dt^2}|\delta\vec{x}| + \frac{e^2n_e}{m_e\epsilon_0}|\delta\vec{x}| = 0. \tag{2.3}$$

This equation of motion describes an harmonic oscillator with the frequency

$$\omega_p = \omega_{p,e} = \sqrt{\frac{e^2n_e}{m_e\epsilon_0}}. \tag{2.4}$$

This frequency is called the plasma frequency and is a measure for the typical time scales τ_e for collective behaviour in a plasma [34, 35].

For the ions of the plasma background, the frequency can be derived similarly resulting in $\omega_{p,i} = \sqrt{(e^2n_i)/(Z_im_i\epsilon_0)}$. However, as the ion mass is much higher, the ions react more slowly, which is why their motion is usually neglected [28].

2.1.3 Definition of plasmas

With the parameters introduced above, it is now possible to state three conditions a plasma must satisfy [27]

1. quasi neutrality, meaning that the length scale of the plasma L must be larger than the Debye length ($\lambda_D \ll L$).

2. domination of collective effects over single-scattering events ($\Lambda \gg 1$).

3. domination of collective effects with respect to collisions with neutral atoms that happen on time scales τ ($\omega_p\tau > 1$).

2.2 Plasma acceleration

Inside a plasma as defined above, the acceleration of electrons is possible with acceleration gradients several orders of magnitude higher than in radio frequency (RF) accelerators. One possibility to create such gradients is to use a laser as a driver of a wakefield inside the plasma. This concept was first introduced by Tajima and Dawson in 1979 [1]. For laser-plasma acceleration (LPA) high-intensity lasers are required with a normalised vector potential of the laser field on the order of one. The normalised vector potential, also called laser strength parameter is defined as $a_0 = eA/m_e c^2$, where c is the vacuum speed of light. a_0 is related to the peak laser intensity I_0 as [32]:

$$a_0^2 = 7.3 \times 10^{-19} [\lambda(\mu m)]^2 I_0(W/cm^2), \tag{2.5}$$

where λ is the laser wavelength. A laser inside a plasma will push away electrons from its beam path due to the ponderomotive force of the laser beam, which is proportional to the intensity gradient:

$$F_p = -m_e c^2 \nabla a_0^2/2. \tag{2.6}$$

The electrons are expelled towards regions of low intensity (away from the laser axis), leaving the heavier ions behind due to their higher mass as described in Sec. 2.1.2.

After the laser has passed, the electrons are pulled back, leading to an oscillatory motion of the electrons with the frequency ω_p, introduced in Eq. 2.4. The result is a plasma wave, which can sustain electric fields in excess of $E_0 = cm_e\omega_p/e$ [32] or

$$E_0(V/m) \approx 96\sqrt{n_0(cm^{-3})}. \tag{2.7}$$

Eq. 2.7 is referred to as the cold nonrelativistic wave-breaking field [36]. For a plasma density of $n_0 = 10^{18} cm^{-3}$, Eq. 2.7 leads to an accelerating field of 96 GV/m, exceeding the maximum gradients in RF accelerators by more than three orders of magnitude. The length of this plasma wave is approximately the plasma wavelength $\lambda_p = 2\pi c/\omega_p$. The plasma wavelength can be linked to the plasma density via [32]

$$\lambda_p(\mu m) \approx 3.3 \times 10^{10}/\sqrt{n_0(cm^{-3})}. \tag{2.8}$$

For the density given before, this leads to a length of the accelerating wave of approximately 30 µm. The duration of electron bunches accelerated in a plasma wave is therefore intrinsicly on the order of femtoseconds. In addition to these longitudinal accelerating fields, transverse fields focus an electron beam that is located in a region of low electron density [32].

The generated density profile and corresponding fields of a laser wakefield accelerator can be simulated as will be described in the following section. An example of a simulation of a linear plasma wave driven by a laser with a laser strength parameter $a_0 = 0.5$ is

depicted in Fig. 2.1.

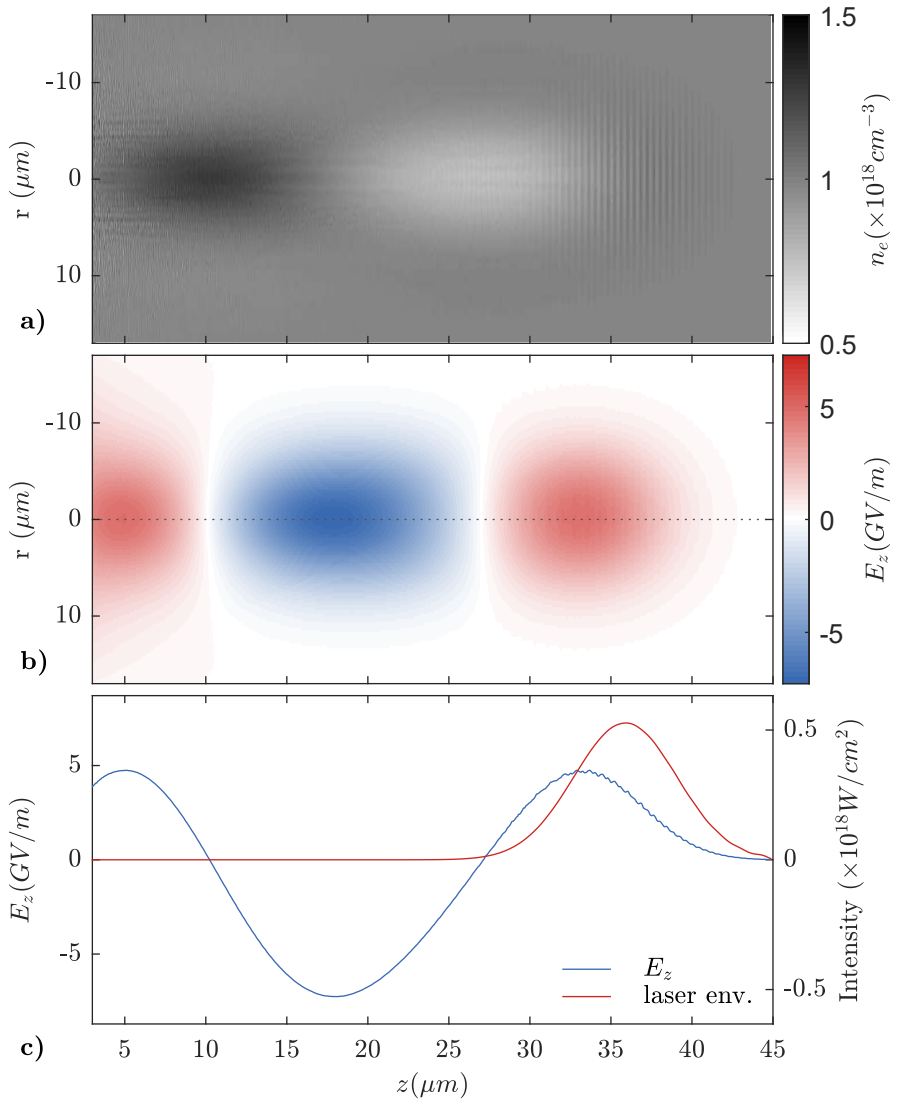

Figure 2.1: FBPIC simulation of a laser with a normalised peak intensity of $a_0 = 0.5$ driving a linear wakefield in a plasma with a density of $1 \times 10^{18}\,\mathrm{cm}^{-3}$. (a) Resulting electron density, (b) longitudinal electric fields and (c) on axis lineout (marked as dashed line in (b)) of the longitudinal field and the laser field envelope.

In the simulation, the laser driver located at $z = 50\,\mu\mathrm{m}$ pushed electrons away from the axis, leading to a lower electron density as is shown in Fig. 2.1a. After the laser has passed, the electrons are pulled back, resulting in an increased density at a distance of one wavelength behind the laser pulse. This electron distribution leads to a roughly sinusoidal electric field on axis (Fig. 2.1c) with a frequency of ω_p.

In case of a laser strength parameter $a_0 >> 1$, the laser pushes away all electrons from the axis, leading to the so-called bubble regime [37]. The resulting plasma wakefield is non-linear, as depicted in Fig. 2.2.

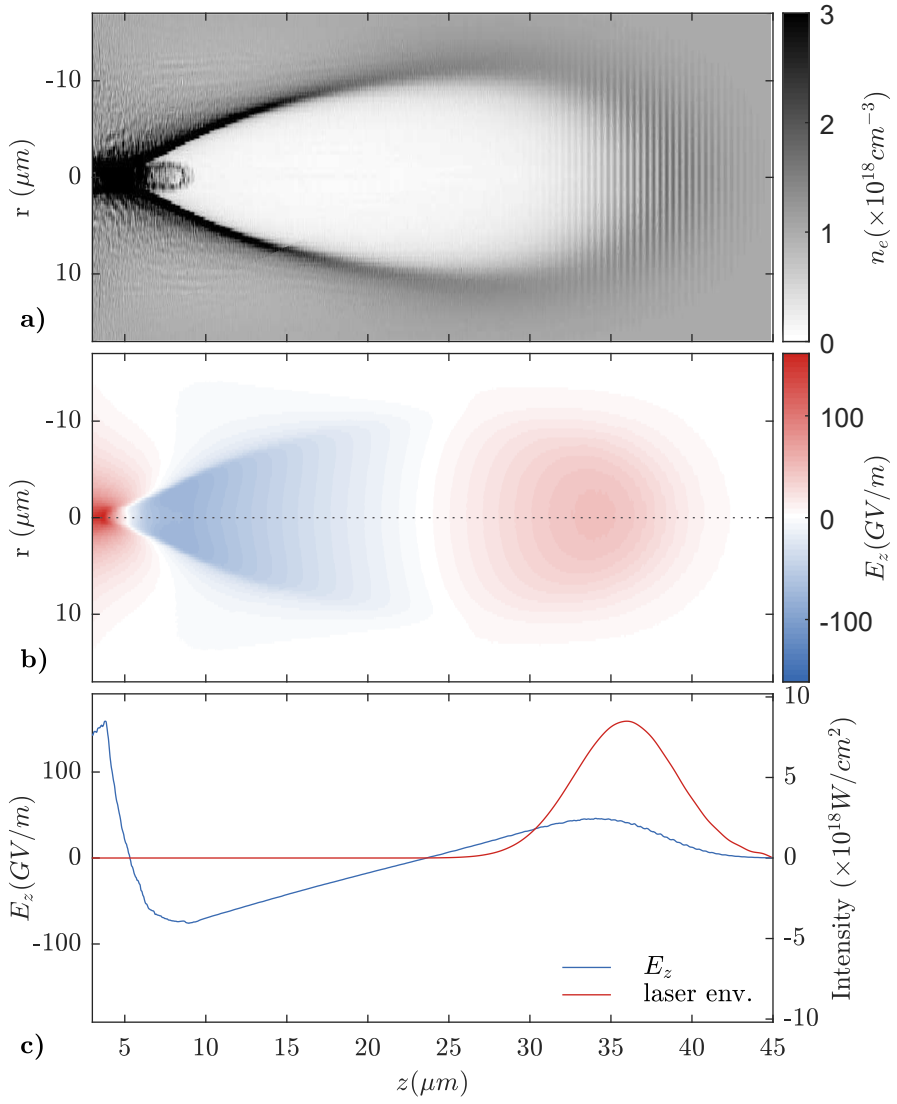

Figure 2.2: FBPIC simulation of a laser with a normalised peak intensity of $a_0 = 2.0$ driving a non-linear wakefield in a plasma with a density of $1 \times 10^{18}\,\mathrm{cm}^{-3}$. (a) Resulting electron density, (b) longitudinal electric fields and (c) on axis lineout (marked as dashed line in (b)) of the longitudinal field and the laser field envelope.

Analogous to the driving of a wakefield using an intense laser pulse, a plasma wave can also be driven by the space charge of an electron beam [38, 39]. This beam-driven acceleration scheme is employed at the FLASHForward facility [40, 41] using an electron beam from the FLASH accelerator as a driver. While the theory of beam-driven plasma acceleration is not described in this thesis in more detail, a short description of the FLASHForward experiments can be found in the Appendix in Chapter C.

2.3 Particle-in-cell simulations

As seen above, particle-in-cell (PIC) simulations are a useful tool to study the acceleration process inside a plasma. PIC codes simulate the interaction of charged particles and electromagnetic fields, making them a powerful way of mimicing plasma-based acceleration. In this thesis, the PIC code FBPIC (**F**ourier-**B**essel **P**article-**I**n-**C**ell) [42–45] was used. As in other PIC codes, charged particles are represented by macroparticles in FBPIC, while the fields are represented on a grid [46]. The time evolution is then simulated in discrete time steps where four calculations are performed:

- The values of the E-field and the B-field are gathered from the grid onto the macroparticles.
- The particles are pushed forward by one time step according to their velocity.
- The charge and the current of the macroparticles are deposited onto the grid representing the fields.
- The E-field and the B-field are incremented in time.

Other than most PIC codes which use a 3D Cartesian grid, FBPIC uses a set of 2D radial grids, which represent azimuthal modes of the 3D problem. This technique is computational advantageous for problems with a close-to-cylindrical symmetry, as is the case in laser wakefield acceleration. Another difference to other PIC codes lies in the solving of the Maxwell equations. Often, Maxwell's equations are discretized using finite-difference methods, which can lead to numerical artefacts such as emittance growth [47], numerical Cherenkov effects [48] or erroneous dephasing-length prediction [49]. In FBPIC, the fields are solved in spectral space, which allows a more precise evaluation of the derivations and an analytical integration of Maxwell's equations. In contrast to other codes, this can make FBPIC dispersion-free in all directions and intrinsically frees the code of numerical Cherenkov instabilities by using co-propagating Galilean coordinates. In addition, the spectral algorithms have better stability in Lorentz-boosted frame simulations, which can be several orders of magnitude faster compared to laboratory-frame simulations [50]. Due to these advantages of FBPIC, especially the low computational costs of simulations compared to other codes, it was chosen for all PIC simulations in this thesis.

2.4 Injection

To accelerate electron bunches using plasmas, they need to be injected into the accelerating phase of the wakefield. The injection can be achieved with several different techniques, of which four are described here, which were also used in the presented experiments.

2.4.1 Self-injection

Plasma electrons can be trapped in the wakefield, which is called self-injection, as the electrons are generated from within the plasma [37, 51, 52]. The trapping of electrons can be achieved by driving the wakefield beyond the wave-breaking threshold defined in Eq. 2.7. If the wave is driven far beyond this threshold, the wave structure is destroyed and large amounts of charge can be accelerated to high energies but at the cost of a broad energy distribution, as already demonstrated in 1995 [53]. Close to the wave-breaking threshold, electrons from the background plasma can be trapped in the wave without destroying its structure. In this case, narrow energy-spread electron beams can be accelerated in the non-linear wakefield, the so-called bubble regime [37] depicted in Fig. 2.2, at high acceleration gradients. This was experimentally shown in 2004 with the first generation of quasi-monoenergetic beams [18–20].

A downside of self-injection is the difficulty in controlling it. As self-injection is a highly non-linear process, it is very sensitive to laser and plasma parameters. Therefore, small changes can lead to a transition from a single to multiple bunches [54]. Nevertheless, significant improvement of the stability of self-injected beams can be accomplished by stabilisation of experimental parameters, as was shown e.g. by the use of steady-state-flow gas cells [55].

2.4.2 Shock-front injection

A more controlled technique for the injection is shock-front injection[56, 57], which is based on density transitions of the driver beam inside the plasma [58, 59]. The length of the wakefield is inversely proportional to the square root of the plasma density, as was shown in Eq. 2.8. A decreasing plasma density will therefore result in an elongation of the wakefield so that electrons positioned at the back of the wakefield will be trapped. This principle is also depicted in Fig. 2.3. The increased density level is often created using a blade positioned over a gas jet that creates a density shock-wave in the gas and therefore a short density ramp that can be used to inject electrons.

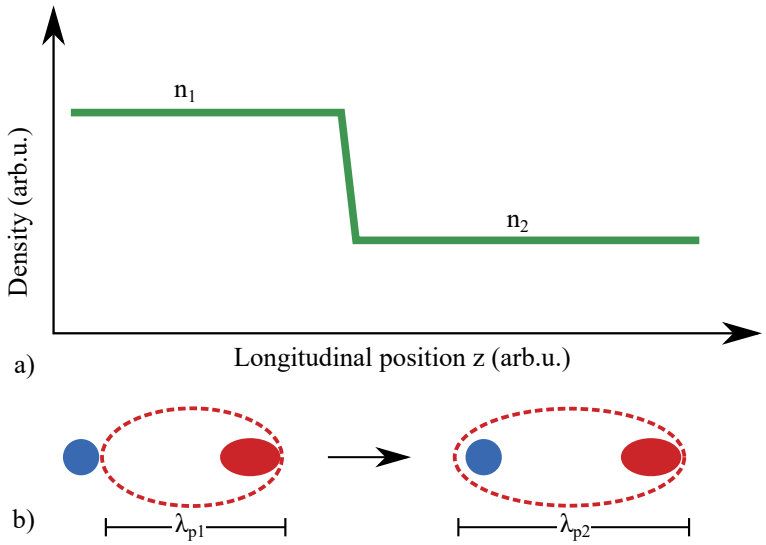

Figure 2.3: The principle of shock-front injection. a) density profile with two density levels n_1 and n_2 with a steep transition between the two levels. b) a laser (red circle) drives a wakefield (red dashed line) with a plasma wavelength of λ_{p1}, accumulating electrons at the back (blue circle). After undergoing the density transition from n_1 to n_2, the plasma wavelength increases to λ_{p2} and the electrons from the back of the wakefield are injected into it.

2.4.3 Ionisation injection

Another controlled technique to inject electrons is ionisation injection (II) [60–62]. Here, the gas being ionised usually consists of two gas species and therefore multiple ionisation states. The lower ionisation states will be ionised by the leading edge of the laser pulse, forming the background plasma. To ionise the higher states, more laser intensity is required. Therefore, these states can only be ionised by the high-intensity peak of the pulse. Electrons that are ionised near the high-intensity peak of the laser will be trapped inside the wakefield rather than being expelled if the wakefield is driven sufficiently high. It was shown that this process requires an a_0 of 1.7 or larger in the case of nitrogen [62].

Nitrogen is a good candidate as a doping gas in hydrogen or helium as can be shown by a calculation of the intensities required for ionisation of these elements. The required intensity for an ionisation level (Z_{ion}) can calculated from the binding energies (E_{bind}) of the elements via [63]:

$$I = 4 \times 10^9 \frac{E_{bind}^4(eV)}{Z_{ion}^2}. \tag{2.9}$$

While Eq. 2.9 was derived for noble gases, it has been found through experimental studies to also apply to other gases e.g. nitrogen [64]. Using literature values for the binding energies [65], the intensities required for the ionisation of hydrogen, helium and nitrogen can be calculated from Eq. 2.9. These are listed in Tab. 2.1. As can be seen in the table, hydrogen and helium as well as the five outer electrons from nitrogen require intensities on the order of $1 \times 10^{16}\,\mathrm{W\,cm^{-2}}$ or below to be ionised and would consequently be ionised

Element	Ion	$E_{bind}(eV)$	Intensity (W/cm^2)
Hydrogen	H^+	13.6	1.37×10^{14}
Helium	He^+	24.6	1.46×10^{15}
	He^{2+}	54.4	8.76×10^{15}
Nitrogen	N^+	14.5	1.77×10^{14}
	N^{2+}	29.6	7.68×10^{14}
	N^{3+}	47.4	2.24×10^{15}
	N^{4+}	77.5	9.02×10^{15}
	N^{5+}	97.9	1.47×10^{16}
	N^{6+}	552.1	1.03×10^{19}
	N^{7+}	667.0	1.62×10^{19}

Table 2.1: Binding energies and intensities required for ionisation of hydrogen, helium and nitrogen.

from the outer wings of a laser pulse with a peak intensity of $1 \times 10^{18}\,\mathrm{W\,cm^{-2}}$ or more. The inner two electrons of nitrogen on the other hand require intensities of more than $1 \times 10^{19}\,\mathrm{W\,cm^{-2}}$, corresponding well to the required a_0 of 1.7.

Ionisation injection was found to be able to inject and accelerate electrons in a stable way as early experiments using this technique show [66–68]. A downside of the injection technique is the continuous ionisation and trapping of electrons that leads to large energy spread.

2.4.4 Self-truncated ionisation injection

Several proposals have been made to overcome the issue of continuous trapping of ionisation injection while maintaining the stability of the injection technique. Examples are the use of multiple laser pulses [69, 70], tailored density profiles [71], the use of two stages [72] or the combination of ionisation injection and shock-front injection [57]. While these techniques have been shown to be capable of generating narrow energy-spread electron bunches, they complicate the setup.

Another technique to overcome the continuous trapping is self-truncated ionisation injection (STII). Here the injection is truncated via self-focusing of the laser pulse inside the plasma [8, 73]. One possibility for STII is to use an initially unmatched laser spot to ionise the doped gas. In this case, the injection condition breaks due to self-focusing of the laser pulse in the plasma and deformation of the plasma wave, as this process shifts the relative position of the ionised electrons towards the front of the laser pulse [73]. Alternatively, a moderate laser energy ($a_0 \approx 1$) is used that only reaches the required intensity for injection for a short distance inside the plasma due to self-focussing and defocussing [8]. In both cases, the injection distance is limited to a length of typically a few hundred micrometers, enabling the generation of low-energy-spread electron beams.

Stable generation of electron bunches with peaked electron distributions using the former technique was shown in several experiments without further changes to the setup [74–76]. The latter case has not yet been shown experimentally.

2.5 Limits of acceleration

While LPA offers high acceleration gradients, the maximum energy gain achievable in a single acceleration stage is limited by several mechanisms, mainly dephasing, depletion and diffraction, which are described here in more detail.

Dephasing

The phase velocity v_ϕ of the wakefield inside a uniform plasma is defined as the difference of the group velocity of the laser and its etching velocity, which describes the etching of the laser due to local pump depletion at the front of the pulse from driving the wakefield [77, 78]:

$$v_\phi = c\left(1 - \frac{3\omega_p^2}{2\omega^2}\right), \tag{2.10}$$

where c is the speed of light in vacuum; v_ϕ is therefore smaller than the speed of the electron bunch, which is accelerated to relativistic energies very quickly and consequently travels at approximately c inside the plasma. An electron bunch that is initially positioned in the accelerating field of the wake will therefore transition into the decelerating phase. The distance an electron will travel in the laboratory frame whilst shifting from the accelerating field to the zero crossing of the wakefield is called the dephasing length. For a laser-strength parameter on the order of 1, the dephasing length L_{deph} can be estimated by [32]:

$$L_{deph} = \frac{\lambda_p^3}{2\lambda_0^2} \tag{2.11}$$

Acceleration for distances exceeding L_{deph} can be achieved by increasing the phase velocity of the wakefield. Several techniques to overcome the dephasing limit have been proposed and demonstrated. These include density ramps [79, 80], travelling wave acceleration [81], multi-pulse acceleration [82] and advanced focussing optics [83]

Depletion

Another factor limiting the acceleration length of an LPA is pump depletion. While the laser drives a plasma wave, it transfers energy from the laser pulse to the wakefield [32]. If all energy from the laser is transferred to the wakefield, the electrons can no longer be accelerated. Therefore, the pump-depletion length L_{pd} can be estimated by equating the laser pulse energy to the energy left behind in the wakefield. For an a_0 on the order of one, this results in a depletion length of [32]:

$$L_{pd} = \frac{2\lambda_p^3}{\lambda_0^2 a_0^2}. \tag{2.12}$$

In the linear regime, the acceleration length is therefore more limited by the dephasing length than by depletion, unless the phase velocity of the wakefield is increased.

Diffraction

To reach intensities required for the driving of the wakefield the laser is usually focussed into the plasma. In vacuum, the laser pulse will undergo Rayleigh diffraction, increasing its spot size as $r_s(z) = r_0(1 + z^2/Z_R^2)^{1/2}$, where r_0 is the minimum spot size in the focus ($z = 0$) and Z_R is the Rayleigh length describing the distance over which the beam radius has increased by a factor of $\sqrt{2}$ [32]. If no optical guiding for the laser pulse is present, the acceleration distance will therefore be limited to a few Rayleigh lengths.

Chapter 3

Overview of the experimental laboratories

The experiments described in this thesis were conducted at a laser-plasma acceleration (LPA) setup at DESY in Hamburg, Germany. Both laser- and experimental laboratories are situated on top of the **F**ree-electron **LAS**er in **H**amburg (FLASH) accelerator hall. A floorplan of the laboratories and the control room is depicted in Fig. 3.1.

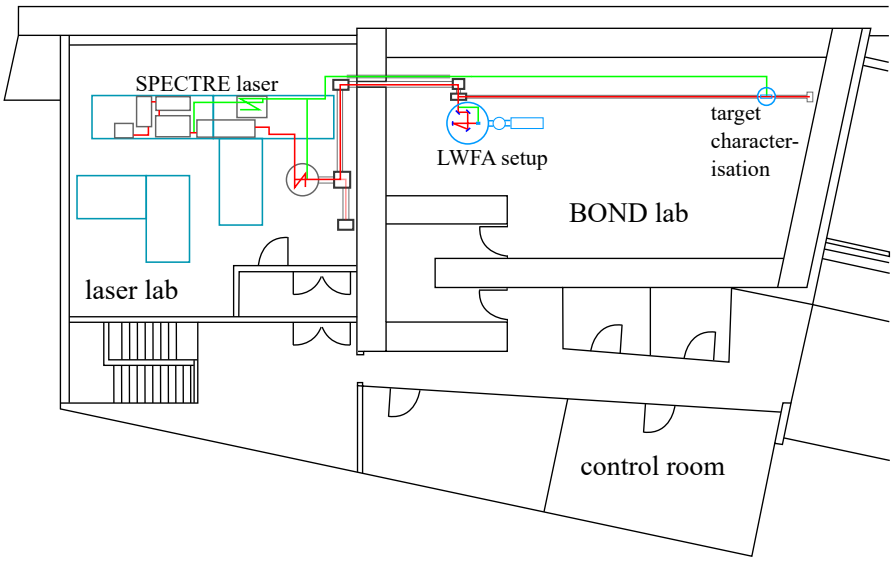

Figure 3.1: Layout of the laser laboratory housing the SPECTRE laser system and the BOND laboratory with the setups for LPA studies and target characterisation. The experiments in the BOND lab are conducted from the control room shown in the bottom of the image.

The laser system used in these experiments is shared with the **F**uture-**OR**iented **W**akefield **A**ccelerator **R**esearch and **D**evelopment at FLASH (FLASHForward) experiment, which conducts beam-driven plasma-wakefield experiments [40, 41]. Despite the author's contributions to several FLASHForward experiments [84–87], the focus of this thesis is on LPA experiments conducted in the context of PLASMED-X, which aims to perform proof-of-principle experiments of X-ray fluorescence imaging (XFI) with an LPA source [5–7]. The laser system used in the experiments and the **B**eam **O**ptimisation and

Novel **D**iagnostics (BOND) laboratory, where the LPA experiments were conducted, are described in this Chapter.

3.1 Laser system

A main component for the LPA experiments described in this work is the SPECTRE laser system, which is also used at FLASHForward for internal-injection experiments and plasma-target characterisation. This section will describe fundamental laser principles followed by specifics of TW-class laser systems - often with respect to the 25 TW laser used for this work. A more general description of ultrashort lasers can be found in literature which was used for writing this chapter [88–90]. Finally, a description of the laser system and its most important parameters and diagnostics used in the experiments is given. The focus is on the use of the laser as a driver in the LPA experiments.

3.1.1 Fundamentals of ultrashort lasers

Laser is an acronym for **l**ight **a**mplification by **s**timulated **e**mission of **r**adiation. The fundamental principle of lasers, the process of stimulated emission of radiation was proposed by Einstein in 1916 [91]. The first experimental demonstration of a laser was achieved in 1960 using ruby as gain material [92].

A laser requires three main components: a gain medium, a pump and an optical resonator. A schematic of a basic laser setup is depicted in Fig. 3.2a. Inside the gain medium, three or more energy levels are required, as can be seen in Fig. 3.2b. The pump will excite electrons in the atoms of the gain medium from the ground state E_0 to an excited state E_3. As this requires the specific energy of the incoming pump photons of $E_3 - E_0 = \hbar\nu_{pump}$, pumping can be done by e.g. another laser or flashlamps. Inside the gain medium, the electrons decay to lower states via non-radiative (thermal) processes to the energy level E_2. From there the electron can decay further to the level E_1 under emission of a photon. This can happen without further influences on the gain medium which is called spontaneous emission. If however a photon with the energy $E_2 - E_1 = \hbar\nu_{laser}$ passes by an exited atom, it will stimulate this process and amplify the light. A passing photon could also be absorbed by the atom to excite an electron from energy level E_1 to E_2. As this process has the same probability as the stimulated emission, a population inversion of the levels E_1 and E_2 is required, meaning more electrons need to be in the higher state E_2 compared to the number of electrons in the lower energetic state E_1, explaining the requirement for three or more energy levels for an optically pumped laser medium. The gain medium is placed between two cavity mirrors to reflect the light back into the gain medium, thereby enabling the amplification of the intensity inside the cavity at each reflection. One of the two mirrors has usually a transmission on the order of a percent to couple out light from the cavity as laser light.

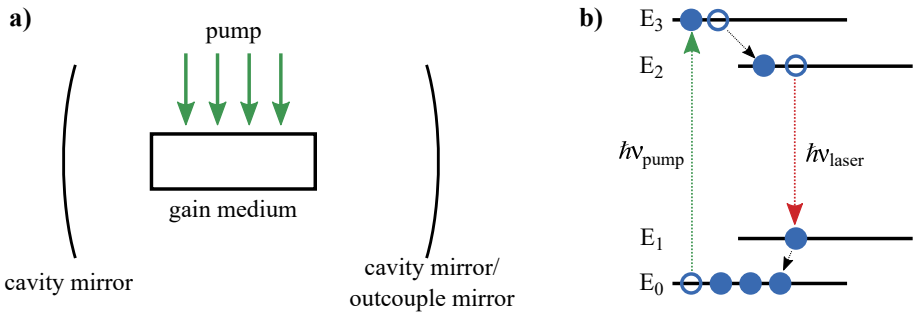

Figure 3.2: Basic principle of a laser. (a) required components for a laser. (b) energy levels in a laser gain medium.

In order to accelerate electrons using laser wakefield acceleration, typically laser intensities on the order of $1 \times 10^{18}\,\mathrm{W/cm^2}$ and more are needed. To produce these intensities, laser systems with peak powers on the order of terawatts to petawatts are required, which often have pulse durations on the order of femtoseconds. As the maximum intensity in the gain medium is limited due to non-linear effects to about $5\,\mathrm{GW\,cm^{-2}}$ [89], the amplification is often done in a stretched pulse. To reach energies on the order of terawatts and more, the stretched pulse is then compressed again after the final amplification stage. This technique is called chirped pulse amplification (CPA) and was introduced by Strickland and Mourou in 1985 [17]. Strickland and Mourou were awarded the Nobel Prize in Physics 'for their method of generating high-intensity, ultra-short optical pulses' in 2018 [93].

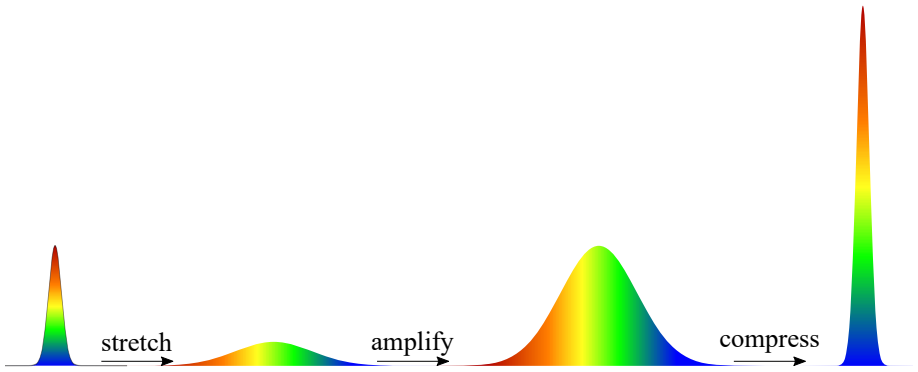

Figure 3.3: Principle of Chirped Pulse Amplification. A short broadband pulse is stretched before amplification and afterwards compressed again to reach high intensities to decrease the intensity inside the laser gain material.

The principle of CPA is based on the wavelength range of short laser pulses and is depicted in Fig. 3.3. Due to Heisenberg's uncertainty principle [94], short laser pulses are required to have a broader wavelength range. For example, a Gaussian laser pulse with a pulse duration of 25 fs and a central wavelength at 800 nm requires a minimal bandwidth of 88 nm [88]. Such a pulse is then called Fourier-limited, as it cannot be compressed further without increasing its bandwidth. As a consequence, only certain laser materials that allow for gain in a broad spectral range can be used. A common example for such

a gain material is titanium sapphire (Ti:Sa) [95]. In CPA, an initially short (few fs) and broad (tens of nm) laser pulse is stretched using a dispersive element e.g. a grating pair, by several orders of magnitude before amplification. The stretched pulse can be amplified without reaching the intensities which would lead to non-linear effects in the laser system. After the final amplification, the pulse is compressed by implementing a negative dispersion to the pulse e.g. using another grating pair. Using this technique, the first laser with similar power to the 25 TW laser system at FLASHForward was reported in 1996 [96].

3.1.2 The SPECTRE laser system

The SPECTRE laser system is set up in a laboratory together with a diagnostics section. An overview plan of the laser laboratory is depicted in Fig. 3.4. The main parts of the system are located on a laser table with a size of about 2 m by 10 m. The final compression of the pulse is done in a compressor tank next to the laser table, from where the laser beam can be sent either to the FLASHForward experiment or into the BOND laboratory. In addition, a laser diagnostic section is situated next to the laser table. A third optics table offers space for small experiments and test setups inside the laser laboratory. The laser system and its most important components, namely oscillator, booster, stretcher, amplifiers and compressors are described in this section, based on the operation manuals [97, 98]. A full drawing of the laser system and its optics is depicted in Fig. 3.5. In addition, some diagnostics and properties of the laser beam will be described in the following.

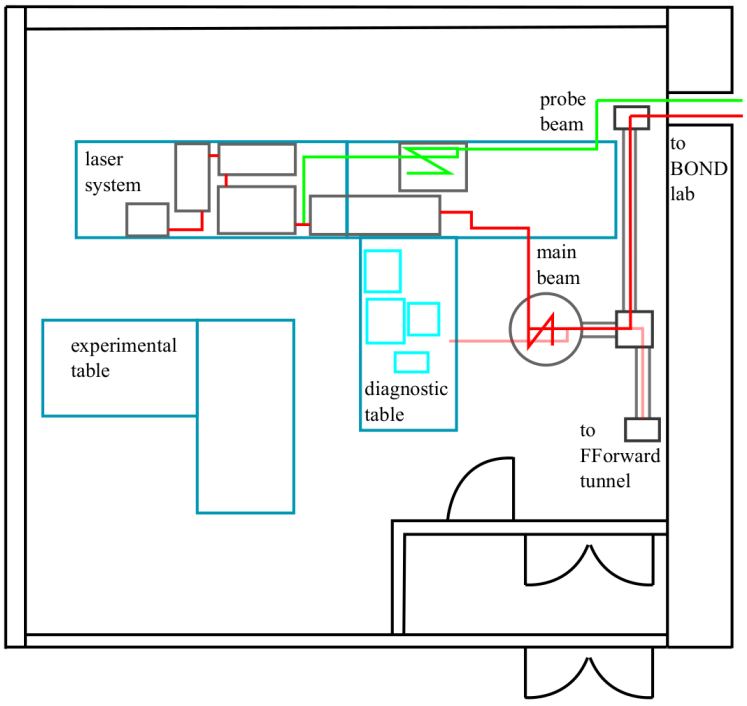

Figure 3.4: Floorplan of the laser laboratory

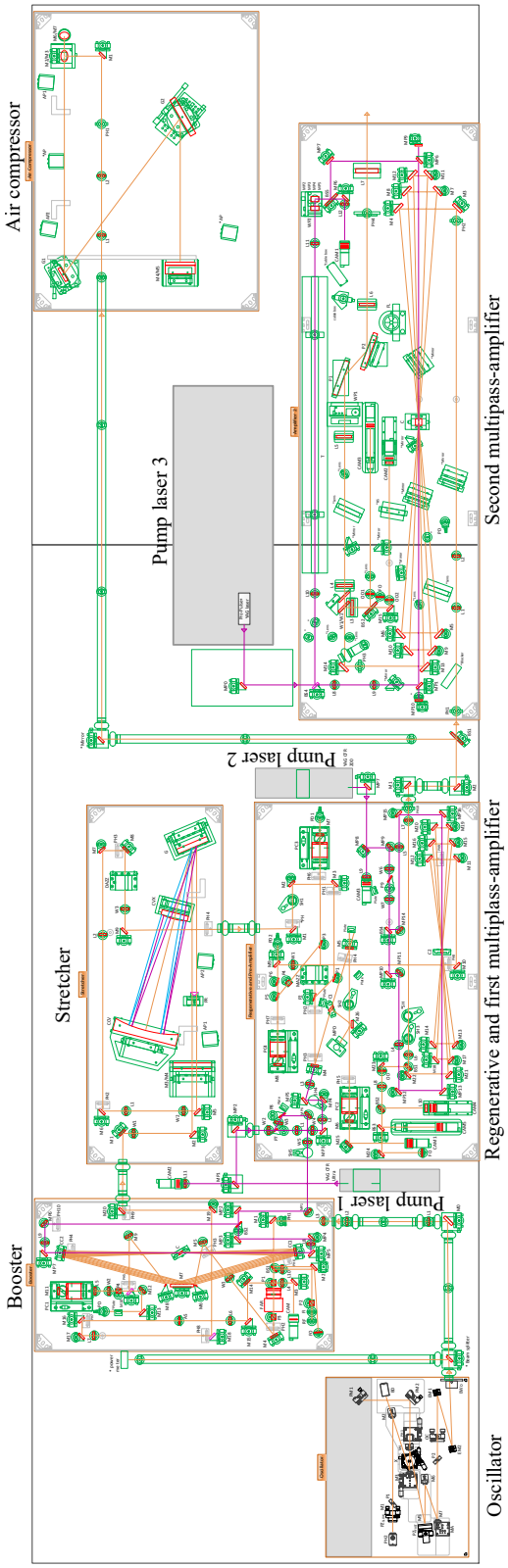

Figure 3.5: Drawing of the SPECTRE laser system.

The initial, spectrally broad pulses come from the oscillator. The beampath of the oscillator is depicted in Fig. 3.6, forming a more complex version of the basic laser setup in Fig. 3.2a. A Ti:Sa crystal is pumped by a 532 nm (frequency doubled) diode laser. The laser cavity is formed by the mirrors M1 to M7 and the out-couple mirror OC. For alignment of the output beam of the cavity, two more mirrors are installed, before the beam leaves the oscillator through a window at the Brewster Angle BWo. The oscillator delivers ultra-short laser pulses rather than continuous wave (CW) via Kerr-lens mode-locking [89]. The Kerr-lens effect is based on the intensity-dependent refractive index of materials. The refractive index n is formed of a constant and a nonlinear term [88, 89]:

$$n = n_0 + \overline{n}_2 I(t) \tag{3.1}$$

The nonlinear component $\overline{n}_2$ in Eq. 3.1 is dependent on the intensity of an electric field (or light wave) and leads to self focussing of a high-intensity laser pulse. Using this effect, the oscillator is designed such that high-intensity pulses are favoured over CW operation and can be mode-locked, leading to a single femtosecond pulse travelling through the oscillator cavity [99, 100]. The repetition rate of these pulses is defined by the round-trip time of the cavity; it is 108 MHz in this case, to enable synchronisation of the laser system to the FLASH accelerator, which is required for several FLASHForward experiments. This synchronisation is done by adjusting the cavity length using the motors PZ_{slow} and PZ_{fast}.

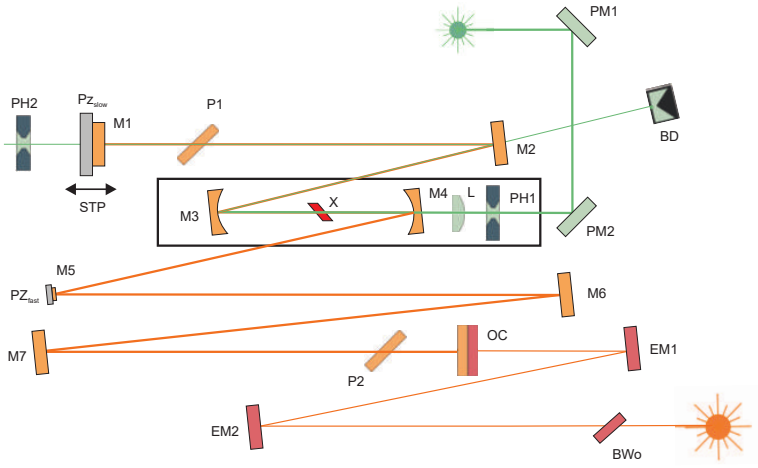

Figure 3.6: Layout of the oscillator [98].

After the oscillator, the pulses go through the Booster unit, where the repetition rate is reduced and the contrast ratio of the pulse is increased. The Booster amplifies the oscillator pulse in a multipass amplifier setup with a total of 14 passes. After 7 passes, the pulses are reflected in a Pockels cell [89], which is able to change the polarisation of a beam using birefringent crystals when applying a high voltage. In combination with a polarizing beamsplitter, this enables the repetition rate to be reduced from the 108 MHz coming from the oscillator to 10 Hz. After the pulse picking and amplification, the pulses are focussed onto a saturable absorber. In the saturable absorber, pre-pulses or continuous background

radiation is absorbed up to a certain intensity threshold, after which the absorber becomes transmissive. This is necessary, since the constant pumping of the oscillator using a CW pump diode leads to amplified spontaneous emission of the oscillator unit [89], which needs to be suppressed for LPA.

The next section of the laser system is the stretcher. In the SPECTRE laser, the stretching of the pulse is done by gratings in a so-called Öffner triplet [101], made of a grating, a concave and a convex mirror. This setup enables abberation-free stretching of the pulse [102, 103]. In addition, an acousto-optic programmable dispersive filter (or Dazzler) is located behind the stretcher. The Dazzler enables control of the spectral phase of the laser pulse. This is done by an acoustic wave generated by an RF signal in a birefringent crystal. Thereby, the Dazzler enables dispersion of later parts of the laser chain to be pre-compensated, allowing for more advanced shaping of the spectral phase.

After the Dazzler, the beam is amplified in three more stages. First, a regenerative amplifier is employed, where the input and output of the amplifying cavity is handled using Pockels cells and polarisers, therefore allowing control of the number of reflections in the cavity. Furthermore, an acousto-optic programmable gain control filter (or Mazzer) is placed in the regenerative amplifier cavity. The Mazzler, works similarly to the Dazzler via acousto-optic waves in a birefringent crystal, but in the case of the Mazzler, the wave is used to flatten the gain curve. This is achieved by diffracting spectral components from the beam to increase losses at spectral regions of high gain. This allows for broader spectra and subsequently short pulses. After the regenerative amplifier, the beam is further amplified in the first multi-pass amplifier stage. The working principle of the first multi-pass amplifier is analogous to the last amplifier stage, which is described below and depicted in Fig. 3.7.

In a next step, the beam is split in a ratio of 80 percent to 20 percent. The latter part is compressed using a grating pair, in the same way as the compression of the main beam is done, which will be discussed later. However, due to the energy in this beam of around 5 mJ, the compression can be done in air, resulting in a beam with a pulse duration of 25 fs and an energy of about 3.5 mJ. The other 80 percent of the beam is widened using a pair of lenses and then amplified in the second and final multipass amplifying stage. A plan view of the second multi-pass amplifier is depicted in Fig. 3.7. Afterwards, the beam size is increased further using another lens pair to its final diameter of about 45 mm. The final magnification of the beam is necessary to reduce the peak-intensity on the optics both inside and subsequent to the compressor and keep the intensity below the damage threshold once the beam is compressed.

The final compression of the main beam is done in a vacuum tank with a diameter of 1.2 m. During the compression, the second- and third-order dispersion introduced by stretcher and amplifier stages can be compensated by requiring two degrees of freedom. In the case of the compressor, these are the angle of incidence on the gratings and the distance between them. After the compression, the leakage of a mirror in the compressor is transferred to the diagnostic table to monitor alignment and to characterise the laser

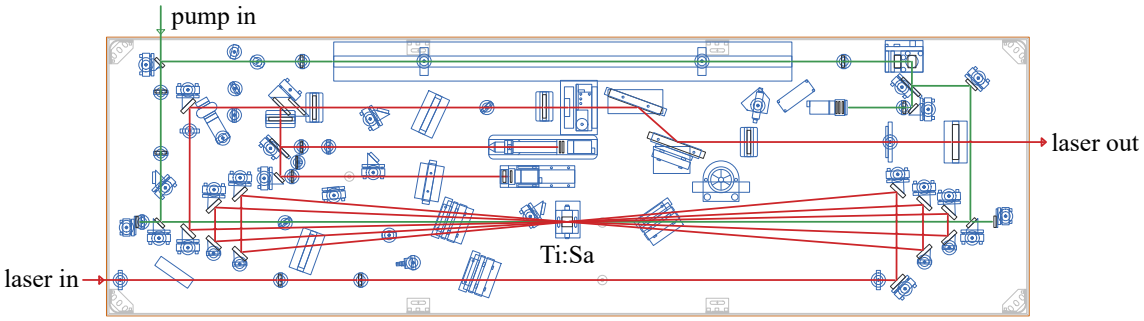

Figure 3.7: Layout of the second multi-pass amplifier stage. A pump laser (green) pumps the Ti:Sa crystal. The incoming laser (red) passes the pumped crystal five times. As no cavity mirrors are used, the intensity inside the crystal is the same intensity the pulse reaches after its final amplification. In addition, several diagnostics for pump and main laser as well as lenses are inside the amplifier.

beam. These diagnostics will be described below. The main part of the compressed beam is transported into a vacuum laser beamline, from where the beam can be sent into the BOND lab or to experiments in the tunnel. An additional laser beamline is set up between the laser and the BOND laboratory to transport the beam from the air compressor into the BOND lab separately.

3.1.3 Laser diagnostics

The laser defines many properties in LPA as described in Chapter 2. Detailed knowledge of the laser and regular maintenance of the laser including an optimisation of its parameters is therefore very important for LPA experiments. The diagnostics used for the monitoring and characterisation of the laser pulse are described in this section.

For the temporal characterisation of the laser pulse, an important measure is the intensity contrast. The contrast is the ratio of the intensity at a time t to the peak intensity of the pulse [104] and needs to be measured on both long timescales (hundreds of picoseconds) and on short timescales on the order of the pulse duration (tens of femtoseconds). For these measurements, a Sequoia [105] and a Wizzler [106] are used respectively. The Sequoia is a third-order cross-correlator that allows the measurement of the background level of amplified spontaneous emission (ASE) or potential pre- and post-pulses of the laser beam [105]. While pre-pulses are especially important in ion acceleration, a low level of ASE is also important for LPA, as was found in the experiments discussed here as well as at other LPA experiments [107]. The working principle of the Sequoia is as follows: the input beam is split into two parts. One part passes a non-linear crystal to generate the second harmonic (SH) of the beam, which functions as a reference of the beam. The SH and the fundamental of the remaining part are then sent through a second non-linear crystal to generate the a sum-frequency wave of the beam. This third harmonic of the fundamental is measured using a photomultiplier tube and compared to the reference beam. To scan the contrast measurements over hundreds of picoseconds, a delay stage is implemented in

the fundamental of the beam. The use of neutral density filters enables a dynamic range of the devices of up to twelve orders of magnitude. A comparison of a contrast measurement using the Sequoia with an optimised alignment of saturable absorber and seed in the regenerative amplifier (therefore reducing the ASE background) and a measurement prior to the optimisation is depicted in Fig. 3.8. In both cases, a post-pulse is visible at about 40 ps. This post-pulse leads to a fake pre-pulse at −40 ps due to the referencing of the post-pulse.

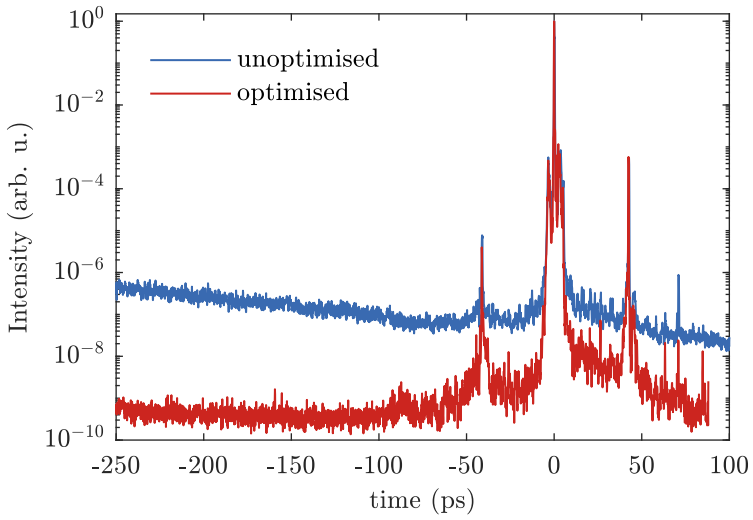

Figure 3.8: Sequoia measurements of an optimised and unoptimised laser pulse. The optimised alignment of contrast booster and amplifiers (red line) increases the background level of amplified spontaneous emission by more than two orders of magnitudes compared to the measurement using a misaligned system. In both cases, a post-pulse is visible at about 40 ps. This post pulse leads to a artificial pre-pulse at −40 ps due to the referencing of the post pulse.

The Wizzler [106] is used for a measurement of the laser-pulse duration via self-referenced spectral interferometry [108, 109]. Using a single shot, it delivers both spectral phase and amplitude measurements and therefore enables the complete temporal characterisation of an ultrashort pulse. Furthermore, the Wizzler can send phase information of the laser pulse to the Dazzler to perform an optimisation of the laser beam. In the Wizzler, a replica of the input pulse is created and delayed. The main pulse generates a reference pulse via Cross-Polarized Wave Generation (XPW) [110]. XPW is a third-order nonlinear effect that generates a wave with a linear polarisation orthogonal to the input wave. The amplitude of the XPW pulse is linked to the input amplitude via:

$$E_{XPW}(t) \propto |E_{IN}(t)|^2 \cdot E_{IN}(t) \tag{3.2}$$

The created XPW pulse is therefore shorter and has a broader spectrum and a flatter phase compared to the input pulse. Both replica pulse and XPW pulse are sent to a

spectrometer that records an interference signal. Via Fourier-transform spectral interferometry [111], the spectral phase and amplitude of the pulse are then extracted in an iterative process. The Wizzler software enables an optimisation of the pulse within a few seconds and a measurement of the pulse duration at 10 Hz with higher accuracy compared to the Grenouille, which was previously used for characterisation of the SPECTRE laser [112]. However, it is worth noting that the measurement of the pulse duration using the Wizzler requires an input pulse close to its Fourier-limit (< 50 fs) due to the sensitivity of the XPW process to chirp. An example of the measurement of 1000 consecutive pulses from the SPECTRE laser after optimisation using the Wizzler can be seen in Fig. 3.9.

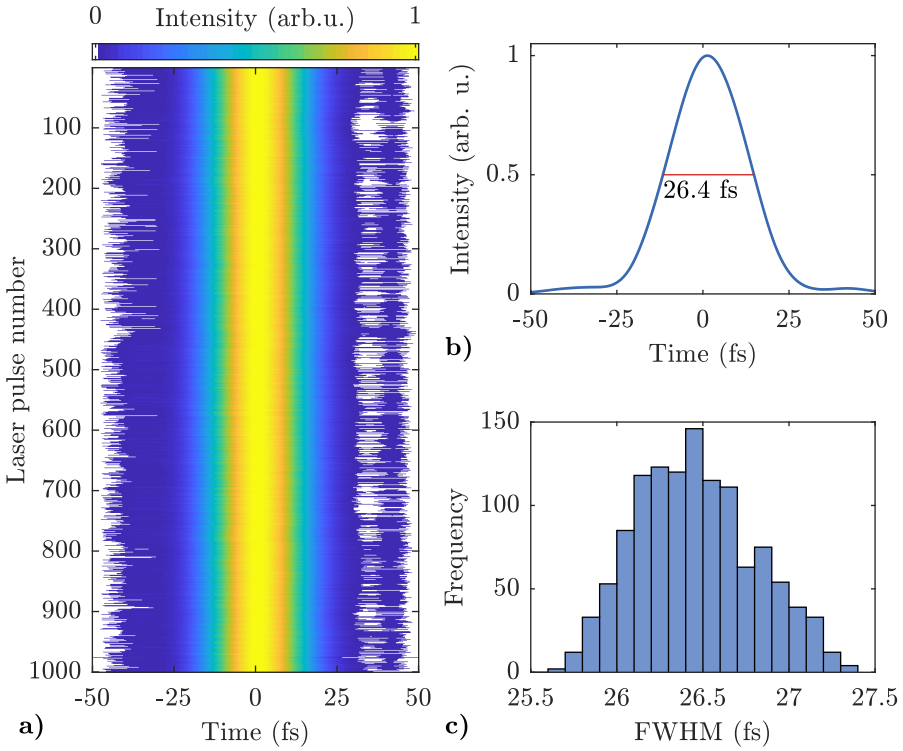

Figure 3.9: Measurement of the pulse duration of 1000 consecutive laser pulses. (a) waterfall plot of the shots. (b) average temporal profile with its FWHM. (c) histogram of the FWHM pulse duration of the 1000 shots displayed.

Especially at the plasma target, a detailed knowledge of the laser parameters is important (more information on the experimental setup will follow in the next section). The Wizzler could therefore be transported into the experimental laboratory to measure the pulse duration before the last focussing optic. Using a flip mirror in front of the focussing optics in the plasma chamber, it is possible to send the laser beam through a 1 mm thin vacuum window into the Wizzler. The Wizzler can therefore correct the laser pulse from any dispersion originating from optics after the compressor using the feedback control of the Dazzler to produce short pulses on target. In the measurement of the pulse duration, the effect of the group delay dispersion (GDD) on the laser pulse duration needs to be considered, which stretches the pulse. For the measurements described here, the laser

passes through a 1 mm-thick window made of fused silica and approximately 1 m of air, which results in a GDD of $36 \times 10^{-30}\,\mathrm{s}^2$ and $20 \times 10^{-30}\,\mathrm{s}^2$, respectively [113, 114] for an 800 nm laser. The resulting pulse duration t_{out} is dependent on the initial pulse duration t_{in} and the total GDD ϕ_2 and can be calculated via [113]:

$$t_{out} = \sqrt{t_{in}^4 + 16(ln2)^2\phi_2^2}/t_{in}. \tag{3.3}$$

As the output pulse duration for the 26.4 fs pulse depicted above does only change by about 2% from the total GDD of $56 \times 10^{-30}\,\mathrm{s}^2$, the pulses were not corrected for this effect after the measurement.

For alignment purposes, several near- and far-field cameras are installed in the laser beamline between the vacuum compressor and the LPA experiment to precisely measure the position and the pointing of the laser beam and allowing a reproducible alignment of it. To image the near- and far-field, two-inch lenses and 12 bit charge-coupled device (CCD) cameras are used in most cases. The near-field cameras could also be used to measure the energy stability of the laser during the experiments. In this case, the cameras were calibrated using commercial energy meters for. An example of the energy stability of 1000 laser shots measured using a near-field camera in the last amplifier stage (MP2) is depicted in Fig. 3.10. The standard deviation of the energy measurement of energy meter and camera measurement agree quite well with values of 1.1% and 1.2% respectively.

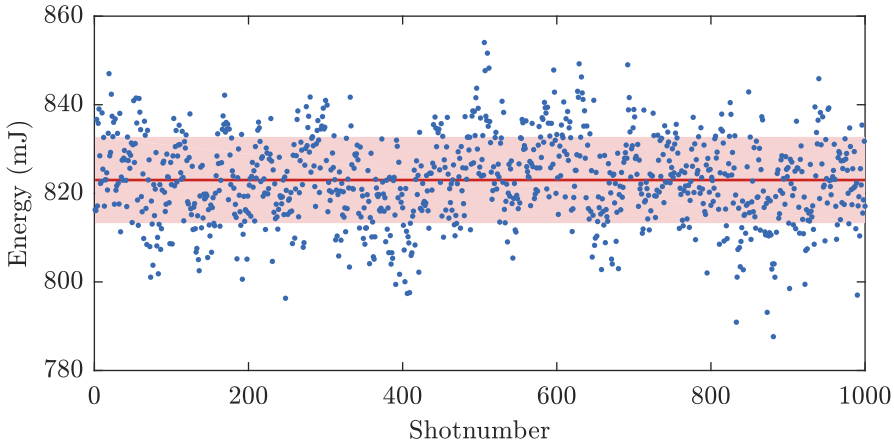

Figure 3.10: Measurement of the laser energy of 1000 laser pulses. The energy (before compression) of individual shots is shown as blue dots, the mean energy is shown as the red line, the red shaded area corresponds of the standard deviation of about 1.2%.

To image and improve the focus quality, a 14 bit charge-coupled device (CCD) camera is installed inside the vacuum in combination with an infinity-corrected objective with a magnification of 10. The average focal-spot image and the pointing stability of 200 consecutive shots is depicted in Fig. 3.11. The optimised focal spot shown here has a FWHM size of about $(10.1 \pm 0.2)\,\mu\mathrm{m}$ in the horizontal axis and $(13.0 \pm 0.5)\,\mu\mathrm{m}$ in the

vertical axis at a pointing stability of 2.0 µrad and 2.2 µrad, respectively.

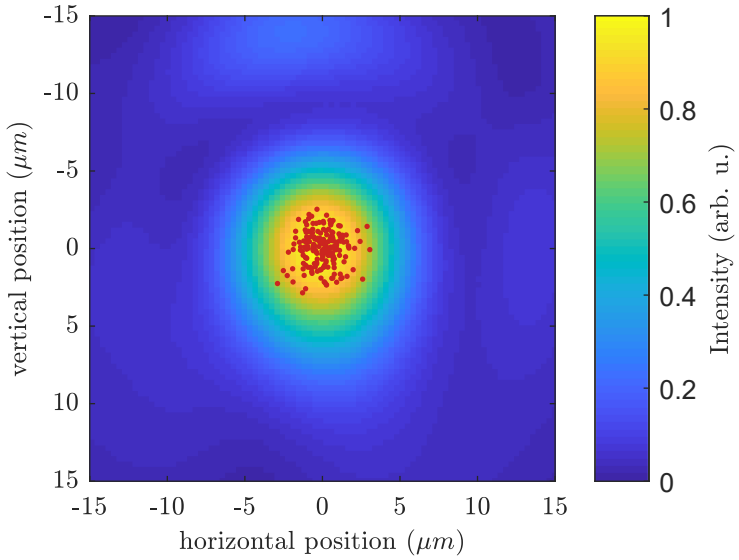

Figure 3.11: The average focal spot (corrected for pointing) of 200 consecutive shots with the centre-of-mass of individual shots shown as red dots. The pointing stability of the 200 shots is 2.0 µrad in the horizontal axis and 2.2 µrad in the vertical axis.

Another important factor for the laser spot is the M^2 value, as it reflects how well the laser beam can be focussed in comparison to an ideal Gaussian beam. The calculation of M^2 is regulated by ISO Standard 11146 and is based on the the measurement of the second-moment beam-width in horizontal($d_x(z)$) and vertical ($d_y(z)$) directions at different longitudinal positions (z) around the focus. For a detailed description of the calculation please refer to literature such as [115]. M^2 is defined as:

$$M^2 = \frac{d_0 \cdot \theta}{4} \frac{\pi}{\lambda}, \tag{3.4}$$

where d_0 is the second moment beam width in focus, θ is the beam divergence and λ the laser wavelength. d_0 and θ can be obtained from a second order fit of the squares of the beam width of the form:

$$d_{x,y}^2 = A + Bz + Cz^2. \tag{3.5}$$

This is depicted in Fig. 3.12, where the squares of the second order beam width in the horizontal axis and the corresponding second order polynomial fit are shown. Using the fit, the beam width in focus can be calculated via $d_0 = \sqrt{A - \frac{B^2}{4C}}$ and the beam divergence via $\theta = sqrtC$. This resulted in M^2 values for the focal scan in the depicted example of $M_x^2 = 1.8$ in the horizontal direction and $M_y^2 = 1.9$ in the vertical direction.

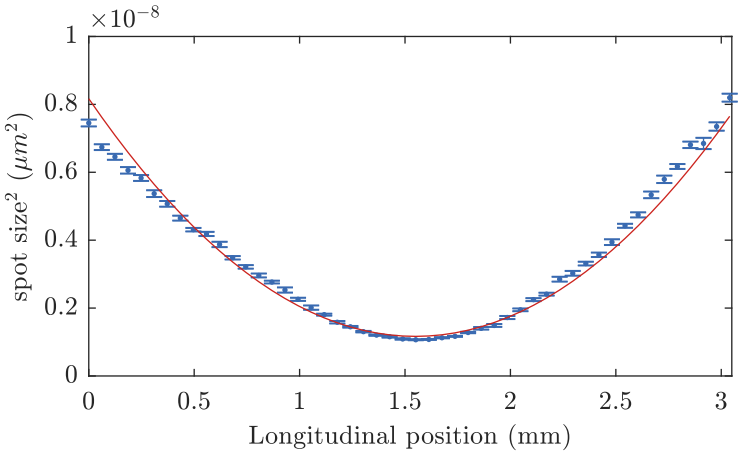

Figure 3.12: Squares of the second moment beam width in the horizontal axis and second order polynomial fit for M^2 calculation.

3.2 The BOND lab

The **B**eam **O**ptimisation and **N**ovel **D**iagnostics lab (BOND lab) is located next to the laser laboratory. A vacuum beamline enables the use of the SPECTRE laser for plasma acceleration and plasma target characterisation experiments in the BOND lab. A floorplan image of the lab showing the plasma acceleration chamber, diagnostic sections for the LPA experiments and the target characterisation setup is depicted in Fig. 3.13. In this section, only the general outline of the LPA setup and diagnostics will be described. For information on the plasma-target characterisation setup and results please refer to recent publications [86].

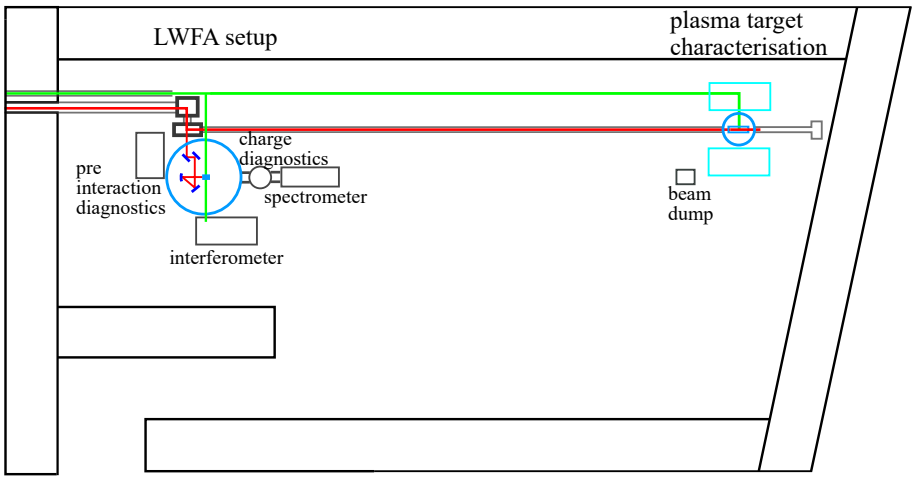

Figure 3.13: Floorplan of the BOND lab with LPA setup and plasma target characterisation setup.

3.2.1 The laser-plasma-acceleration chamber

The heart of the plasma experiments is the plasma-acceleration chamber, which is a vacuum chamber with a diameter of 1.4 m. The chamber houses the setup for the laser wakefield experiments, consisting of a focussing parabola, the plasma target and several diagnostics, motors and stages for alignment. In the chamber, the beam is focussed using an 3" off-axis parabola with a focal length of either 671 mm (silver coating) or 500 mm (dielectric coating) onto a gas-target, consisting of a sapphire capillary [116, 117] or a gas-jet nozzle [118]. To adjust the targets to the laser focus and beamline, the capillary is mounted on a Hexapod, allowing for alignment in all three translational dimensions and the corresponding angles of the capillary, while the gas jet is mounted on stages to allow movement in the longitudinal and transverse axes of the laser beam. For the gas jet, a differential pumping cube was developed, which is described in more detail in Sec. 4.3. The differential pumping allows low residual pressures in the vacuum interaction chamber and the vacuum compressor to be maintained, even when firing the gas jet at high repetition rates. A transverse laser probe enables the measurement of the plasma density of the gas jet, as described in more detail below.

In addition, the laser infrastructure for Thomson experiments and the alignment of this laser beamline is done in the plasma acceleration chamber. This includes corresponding motors and stages and diagnostics for alignment of the Thomson laser arm. Furthermore, an active plasma lens (APL) [119, 120] can be used in the plasma chamber for emittance measurements [121], or tunable and narrow bandwidth Thomson-scattering experiments [7, 122].

3.2.2 Electron diagnostics

A detailed characterisation of the electrons is required to make any meaningful statements about the produced beams. Informations about several aspects of the electrons can further help to find correlations to other parameters of the experiments and help to improve the quality and stability of the electron source. A number of diagnostics is available to measure the electron beam pointing, divergence, charge and energy in the BOND lab. The electron-beam pointing and divergence is measured on a profile screen, consisting of a phosphor screen imaged with a CCD camera. The charge can be either measured non-invasively using a cavity (the so-called DaMon [123, 124]) and an integrating current transformer (ICT, sometimes also called toroid [125]) or using the profile screen in an invasive measurement [112, 126]. The electron energy is measured in the electron spectrometer, consisting of a dipole magnet and phosphor screens imaged by CCD cameras. To be able to describe the produced electron beams in later parts of this thesis, the working principle of these diagnostics is described here in more detail. The use of Thomson scattering as a diagnostic described in Chapter 5. A comparison of the different charge-diagnostic techniques can be found in Appendix B.

Phosphor screens

Phosphor screens convert energy of particles passing through the screen into visible light. For the case of electrons, the energy stored in a screen is roughly constant for kinetic energies larger than 1 MeV [127]. Consequently, these screens can be used for a wide variety of diagnostics applications. In the BOND lab, phosphor screens are used to measure pointing and divergence of the electron beam, the beam charge and, in combination with a dipole magnet, the spectrum of produced electron bunches. The emission of light happens via luminescent processes, which are similar to the physics in a laser gain medium described in Sec. 3.1.1. In phosphor screens, these processes are called fluorescence and phosphorescence [112, 126]. Both processes describe a decay from an excited state to the ground state under emission of a photon. The schematic Jablonski diagram [128] for fluorescence and phosphorescence is depicted in Fig. 3.14.

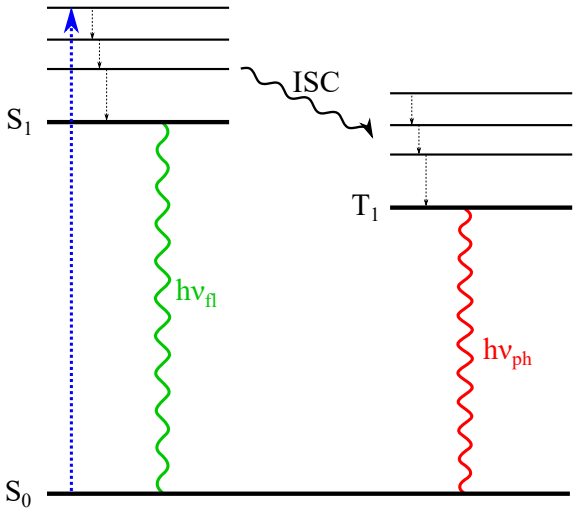

Figure 3.14: Jablonski diagram of fluorescence and phosphorescence [128]. An electron is excited from the ground state S_0 to an excited singlet state S_1. Under emission of a fluorescence photon, the excited electron can transition back to the ground state. Alternatively, the excitation of the electron is followed by an intersystem crossing (ISC) from the singlet state S_1 to a triplet state T_1. As the transition from the triplet state T_1 to the ground state S_0 is spin-forbidden, the decay is much slower. Such a decay is called phosphorescence.

For both processes, an electron is excited from the ground state (valence band) S_0 to an excited state S_1 (conduction band). Within the excited state, the electron can undergo non-radiative transitions to the lowest vibration level via vibrational relaxation. In fluorescence, which was first described by Stokes in 1852 [129], the electron can fall down to the ground state under emission of a photon with an energy of S_1 - S_0. As the excited state is usually unstable, this process happens on timescales of microseconds. In the case of phosphorescence, the electron changes from the excited singlet state S_1 to an excited triplet state T_1 via intersystem crossing. From the triplet state, the electron can then transition to the ground state, similarly to fluorescence, However, according to the

quantum-mechanical selection rules (please refer to text books such as [130]), a transition from T_1 to S_0 is spin-forbidden. Therefore, phosphorescence happens on slower timescales of milliseconds up to several seconds or even minutes, depending on the materials used.

The phosphor screen used in these experiments is called DRZ-High and consists of a phosphor layer, a thin protective layer made of PET and a plastic supporting layer. The phosphor layer in DRZ-High is made of Gd_2O_2S, know as Gadox, which is doped with terbium. This material offers high light yield due to the high atomic numbers and densities of gadolinium and terbium. In addition, the main fluorescence line of Gadox is at a wavelength of 545 nm, which is advantageous for imaging with modern CCD camera chips due to the high quantum efficiency of the chips for green light [131]. The DRZ screens were absolutely calibrated together with several different screen types and a tritium source at the ELBE accelerator in the Helmholtz Center Dresden Rossendorf (HZDR) [132, 133]. Compared to other phosphor screens based on the same phosphoric material (e.g. LANEX screens or BioMAX screens), DRZ-High offers higher light yield per electron charge and is more linear at high charge densities, making it a good choice for many diagnostic applications.

The tritium source used to calibrate the imaging systems in the absolute calibration campaign was cross calibrated to tritium sources at DESY in the context of this work, allowing the application of the absolute calibration to other setups in the FLASHForward framework. The results of this cross calibration can be found in the Appendix A.

The phosphor screens were also used to detect X-rays produced in the experiments. The detection of X-rays is an indirect detection of the secondary particles produced inside the DRZ screen via the photoelectric effect, Compton scattering and pair production. The detection of an X-ray beam with DRZ is then analogous to the use of phosphor screens for the detection an electron beam. The underlying processes for the production of secondary electrons are described in Sec. 5.3.1. Consequently, measurements done using phosphor screens are sensitive to noise from X-rays produced during or after the electron acceleration.

Profile Screen

The profile screen consists of a DRZ-high screen, which can be driven into the electron beam at a distance of 1.3 m from the gas target. The screen is installed at an angle of 45 degrees with respect to the electron axis to enable imaging of the reverse side of the screen from the top. The size of 70 mm by 50 mm leads to a sensitive area of roughly 40 mrad × 40 mrad in the two transverse axes. To prevent laser light from illuminating the screen, two layers of 50 µm-thick anodized aluminium foil were attached to the front surface of the screen. The screen was then imaged with an 8 mm f/1.4 lens onto a 12 bit CCD camera. A 10 nm bandpass filter around the central Gadox wavelength of 545 nm was installed in front of the camera to reduce residual laser light reaching the camera chip from scattering and plasma radiation by several orders of magnitude outside the

filter bandwidth. An additional ND1 filter was installed on a flip mount to increase the dynamic range of the profile screen measurement and prevent saturation in case of high-charge beams. The imaging was spatially calibrated using graph paper to enable the use of the screen as a diagnostic of the beam pointing and beam divergence. A cross-calibration using tritium sources enabled to apply the absolute calibration of the screen done at HZDR to be applied. Therefore, the screen can also be used as an invasive charge diagnostic.

DaMon

Two additional diagnostics were installed for a non-invasive measurement of the electron-bunch charge. One of these diagnostics is the DaMon [123, 124], which stands for **da**rk current **mon**itor whose name derives from its original use to detect dark currents in the FLASH accelerator. The DaMon consists of a stainless steel cavity with its first monopole mode at $f = 1.3\,\mathrm{GHz}$. A beam passing through the cavity will stimulate the first monopole mode with a voltage of

$$U = U_0 \sin(\omega t) e^{-t/\tau}, \tag{3.6}$$

with $\omega = 2\pi f$ and a decay time $\tau = Q_L/(\pi f)$, where Q_L is the resonator-loaded quality factor. The amplitude of this monopole mode U_0 is proportional to the beam charge q via

$$U_0 = qS. \tag{3.7}$$

S is the sensitivity defined as $S = \pi f \sqrt{\frac{Z}{Q_{ext}} \left(\frac{R}{Q}\right)}$, where Z is the line impedance, Q_{ext} is the resonator external quality factor and $\left(\frac{R}{Q}\right)$ is the normalized shunt impedance. As the sensitivity is only defined by constants, the amplitude of the first monopole mode (also known as TM01 mode) is directly proportional to the bunch charge. In case of knowing the values previously stated (as is the case for the unit installed in the BOND lab), the electron-bunch charge can therefore be determined from a measurement of the amplitude of the TM01 mode. It should be noted that the TM01 mode is not dependant on the position of the electron bunch inside the cavity.

For a measurement of the amplitude, two antennae were installed to provide a high dynamic range. The signal from the antennae is then processed by a dedicated electronics unit that filters and converts the amplitude to a logarithmic value which is then sent to an analog-to-digital converter (ADC). By the use of two antennae and conversion to a logarithmic scale, the DaMon can detect bunch charges with a dynamic range of seven orders of magnitude. The minimum charge detectable is roughly 50 fC, limited by the noise in the electronics. By upgrading of the electronics (e.g. cooling), the noise level could be lowered below one femtocoulomb [134]. Shielded cables reduce noise of electromagnetic pulses (EMP) being picked up, as is depicted in an image of the DaMon in Fig. 3.15.

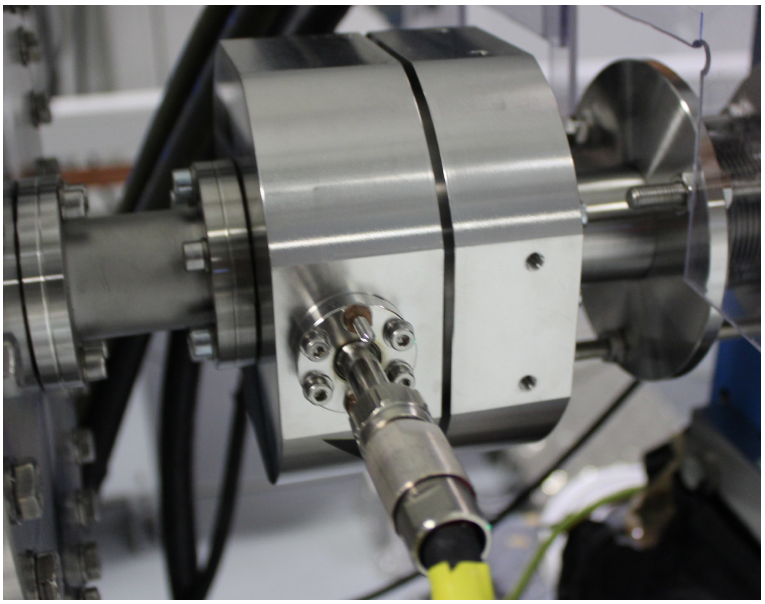

Figure 3.15: Image of the DaMon. The cavity is connected to the electron beam pipe enabling the measurement of the charge of an electron bunch travelling through it. The antenna for measurement of the Amplitude of the TM01 mode is visible in the front. A second antenna is at the back for higher dynamic range which can not be seen in the image.

Integrating current transformer

The second non-invasive charge diagnostic implemented in the setup is an integrating current transformer (ICT) [112, 125], sometimes also known as a toroid. The ICT is a passive transformer for the measurement of charges of short electron bunches. It is made of a single-turn, capacitively shorted transformer and a second, fast-read-out transformer in a common magnetic circuit. A passing electron bunch loads its charge instantaneously into the single-turn transformer. Afterwards, the charge is slowly transferred to the second transformer, leading to a pulse with a rise time of approximately 20 ns irrespective of the electron bunch duration while at the same time avoiding core losses.

The ICT is commonly used in plasma-acceleration experiments for charge measurements [18, 20] despite its known disturbance in the presence of EMP noise from e.g. powerful lasers, plasma EMP, or discharge units [26, 125, 127, 135]. The influence of EMP on the measurement of the electron charge using the ICT was also found in experiments in the BOND lab (compare Sec. B in the Appendix). Therefore all measurements of the electron-bunch charge stated in the following experimental sections were performed with the DaMon.

Electron spectrometer

The energy of the electrons is measured in the electron spectrometer. The spectrometer in the BOND lab is a single-shot dipole spectrometer commonly used in wakefield experiments

[127, 136, 137]. The dipole magnet bends the electron trajectories according to their energy due to the Lorentz force acting on the electrons. A measurement of the bending radii using phosphor screens therefore enables the electron spectrum to be determined in a single shot.

The dipole magnet used in the BOND lab is an electromagnet with length of 500 mm and a maximum current of 311 A, resulting in a magnetic field strength of 245 mT. The magnet surrounds a vacuum chamber that prevents scattering of the electrons with air. Using the maximum current, electron energies of up to 500 MeV can be resolved. Full 3D measurements of the magnetic field inside the dipole were performed for currents of 311 A, 250 A and 180 A. These field maps are used for a calculation of the electron trajectories, Furthermore, a relative calibration of the maximum field as a function of the current was done using a Hall probe at a single measurement position, allowing to scale the 3D maps for arbitrary current settings. The result of the calibration is shown in Fig. 3.16, indicating a linear behaviour up to currents of about 250 A. Despite the tuning ability of the electromagnet, the spectrometer was mostly operated at a current of 180 A, which enabled an easy comparison of the electron beams of different measurement campaigns.

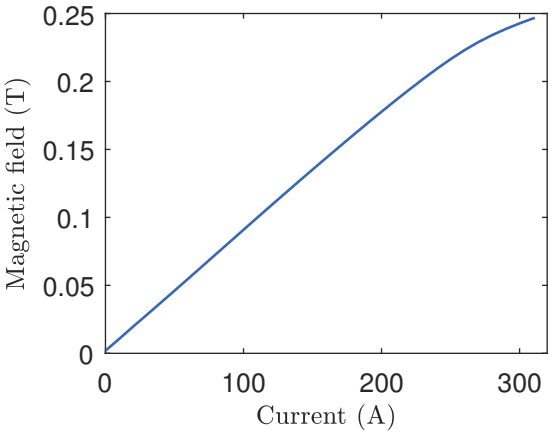

Figure 3.16: Calibration of the magnetic field of the electron spectrometer dipole magnet as a function of the current.

For the measurement of the electron bending radii, two DRZ-high type phosphor screens are used. The first screen is mounted in the forward direction at an angle of 125 degrees with respect to the electron beam axis to detect high-energy electrons ($>$ 35 MeV at 180 A). The distance of the forward screen from the gas target is roughly 2.25 m. Under the magnet, a second screen was attached to the bottom of the magnet parallel to the electron beam axis to detect low-energy electrons. Both screens were attached to a 1 mm-thick steel plate, functioning as the vacuum window of the magnet chamber. A support for the vacuum chamber leads to a gap between the two phosphor screens preventing the detection of electrons in that region. While the high light output of DRZ-high screens is beneficial for the low charge density of the dispersed electron beams, the low resolution of the screen compared to other screens leads to a broadening of the signal and potential overestimation of the spectral bandwidth. Despite the use of screens with high light yield,

the signal on the low-energy screen was usually not sufficient for an efficient detection of the lower electron energies (especially in the case of quasi-monoenergetic beams), which is why only the spectrum obtained from the high-energy screen will be shown here.

Several effects can lead to a broadening of the measured spectra and a full analysis and deconvolution of these effects can easily fill an entire thesis [137]. The main effects that have to be considered are the resolution of the imaging system, broadening of the signal in the phosphor screen and the vacuum window, broadening from the electron beam divergence and, in the case of multiple shots, pointing fluctuations of the beam. Understanding of the broadening effects is essential when comparing spectrum measurements of the electron beams to those obtained from PIC simulations.

The resolution of the imaging system was measured by determining the edge sharpness of a chessboard pattern, which resulted in a resolution of the transition of roughly 520 µm. The resolution of the phosphor screen can be obtained from the modulation transfer function (MTF) of the screen [138, 139]. From the MTF, the point spread function (PSF), which can be used as a measure of the resolution of the screen, can be calculated via Fourier transformation. The resulting PSF for DRZ-high and a power law fit are depicted in Fig. 3.17. The fit resulted in a half width at half maximum of 130 µm, such that the screen resolution is considered to be 260 µm. For a more detailed description of the resolution of imaging screen please refer to literature [138]. The broadening of the electron beam in the steel vacuum window can be estimated by the RMS scattering angle $\sqrt{\langle\theta^2\rangle}$ arising from multiple-scattering in the material. The scattering angle is defined by [140]:

$$\sqrt{\langle\theta^2\rangle} = 13.6\frac{1}{\beta p}\sqrt{\frac{x}{X_0}}\left(1 + 0.038\,\ln\frac{x}{X_0}\right), \tag{3.8}$$

where β is the velocity relative to the speed of light, p the total momentum in MeV/c, X_0 the radiation length of the material and x the thickness of the material. For 1 mm of iron, this results in a scattering angle of 3.3 degree for an electron with an energy of 50 MeV. An upper estimate of this broadening effect can be made multiplying the thickness of the material by the tangent of the scattering angle, which results in a broadening of the beam by 58 µm. Compared to the other effects described here even this upper limit is relatively small, such that the effect can be neglected for the broadening in the even thinner DRZ screen. In total, the broadening arising from the optical imaging resolution, the screen resolution and broadening in the vacuum window and DRZ screen is estimated with 1 mm.

More broadening originates from the electron beam divergence and pointing. The divergence and pointing stability of the beams of several milliradian each leads to a more significant broadening on the order of several millimetres, due to the distance of the screen from the gas target of approximately 2.25 m. A more detailed description of the beams and their divergence and pointing stability will be presented in the following chapter. As these broadening effects are highly dependent on the electron beam parameters, their calculation

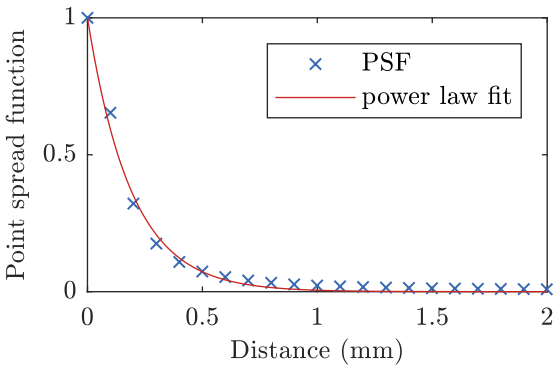

Figure 3.17: Point spread function obtained from Fourier transformation of the modulation transfer function of DRZ-high.

is also presented after a discussion of the electron beam parameters. The calculation of the broadening from the divergence is done via tracking of the electrons through the measured magnetic field. From the tracking, the energy dependent broadening of the signal on the DRZ screen can be determined. An example is shown in Fig. 3.18, where the energy dependent broadening on the DRZ screen is depicted for electrons with a FWHM divergence of 8 mrad. Using the tracking it is also possible to study the influence of the pointing fluctuations by tracking the electrons with a pre-defined pointing offset. The offset of the energies at the screen from the resulting tracking matrices can then be used to calculate the broadening of this effect. This will again be explained in more detail in the following chapter where the measured electron spectra are compared to the result of PIC simulations.

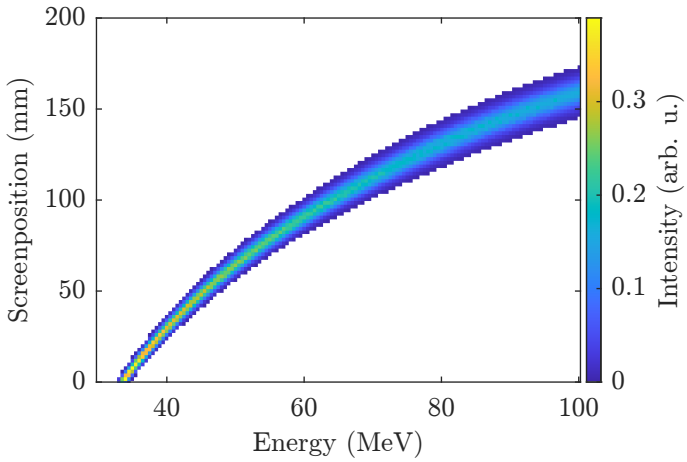

Figure 3.18: Broadening of the electron beam on the DRZ screen as a function of the electron energy for an electron beam with an FWHM divergence of 8 mrad.

Several other second order effects would have to be considered for a complete analysis of the broadening, such as the collection efficiency of the camera as a function of the screen position. However, a complete analysis of this and further effects would go beyond the scope of this work. Nevertheless, a comparison of electron beams from PIC simulations

and the measured electron spectra is possible using the broadening effects described in this section.

3.2.3 The probe beam and density measurements

Another important parameter for electron acceleration is the plasma density. For the LPA experiments in the BOND lab, the measurement of the plasma density is done using interferometry [141–143]. The refractive index of a plasma is dependent on the electron density in the plasma. A transverse laser beam passing through the plasma will therefore experience a phase shift compared to a laser beam that travels through vacuum. The line-integrated plasma density is then proportional to the phase shift measured by an interferometer [144].

In the BOND lab, the probe beam originating from the air compressor of the laser system is used for the interferometry measurements. This enables independent timing of the probe beam which is also advantageous for the Thomson experiments (see Chapter 5). After passing through the plasma, the probe beam is transported outside the plasma chamber and sent to a Mach-Zehnder interferometer, where a part of the probe beam that passed through the plasma is overlapped with a part of the beam that travelled through vacuum only. The beams are imaged onto a CCD camera using a lens. As the region of visibility of fringes is inversely proportional to the bandwidth of the laser pulse [144] used for interferometry, a bandpass filter around the central laser wavelength is installed in front of the camera to enhance the contrast of the resulting fringes. A sketch of the setup is depicted in Fig. 3.19

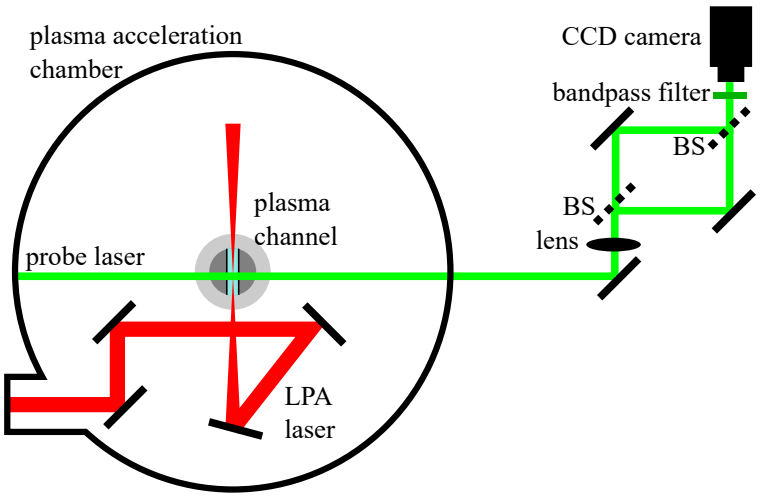

Figure 3.19: Sketch of the density measurement setup. The LPA laser (red) is focussed onto the gas jet to create a plasma. The transverse probe beam (green) is passes the plasma channel and is transported outside the chamber. The beam is sent through a Mach-Zehnder interferometer where a a region of the beam that passed the plasma is overlapped with a region that did not pass the plasma. The plane of the plasma is then imaged on a CCD camera using a lens.

From the fringe shift, the phase shift of the beam can be acquired using Fourier transformation. As the resulting phase can only take values between $-\pi$ and π, the resulting phase map needs to be unwrapped to retrieve a phase map without unphysical jumps of the phase by 2π. From the resulting two-dimensional map of the phase shift $\Delta\phi$(z,y), where z is the propagation direction of the LPA laser and y the axis perpendicular to LPA laser and probe laser, it is then possible to calculate the plasma density via an Abel inversion. This requires the assumption of a radially symmetric density profile such that the 2D phase shift $\Delta\phi$(z,y) is transformed to a radially symmetric density $n_e(z,r)$ via:

$$n_e(z,r) = \frac{\lambda_0 n_c}{\pi^2} \int_r^\infty \frac{d\Delta\phi(z,y)}{dy} \frac{1}{\sqrt{y^2 - r^2}} dy. \tag{3.9}$$

Here, λ_0 is the wavelength of the probe laser and n_c is the critical plasma density. While perfect cylindrical symmetry is not achievable due to a decreasing density away from the gas jet and imperfections of the laser pulse, the approximation is required for density retrieval using this technique and is usually sufficiently accurate for a density measurement. For a more detailed description of the phase retrieval and the subsequent calculation of the density, please refer to [144].

Chapter 4

Development of a stable electron source

A major part of this thesis was the development and improvement of the electron source, starting from the first electrons in the BOND lab towards a reproducible, high-repetition-rate electron beam. The chapter starts with a short description of the first electron beams accelerated in the BOND lab in Sec. 4.1 and the efforts necessary for these beams. Afterwards, results of a comparison of three different injection mechanisms that were tested in the laboratory are presented in Sec. 4.2. In Sec. 4.3, the improvement of these beams towards a reproducible, high-repetition-rate electron source, which was used for the data taking of several theses [7, 121, 145, 146] and publications [3, 147], is described. Finally, the results of an 8 hour stability test with thousands of consecutive shots is presented in Sec. 4.4, which is also prepared for a separate publication [3]. The next steps for further optimisation of the electron beams are presented in Sec. 4.5.

4.1 Early self-injection experiments

To accelerate electrons in a laser plasma acceleration setup, a detailed understanding and control of the laser is necessary. Therefore, most of the components and diagnostics described in the previous section were already installed for the first electron acceleration in the BOND lab. A schematic of the first acceleration setup is depicted in Fig. 4.1. A photograph of the chamber for the first experiments can be seen in Fig. 4.2.

The diagnostics required for the acceleration of the first electron beams were built up and optimised in multiple iterations, which was part of this work. To get a better understanding of the processes, diagnostics such as laser spectrometers and further alignment cameras were set up before the first successful accelerations. The cameras and spectrometers helped to achieve a more precise alignment and to optimise plasma density and laser energy in a more controlled way. The maximisation of the red shift of the laser in the plasma for example, which indicates the driving of the wakefield, was possible after the implementation of the spectrometers. Using the added diagnostics, the first successful acceleration of electron beams in the BOND lab was enabled. An image of the first ever electron beam accelerated in the BOND lab is depicted in Fig. 4.3.

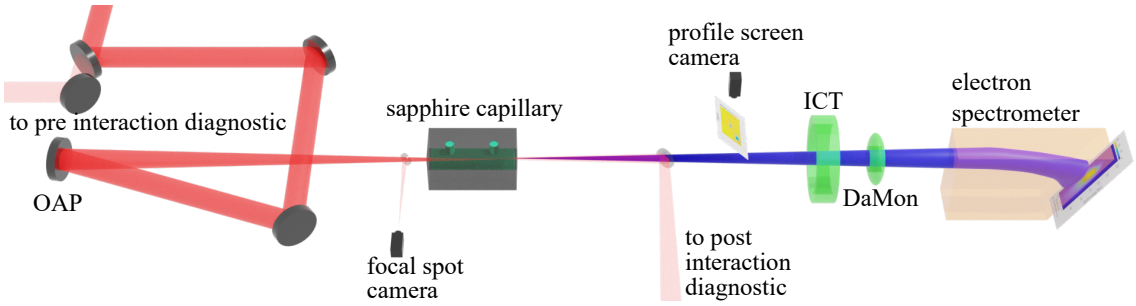

Figure 4.1: Schematic drawing of the setup for first self-injection experiments. The beam enters the main vacuum chamber and the leakage of the first mirror is sent to the pre-interaction diagnostics for alignment. The reflected part is sent to an f/14 off-axis parabola (OAP), which focussed the beam onto a sapphire capillary with a length of 15 mm and a diameter of 200 µm. To check the focus quality, a wedge could be driven into the focussed laser beam in front of the capillary, sending it into a focal-spot camera. The focal-spot quality was then optimised in vacuum using pico motors. Before the parabola, a pickoff mirror could be flipped into the beam to sent the pulse to the pre-interaction diagnostics for pulse-duration measurements. The additional dispersion of the window was compensated using the Dazzler. After the capillary, the laser could be collected using a second wedge, was refocussed and sent to the post-interaction diagnostics for laser alignment, capillary alignment and spectral analysis of the laser beam. To characterise the electron beams, a profile screen and an electron spectrometer are available. Within the first few weeks after electron acceleration, the ICT and the DaMon, were added, which offered a non-invasive measurement of the bunch charge.

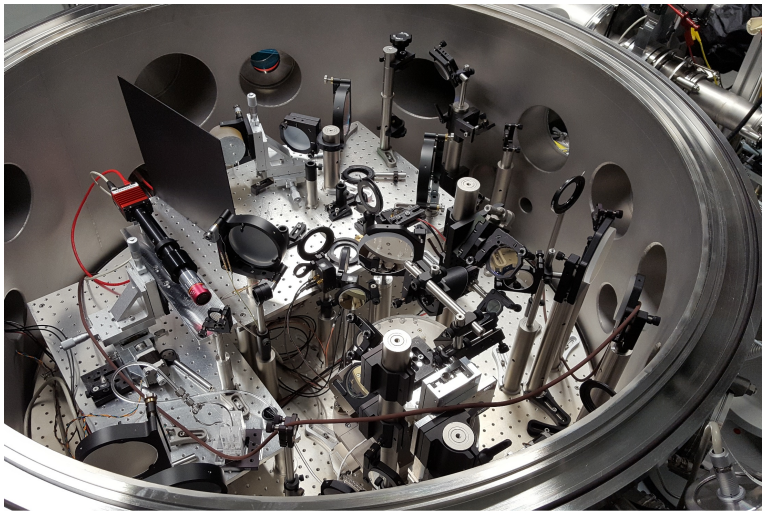

Figure 4.2: Photograph of the LPA chamber for the first electron acceleration.

Once the key parameters for electron acceleration were found, the beams could be optimised and also other injection techniques such as ionisation injection were successfully tested. Subsequently, improvement of the laser and plasma parameters lead to singular electron beams with small divergence and narrow spectra, as is shown in Fig. 4.4.

The profile image in Fig. 4.4a shows a beam with an divergence of only 3.9 mrad in the vertical and 4.3 mrad in the horizontal axis, and all three spectra shown in Fig.

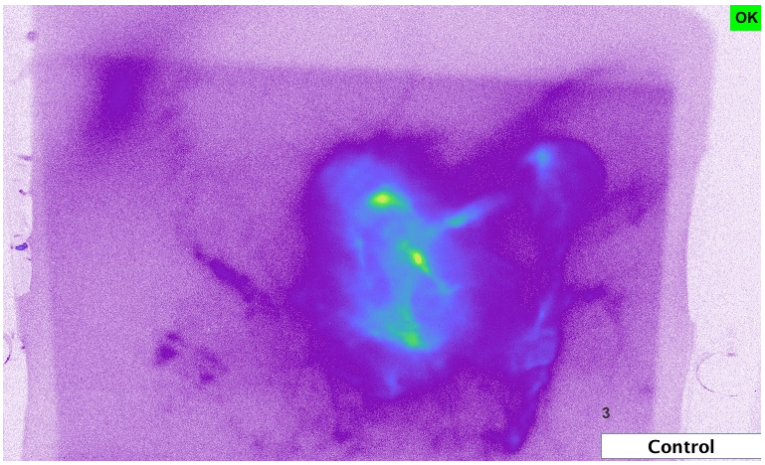

Figure 4.3: Logbook image of the first electron beam accelerated in the BOND lab.

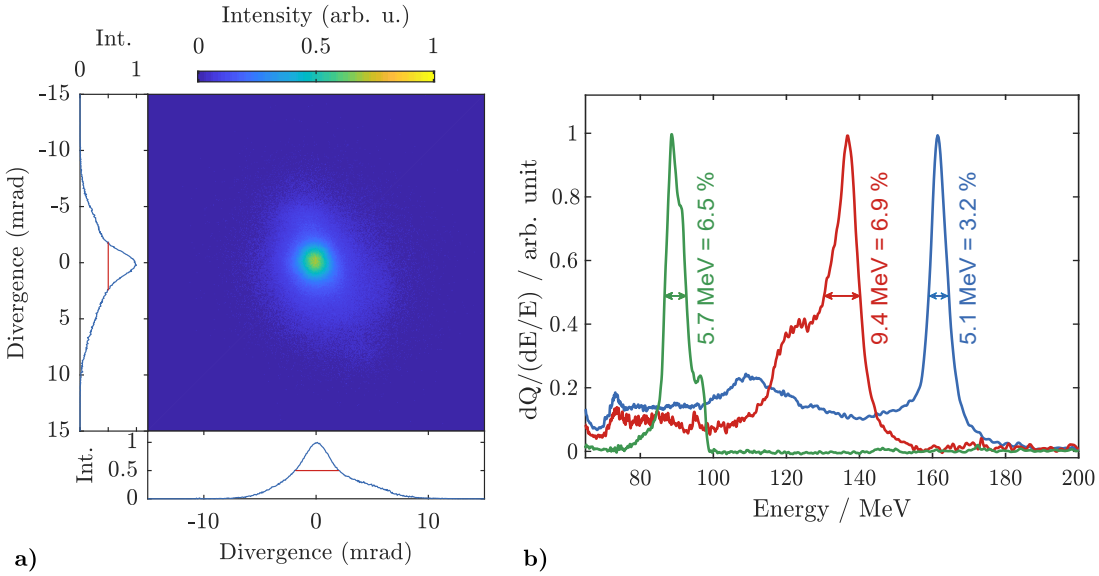

Figure 4.4: (a) profile image and (b) three spectra of early electron beams.

4.4b have a bandwidth of less than 10% FWHM. First studies of betatron radiation for emittance measurements [112] and tests of the charge diagnostics [148] were therefore possible using these beams. However, the reproducibility and stability of the electron beams needed improvement, as can be seen in Fig 4.5, where the pointing stability and the resulting integrated beam profile of an ionisation-injection test with 190 shots taken over about 4 hours in February 2017 is shown. The pointing stability of this run resulted in a standard deviation of 3.9 mrad in the horizontal axis and 6.4 mrad in the vertical axis and a correspondingly big integrated profile image. As diagnostics required for a detailed study of the acceleration process such as e.g. density measurements were not available yet, the origin of the fluctuations could not be studied in more detail. Furthermore, measurements of the charge of the early beams were not possible in a reliable way as described in Appendix B.

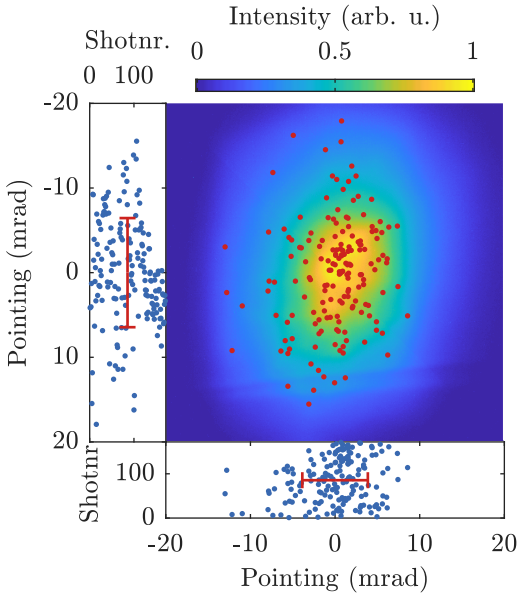

Figure 4.5: Pointing stability and integrated profile image of an early stability run with 190 shots.

4.2 Comparison of different injection schemes

After the first successful tests of the system, the focus was on creating a stable and reliable electron source. The development of a stable electron source was necessary for many LPA experiments at FLASHForward such as the study of plasma lenses [121], Thomson experiments for medical imaging [6, 7] or the measurement of electron parameters using Thomson scattering which is described in Chapter 5. Especially the Thomson experiments set certain requirements on the stability of the electron source, as these experiments had to be performed as multi-shot experiments due to difficulties in the detection of the produced X-rays. Pointing stability and spectral stability were of high importance for all of the planned experiments. In case of the Thomson experiments, the stability was required to integrate the X-ray signal from multiple shots on the detector. In the case of plasma-lens experiments, a reliable pointing was required to align the beam centrally through the lens without introducing a dipole kick to energies not imaged on the electron spectrometer screen. The Thomson experiments further required a stable electron-beam charge to be able to adjust the flux to the detector and prevent saturation. Lastly, a small divergence of the beams and a narrow spectrum would be beneficial for medical-imaging experiments to reduce the background. These experiments were also the only ones which set requirements on the electron energy. In a design study using Thomson simulations it was found that the optimal energy for X-ray fluorescence imaging using gold nanoparticles is 64 MeV [149, 150], which was targeted for in the experiments.

The planned experiments also required a change of the layout inside the acceleration chamber. The sapphire capillary was exchanged for a gas-jet target in order to allow an overlap of the Thomson laser and electron beam inside the plasma and the use of the

capillary as a plasma lens. The 671 mm parabola was changed to a parabola with a focal length of 500 mm. The use of a parabola with a shorter focal length is advantageous for the Thomson experiments, as it allows similar peak intensities to be reached in the focus even after splitting the laser beam in an LPA and a Thomson part and eases the layout in the chamber. Due to the amount of changes necessary, a full rebuild of the acceleration chamber was required. As the planned Thomson experiments complicated the new layout of the chamber and less space was available, the post interaction laser diagnostics were removed. An interferometer setup using the transverse probe beam was added to measure the plasma density of the gas jet as described in Sec. 3.2 but was only commissioned at a later stage. A schematic of the changed setup is depicted in Fig. 4.6.

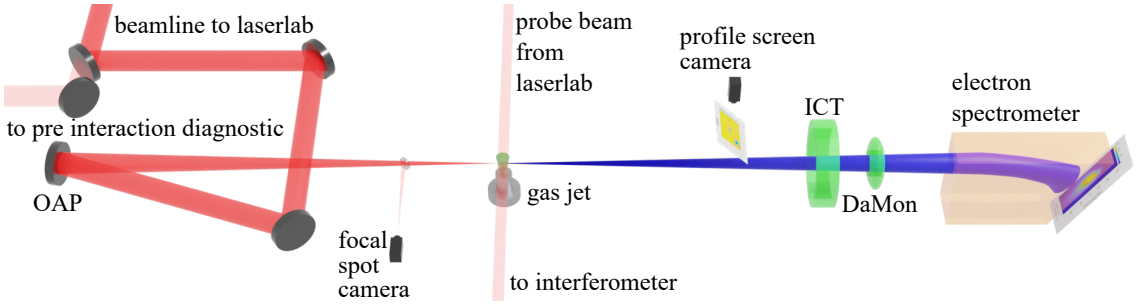

Figure 4.6: Schematic drawing of the setup for injection-mechanism comparison. The beam enters the main vacuum chamber and the leakage of the first mirror is sent to the pre-interaction diagnostic table for alignment and pulse-duration measurements. The reflected part of the beam is sent to a 3" f/11 off-axis parabola (OAP). The parabola focusses the beam onto a gas jet with a diameter of either 1 mm or 3 mm. To check the focus quality, a wedge could be driven into the focussed laser beam in front of the gas jet, sending the beam into a focal-spot camera. The focal spot-quality was then optimised in vacuum using pico motors on mirror mounts and the mount of the OAP. A transverse probe laser was used in combination with a Mach–Zehnder interferometer to monitor the plasma density of the gas jet. To characterise the electron beams, a profile screen for divergence and pointing and charge measurements, an ICT and a DaMon for non-invasive charge measurements and an electron spectrometer for energy measurements are available.

In order to produce stable electron beams with the parameters mentioned above, several injection techniques were tested. The methods used were further studies of self-injection beams with the gas-jet target, as well as the two more controlled injection schemes, shock-front injection and ionisation injection. For all of these techniques, several parameters were available for the optimisation of the electron beams. Examples are laser energy, pointing and focus positions as well as the spectral phase of the laser, the gas species, plasma density or the position of the gas jet. In the case of shock-front injection, the position of the blade used to create the density shock added more parameters to tune, while for ionisation injection, different gas-doping species and doping percentages were tested. As this number of degrees of freedom are too many for detailed scans of all parameters for the three different injection techniques studied here, it is unlikely that the

optimal parameters for the used setup were found for the three different injection mechanisms. Nevertheless, the beam stability of the optimal parameters found for the different injection techniques is compared in this section. As these scans were performed at relatively low repetition rates, no dedicated stability runs for the optimal parameter with hundreds of shots were performed. Especially in the case of obviously unstable beams, no time was wasted to demonstrate the instability with high statistical precision. Therefore, sometimes the comparison of the stability of the different injection methods was sometimes based on only a few shots.

The main focus was on finding beams stable in, pointing, energy and charge. The maximum energy achievable in the LPA process was only of secondary importance, as the optimisation towards 64 MeV was planned to be part of further optimisation using the ideal injection technique. In addition to the stability at the best parameter set found, the scans performed already gave hints on the robustness of the methods as they would be stable for a wider range of parameters, or only work with very specific settings. This robustness of the injection technique was also included in the final decision on finding the optimal injection method for the future experimental goals.

For all of these injection techniques, a detailed understanding of the experimental parameters would be desired to be able to find the origin of possible instabilities. However, as the comparison shown here was done at an early stage of the setup, several diagnostics were not available or not commissioned yet. Examples are the Wizzler required for pulse-duration measurements which was added at a later stage, and the interferometer for plasma density measurements, which had not been commissioned at the time.

To still be able to compare the different methods, the stability of the system is estimated here. From near-field images of the last amplifier stage, the energy stability of the laser was calculated, similar as in the example in Sec. 3.1.3. While several other effects such as pulse duration play an important role in the acceleration process, this value still enables a comparison of the overall stability of the laser for the different injection techniques. As the interferometer setup was not commissioned yet, the stability of the plasma density could only be determined relatively. While interferometer images were saved, the lack of references prevented the calculation of the actual plasma densities from the measured phase shifts. Furthermore, the low image resolution in this early setup prevented the analysis of the images from self injection and shock-front injection tests. In the ionisation injection experiments described in this section, the standard deviation of the plasma density was found to be 8%. This instability most likely originated from differences in the backing pressure as will be explained in Sec. 4.3. As the same gas system was used for all experiments discussed in this section, the fluctuations of the plasma density will be assumed to be similar for all presented datasets. It should also be noted that the data shown in this section was taken within a period of one month, such that a similar overall stability of the system for all presented experiments can be assumed.

4.2.1 Self injection

The first method tested with the new setup was self injection (SI). To reach the intensities required for self injection, high backing pressures and plasma densities were needed. Fluctuations of the backing pressure therefore also led to more unstable beams, especially with regard to the pointing compared to the SI beams achieved using the sapphire capillaries. However, the SI beams were further optimised by changing the parameters described above. Results of the optimisation runs are shown in Fig. 4.7 and Fig. 4.8.

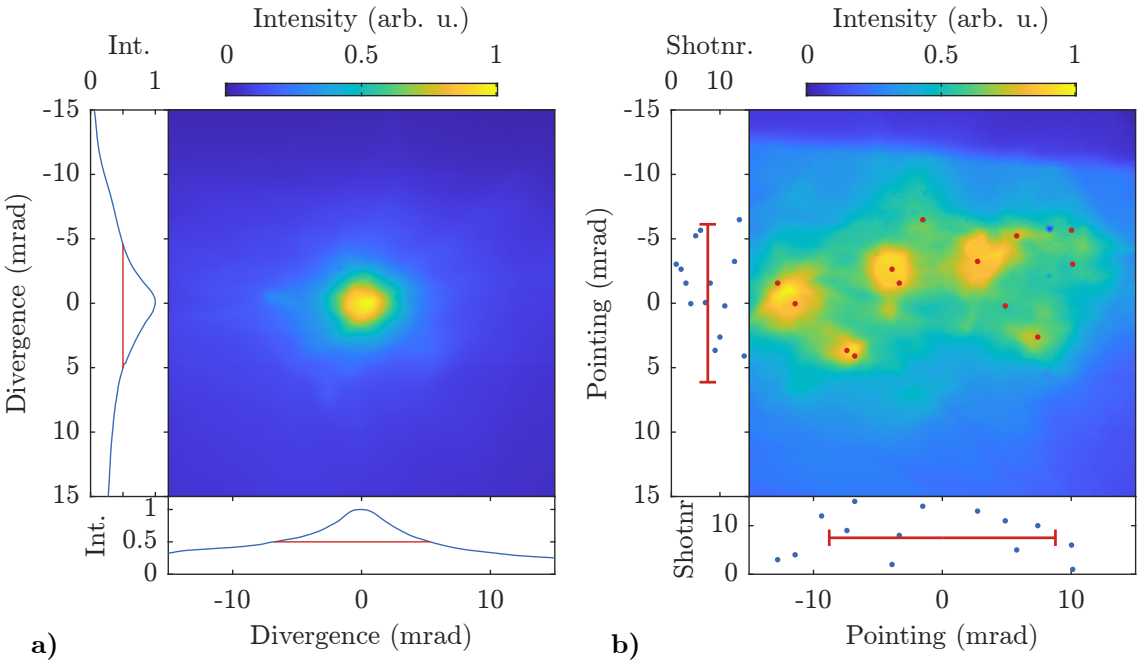

Figure 4.7: (a) average beam profile of 15 self injection shots. The FWHM divergence in the horizontal and vertical plane is depicted on the respective sides of the profile. (b) integrated beam profile and pointing of single shots. The standard deviation of the pointing stability is depicted on the sides of the integrated profile.

In Fig. 4.7a, the average beam profile and divergence of 15 shots and its divergence is shown. The unsymmetrical beam shape of single shots is still visible in the average profile and leads to wide background wings over the entire range of ±15 mrad shown here in the horizontal and vertical axis of the profile image. The resulting FWHM divergence of the average beam profile is 12.1 mrad in the horizontal and 9.6 mrad in the vertical axis, while Gaussian fits of the single shots resulted in (25.3 ± 8.6) mrad for the horizontal divergence and (17.1 ± 6.5) mrad in the vertical axis. The difference of the two values can again be explained by the irregular beam halo of the self-injection electron beams.

The sum of the profile images of the 15 shots depicted in Fig. 4.7b indicates the integrated electron profile of a run with multiple shots and is vastly different from the average profile, showing the high pointing fluctuations of the method, even for optimised conditions. The standard deviation of the pointing is again higher in the horizontal axis, with 8.8 mrad compared to 6.1 mrad in the vertical axis. Single shots are even outside the

range of ±15 mrad around the mean pointing depicted here, which was chosen for better visibility and comparison to the other methods.

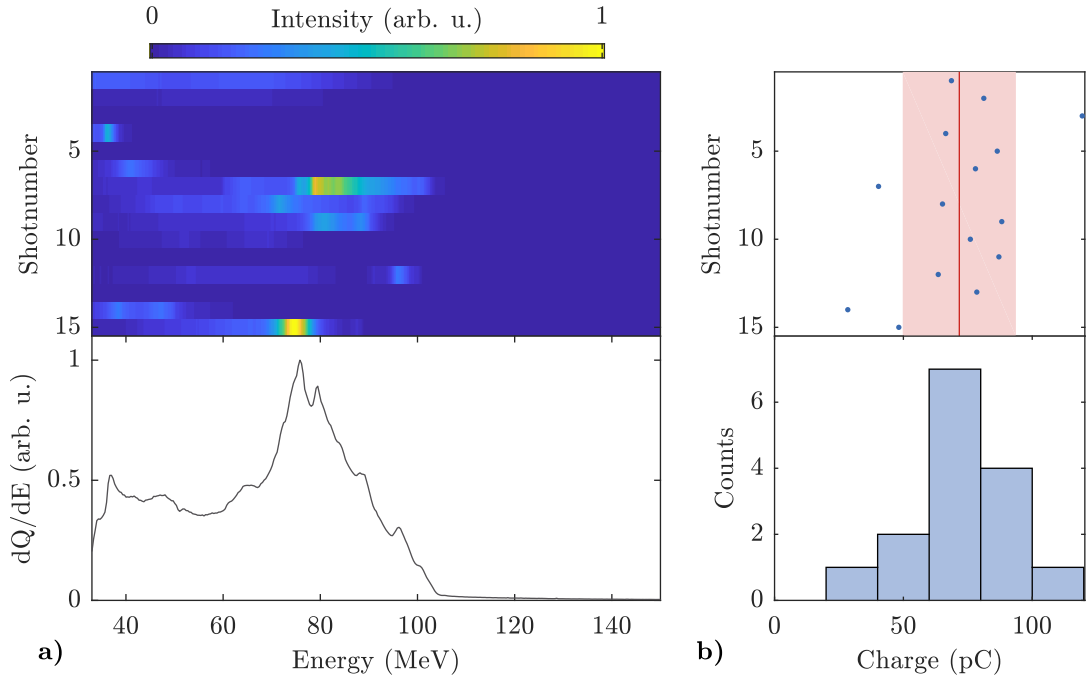

Figure 4.8: (a) Waterfall image (top) and integrated energy spectrum of 15 self-injection electron beams (bottom). (b) charge of the corresponding beams measured using the DaMon.

The large pointing fluctuation is also visible in the waterfall plot shown in the upper half of Fig. 4.8a. In combination with the charge measurements shown at the top of Fig. 4.8b, it seems that, due to the bad pointing, almost 50% of the shots shown here miss the electron spectrometer entirely, as charges of at least 30 pC were measured for all of those beams using the DaMon. Figure 4.8a does indicate some quasi monoenergetic shots with peaks around 80 MeV, but the overall stability of the beams in terms of energy is very poor as can be seen in the integrated energy spectrum. Despite the fact that charge was injected for each of these 15 shots, the charge stability suffers from major fluctuations as well, resulting in a mean charge of (71.7 ± 22.0) pC per shot.

Overall, self injection was found to be unstable in the described setup, despite the fact that with sufficient laser power and plasma density, reliable injection of charge was possible. The stabilisation of the injection technique, which highly depends on non-linear processes such as self-focussing, turned out to be very difficult. Overall, the stability of these beams is comparable to the beams achieved in early self-injection setups, which had similar parameters as here [18–20]. In order to produce more stable beams using this injection technique, the experimental parameters and especially the plasma density would have to be stabilised, as has been shown previously [55]. The standard deviation of the energy in the last amplifier stage resulted in a stability of 0.9%, such that the instabilities are most likely originating from the plasma instabilities.

4.2.2 Shock-front injection

To test shock-front injection, a blade was installed between gas jet and incoming laser beam to create a shock in the density profile and inject particles as described in Sec. 2.4.2. To adjust the position of the density peak, the blade was placed on a motor stage that moved parallel to the laser and electron axis. To align the blade in the horizontal axis, the size of its image and the diffraction rings were minimized using the transverse probe laser also used for density measurements.

The electron beams injected by the shock front were again optimised for different backing pressures, laser energies and laser-pulse durations. In addition, the position of the blade was changed to optimise the injection process. Moving the blade all the way out away from the gas jet stopped the injection, indicating that the laser was below the self-injection threshold and therefore operating in a more controlled way.

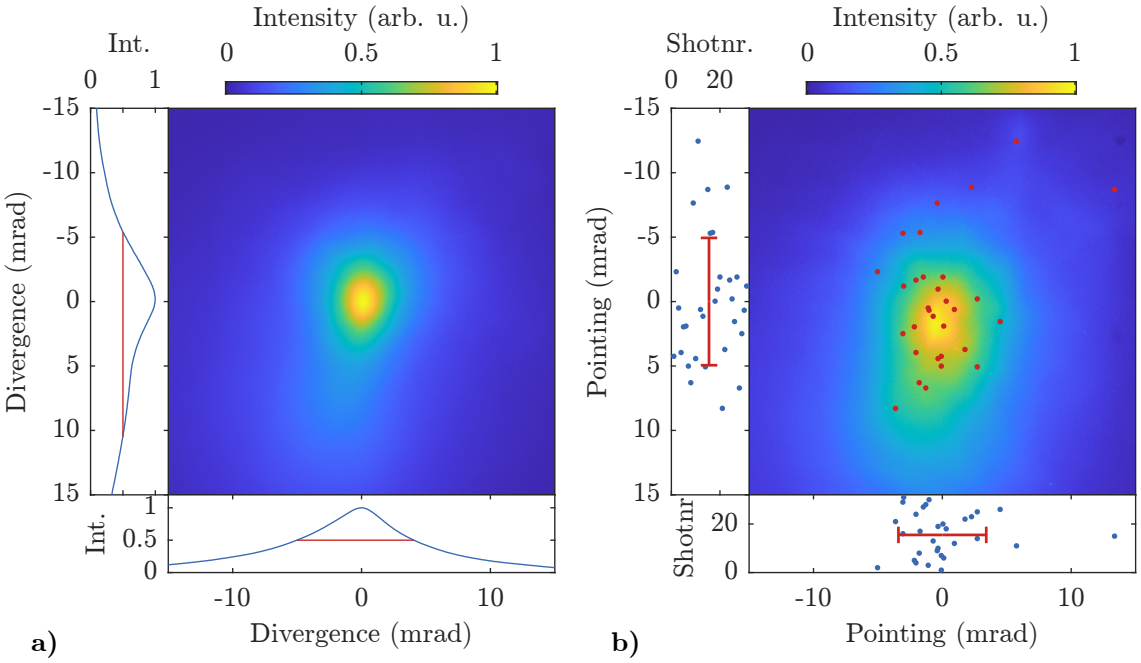

Figure 4.9: (a) average beam profile of 25 shock-front injection shots. The FWHM divergence in the horizontal and vertical plane is depicted on the respective sides of the profile. (b) integrated beam profile and pointing of single shots. The standard deviation of the pointing stability is depicted on the sides of the integrated profile.

Results of the optimisation are depicted in similar plots as for self injection in Fig. 4.9 and Fig. 4.10. As can be seen in Fig. 4.9a, the average beam profile for 30 shock front injected beams is cleaner compared to the self-injection case discussed before. The bottom tail of the average profile was later linked to residual fields of the spectrometer magnet, indicating that a substantial part of the total charge is coming from low-energy electrons. As no profile data of these beams exists without the magnetic field present, the divergence of these beams in the vertical axis is most likely overestimated. The resulting FWHM divergence for the average profile is 9.1 mrad in the horizontal and and 15.9 mrad

in the vertical axis. Gaussian fits of the single shots resulted in FWHM divergence of (11.0 ± 8.6) mrad in the horizontal and (13.7 ± 7.2) mrad in the vertical axis. The high standard deviation of these values could originate from the difference in the spectra of single shots and therefore different beam divergences, e.g. small divergences for peaked spectra and high divergences in case of electron beams with a broad energy spectrum. The integrated beam profile and the pointing stability shown in Fig. 4.9b shows an improvement of the pointing stability of the shock-front beams compared to the self-injection beams. Nevertheless the resulting integrated profile in Fig. 4.9b is still clearly bigger than the average profile of the beams corrected by their pointing fluctuations depicted in Fig. 4.9a. The pointing stability of the 30 shots is 3.4 mrad in the horizontal and 4.9 mrad in the vertical direction, which is substantially smaller than in the case of self injection.

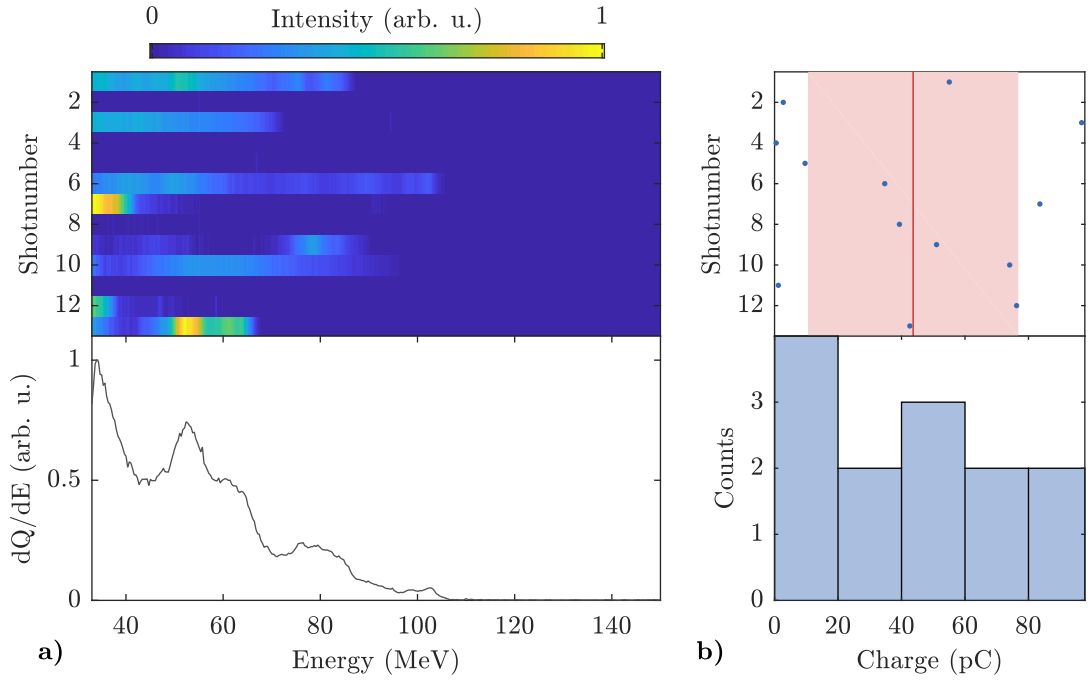

Figure 4.10: (a) Waterfall image (top) and integrated energy spectrum of 13 shock-front injection beams (bottom). (b) charge of the corresponding beams measured using the DaMon.

In contrast to the pointing stability, the spectral stability of the shock-front injected beams did not improve, as can be seen in Fig. 4.10a. Both waterfall plot and integrated spectrum in the figure show that quasi mono-energetic shots are achievable using this technique. Stable injection of beams was however not possible, as can also be seen by looking at the charge plots in Fig. 4.10b. In the case of two out of 13 shots, no charge at all was injected and two more shots had charges of less than 3 pC. In addition, the charge fluctuated a lot, leading to an average charge of (43.7 ± 33.1) pC.

Overall, the shock-front injected beams were not very stable in terms of energy and more degrees of freedom for the blade such as height or rotation would probably have been necessary to achieve reproducible beams using this injection method. In addition, small

fluctuations of the gas backing pressure could again lead to instabilities of the produced beams, as the dynamics of the injection would change for different gas densities. The laser energy in the last amplifier stage had a standard deviation of 1.2% during the experiments. Overall, the stability of previous experiments using this technique with slightly higher laser energy could not be reproduced [56]. It should however be noted that a positive effect of an increase in the laser power to 40 TW was already described in the experiments by Buck *et al.* [56]. As adjustments required for the tuning of the shock could not be implemented in the described system and the overall stability shown here was far from sufficient for the planned Thomson experiments, shock-front injection was not pursued further.

4.2.3 Ionisation injection

The third injection method tested was ionisation injection, which already produced reliable injection in experiments using the sapphire capillary. Both nitrogen and argon were tested as doping species with different doping percentages. In addition, both 1 mm and 3 mm nozzles were used as plasma targets. The results of the optimisation are again divided into two figures with divergence and pointing of the beams shown in Fig. 4.11 and charge and energy of the beams depicted in Fig. 4.12.

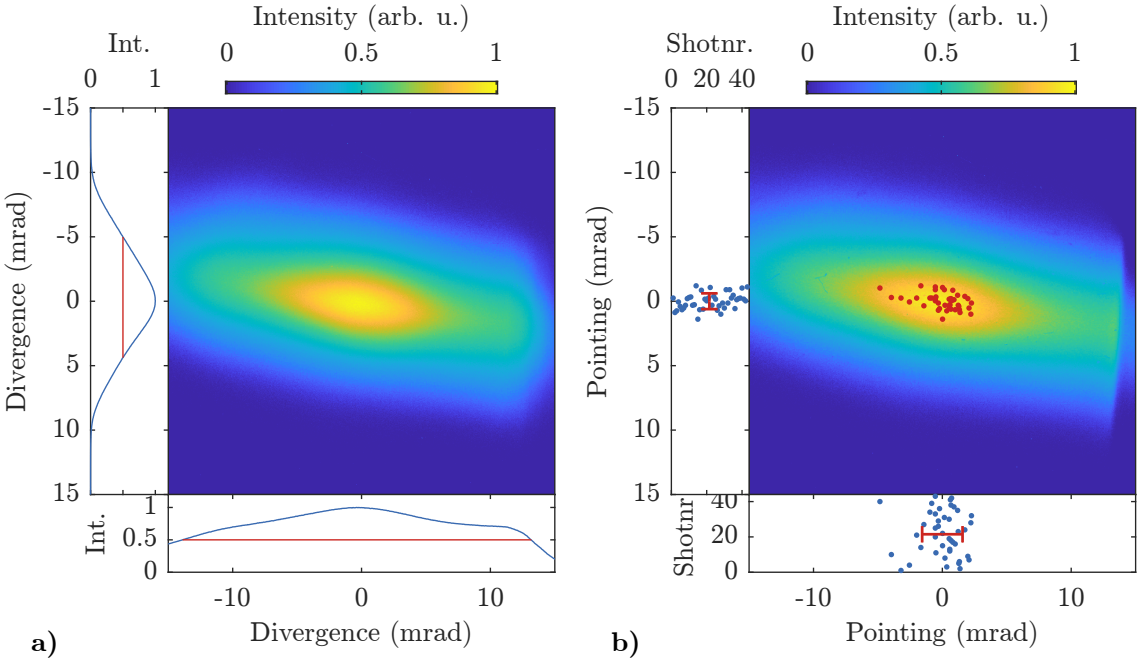

Figure 4.11: (a) average beam profile of 50 ionisation injection shots. The FWHM divergence in the horizontal and vertical plane is depicted on the respective sides of the profile. (b) integrated beam profile and pointing of single shots. The standard deviation of the pointing stability is depicted on the sides of the integrated profile.

In Fig. 4.11a, again the average beam profile is shown with its divergence. Compared to the previous electron beams, the divergence of the average profile is much larger, especially in the horizontal axis, which in this case is also the laser polarisation axis. The high

divergence of the beam indicates that there is a large contribution from lower energy electrons, as expected in the case of continuous injection due to the ongoing ionisation of the doping gas. The elongation of the ionisation injection profile in one axis was already present in the first publications using this injection method [67] and was previously linked to the laser polarisation [151]. The FWHM size of the average profile with 27.1 mrad in the horizontal and 9.4 mrad in the vertical direction is very similar to the divergence value of Gaussian fits to single shots, leading to (27.1 ± 0.9) mrad in the horizontal and (9.3 ± 0.6) mrad in the vertical axis, meaning that, despite the large divergence of the beams, they are accelerated in a stable way.

Stable acceleration is also visible in the pointing of the beams depicted in Fig. 4.11b, resulting in a standard deviation of 1.6 mrad in the horizontal axis and 0.6 mrad in the vertical axis. Consequently, the average electron beam looks very similar to the integrated profile of an entire run, which was not the case using the other two injection techniques presented before.

In addition to pointing and divergence stability, the advantages of ionisation injection are also visible when looking at spectral and charge stability in Fig. 4.12. In the waterfall plot on the top half of Fig. 4.12a, similar spectra are visible for most of the 30 shots displayed here. As a downside, continuous injection is also indicated in the integrated spectrum at the bottom half of the graph, suggesting a long tail of low-energy electrons for the energies below 35 MeV not measured by the high-energy spectrometer screen.

In terms of charge plotted in Fig. 4.12b, again the stability of the ionisation injection beams exceeds that of the other two techniques, resulting in 100% injection for the 30 shots shown here with an average charge of (46.1 ± 8.6) pC per shot. The standard deviation of the laser energy in the last amplifier stage was again 1.2%.

Overall, ionisation injection offered more stable beams compared to the other two injection techniques, as is also shown in Tab. 4.1, where the most important characteristics of the achieved beams are compared. Compared to the other techniques, the only major disadvantages are the larger beam profiles and broader electron spectra due to the continuous injection process. In addition, similar reproducible beams were also achieved using a variety of different parameters, such as different gas-doping species or different doping percentages. Furthermore, electron charge, energy and pointing could be tuned e.g. by changing the laser energy, as shown in Sec. 4.3. Therefore, ionisation injection was chosen as the injection mechanism for future experiments and was optimised further.

	Self injection	**Shock-front injection**	**Ionisation injection**
Divergence (mrad^2)	12.1 x 9.6	9.1 x 15.9	27.1 x 9.4
Pointing (mrad^2)	8.8 x 6.1	3.4 x 4.9	1.6 x 0.6
Charge (pC)	71.7 ± 22.0	43.7 ± 33.1	46.1 ± 8.6
Bandwidth	peaked	peaked	continuous
Spectral stability	poor	poor	good
Robustness	poor	poor	good

Table 4.1: Comparison of the electron beams achieved using different injection techniques.

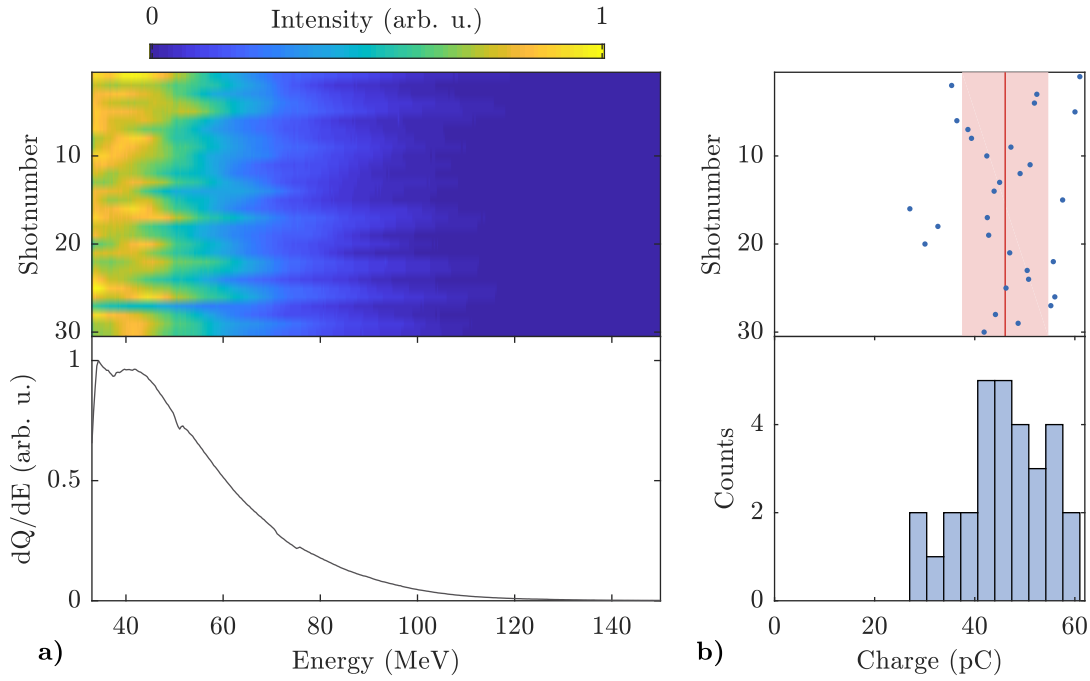

Figure 4.12: (a) Waterfall image (top) and integrated energy spectrum of 30 ionisation-injection beams. (b) charge of the corresponding beams measured using the DaMon.

4.3 High repetition rate self-truncated ionisation injection

After the injection tests, the ionisation injection beams were further improved to meet the requirements for the planned Thomson experiments. In addition, the repetition rate of the system was increased to enable faster data taking and consequently speed up the further optimisation process. For the Thomson experiments, the electron stability, especially in terms of charge and spectral stability, needed further improvement and the energy had to be increased to reach a high charge density at the target energy of about 64 MeV required for medical imaging experiments. The process of the electron optimisation towards stable high-repetition-rate acceleration is described in this section.

4.3.1 Increasing the stability and repetition rate

Two main problems in producing stable electron beams at high repetition rate were related to gas issues for the plasma creation. First of all, the repetition rate for the electron acceleration was limited by the amount of residual gas in the vacuum chambers for all electron beams described above. In addition, the fluctuations of the gas density and subsequently the fluctuation of the plasma density of consecutive shots exceeded the variations of laser parameters for these shots and had therefore had a high influence of the electron stability. Therefore, two modifications to the setup were made to minimise residual gas in the system and to stabilise the backing pressure.

In order to protect the compressor gratings and mirrors in the system from the high-intensity laser beam, the ambient pressure in the compressor was kept below 1×10^{-4} mbar. By firing the gas jet or filling the sapphire capillary, the pressure in the LPA chamber and the vacuum compressor exceeded this value to pressures on the order of 1×10^{-2} mbar. Using the pumps attached to the system, it took tens of seconds to pump this gas out of the system to a level where another shot could be fired. Therefore, a differential pumping line was added to the chamber. A cube with 2 mm openings for in- and out-coupling of laser and electron beam and windows for the transverse probe beam was put around the gas jet. The gas jet was mounted on three stages for translations in all three dimensions and attached to the bottom of the cube using flexible bellows to seal the bottom of the cube. The top of the cube was then connected to a large external pump via an additional vacuum line inside the LPA chamber as depicted in Fig. 4.13a, which shows a 3D drawing of the differential pumping system. Due to the installation of the differential pumping line, the pressure in the LPA chamber stayed at levels of 5×10^{-5} mbar when firing the gas jet with a backing pressure of 6 bar helium and an opening time of 7 ms at a repetition rate of 10 Hz, which exceeded the opening durations of 4 ms and backing pressured around 5 bar used in daily operation. Even for a backing pressure of 17 bar, and the same repetition rate and opening time as in the 6 bar case, the pressure in the LPA chamber only increased to about 2×10^{-4} mbar, as can be seen in Fig. 4.13b. During all these tests, the pressure in the vacuum compressor tank was lower than the pressure in the LPA chamber by about one order of magnitude.

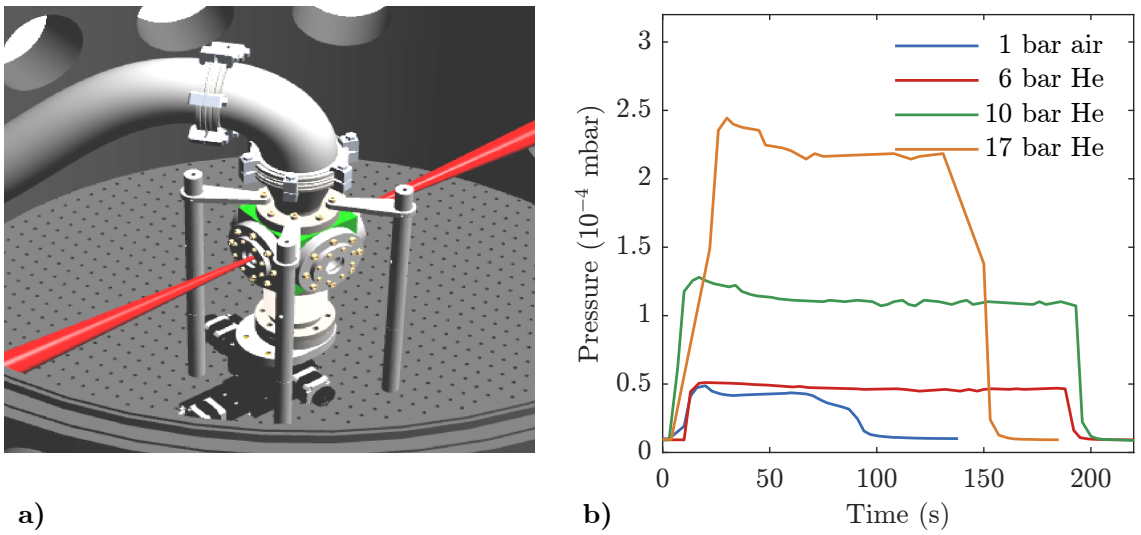

Figure 4.13: (a) 3D drawing of the differential pumping cube inside the chamber. (b) pressure in the main interaction chamber when firing the gas jet wit different pressures at a repetition rate of 10 Hz.

The implementation of the differential pumping cube would therefore allow even higher backing pressures or repetition rates and the gas load was no longer the limiting factor after this upgrade to the system. The cube was later changed to a cone with an 8 mm

opening directly above the gas jet for more flexibility. Even after this change to the differential pumping system, the gas load did not exceed the limit of 1×10^{-5} mbar in the compressor when firing at maximum repetition rate of 10 Hz and backing pressures of 3 bar to 5 bar used in daily operation. A photograph showing a helium plasma in the differential pumping cube during active plasma lens experiments is depicted in Fig. 4.14.

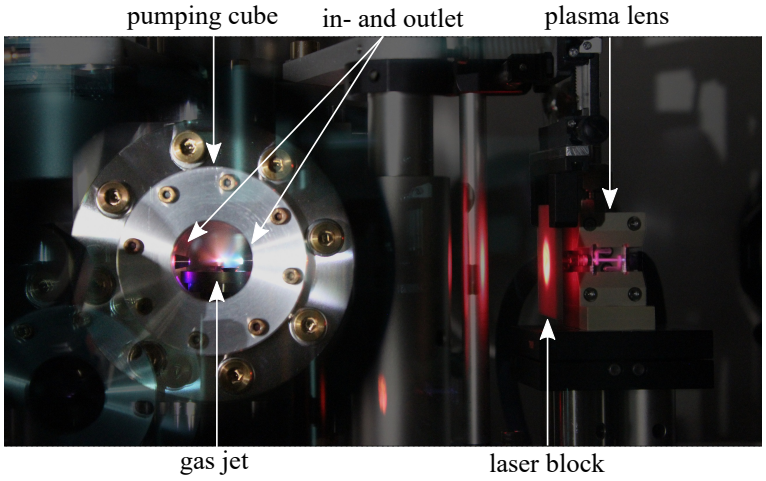

Figure 4.14: Photograph of a helium plasma in the differential pumping cube and hydrogen filled active plasma lens. The in- and outlets for laser and electron beam are visible through the window of the differential pumping cube, which are used for interferometry images using the transverse probe. In front of the plasma lens, the laser is blocked by a ceramic with a small hole for the electron beam.

In Fig. 4.13b, small peaks at the beginning of the pressure tests are visible for the different backing pressures, indicating the higher backing pressures for the first tens of seconds after starting to pulse the gas jet at 10 Hz. These problems point to the second issue with the gas system. The peaks originate from the manual gas valves used to set the backing pressure. The slow response time of these valves leads to a decrease of the backing pressure while firing the gas jet until a steady-state backing pressure below the original set point is reached. This is depicted in Fig. 4.15a, where backing pressure and chamber pressure are shown in more detail for the 10 bar helium case from Fig. 4.13b. For the first 50 s after starting to pulse the gas jet, the backing pressure decreases by about 1.5 bar - more than 10% of the original set point - and a new steady-state level is reached at about 10 bar. When the pulsing of the gas jet is stopped after 200 s, the backing pressure increases slowly until the original set point is reached after about one minute.

Therefore, the manual gas valve was exchanged to an electronic feedback system, which monitors and adjusts the gas pressure constantly. A comparison of the backing pressure using this feedback system is shown in Fig. 4.15b. In the figure, no difference of the backing pressure is visible within the region within which the gas jet is fired (0 s to 200 s) or when the gas jet is closed. In addition, the standard deviation of the backing pressure over the entire duration shown here is only 0.8%, therefore allowing for a more stable

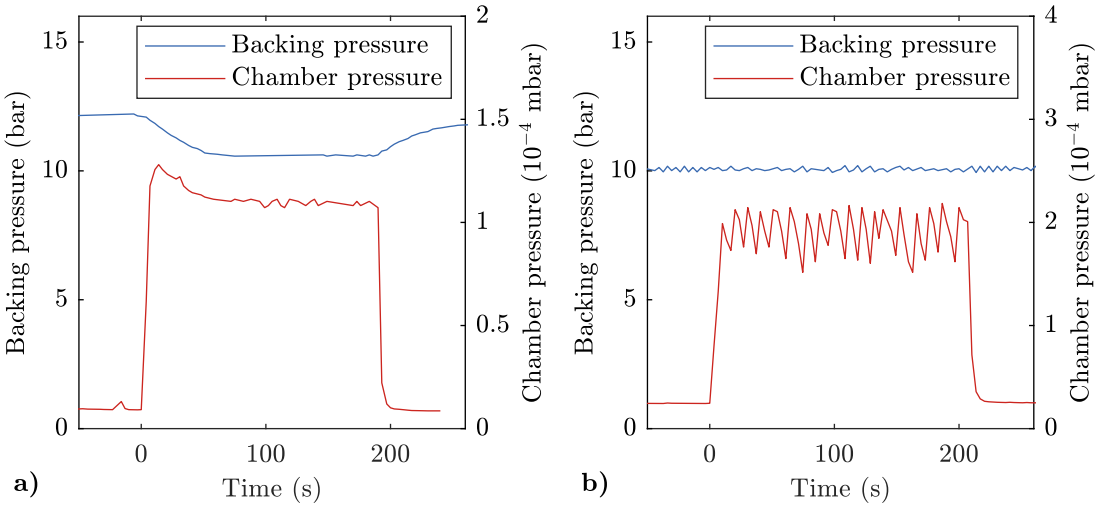

Figure 4.15: (a) backing pressure of the gas jet and ambient chamber pressure (indicating times when the gas jet is fired) using manual pressure valves. (b) backing pressure of the gas jet and ambient chamber pressure (indicating times when the gas jet is fired) using the feedback controlled electronic gas valves.

operation of the gas jet than before. The electronic gas valve also enabled faster and more detailed studies of the plasma density for further optimisation of the electron beams, as the setpoint can be controlled from outside the BOND lab and reaches a new level within a few seconds.

In addition to the plasma-density stability, the laser stability is another important factor for stable electron acceleration. During the injection tests described above, the laser was operated within its design stability described in Sec. 3.1. Regular laser maintenance helped to keep the laser system within the design parameters over the entire duration of data taking for this thesis. The energy stability for example, which was mostly influenced by the stability of the pump lasers was monitored on a daily basis and regular change of the pump laser flashlamps allowed to operate at the design energy with a standard deviation of about 1.5%. Therefore, only small changes to the system were made, e.g. an automatically rotating mount for the saturable absorber in the Booster unit of the laser system, allowing for the stable operation of the laser and especially a high spectral stability over longer durations without the need to manually tune the laser system.

4.3.2 Transition to self-truncated ionisation injection

To bring up the beams to higher energies and decrease their spectral bandwidth, the ionisation-injection beams had to be further improved. The continuous ionisation of the doping gas and subsequently large energy spread of ionisation-injection electron beams was already witnessed in the first experiments demonstrating the technique [66–68]. Nevertheless, several experiments managed to mitigate the problem and decrease the energy spread of the ionisation-injection beams. One possibility is to restrict the doping gas to

a small region of the target. This can either be done by controlled doping into a small region [62] or by using a two-stage acceleration setup [72, 152]. However, due to the use of a short gas jet, these modifications were not possible here. Another possibility to reduce the energy spread is the transition to a regime of self-truncated ionisation injection. This injection method has been shown to accelerate quasi mono-energetic beams in a stable manner in previous experiments [74–76]. As described in Sec. 2.4.4, this mechanism is based on the self-focussing of the laser and the subsequent deformation of the wakefield, breaking the trapping condition of the ionised gas.

Consequently, comprehensive scans of focus position, laser energy and plasma density were performed to find the correct parameters for self-truncated ionisation injection in the setup used. The improvements to the gas system and the high-repetition-rate upgrades helped to find a parameter set where the beam size is substantially decreased compared to the ionisation-injection beams described in the previous section. This already indicates the transition to STII, as the divergent, low-energy electrons are not present in the profile images depicted in Fig. 4.16.

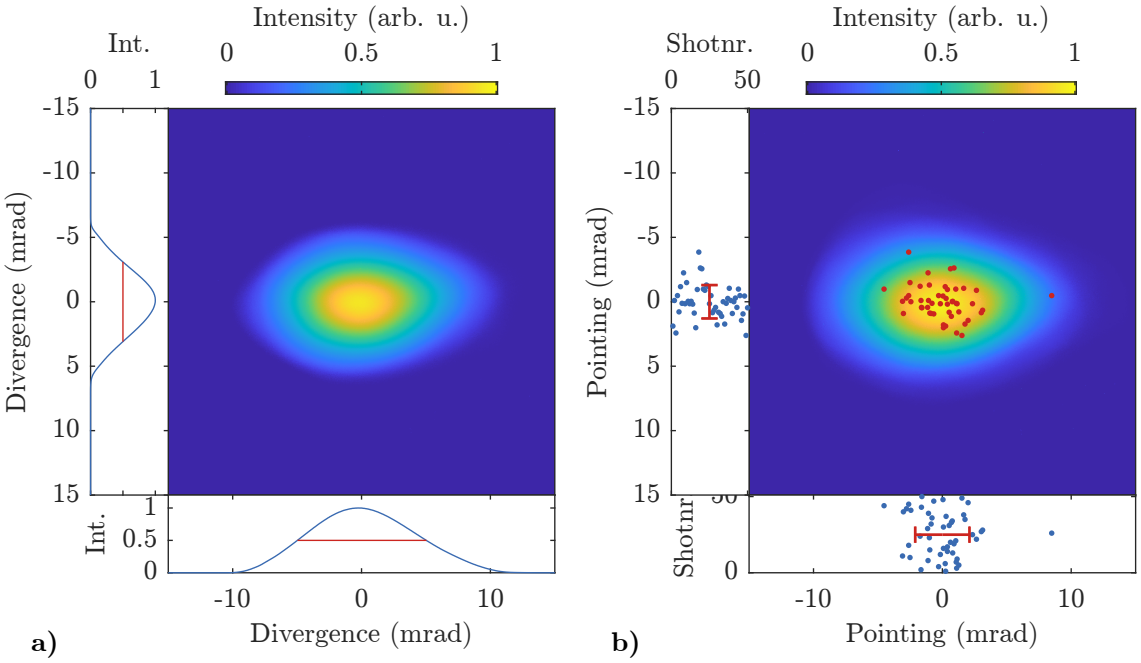

Figure 4.16: (a) average beam profile of 50 self-truncated ionisation-injection shots. The FWHM divergence in the horizontal and vertical plane is depicted on the respective sides of the profile. (b) integrated beam profile and pointing of single shots. The standard deviation of the pointing stability is depicted on the sides of the integrated profile.

Similar to the II beams, the average profile of the 50 consecutive STII shots shown in Fig. 4.16a is widened on the axis of the laser polarization. In comparison to the previous II beams, the divergence of these beams decreased, now reaching values of 10.0 mrad in the horizontal and 6.2 mrad in the vertical axis, which is lower by a factor of two to three in both axes. Gaussian fits to the divergence of single shots leads to a divergence of

(9.6 ± 0.8) mrad by (5.9 ± 0.3) mrad, indicating the stability of this process. The integrated beam profile depicted in Fig 4.16b is again not much larger than the average beam profile, due to the small pointing fluctuations achieved using this technique. This is similar to the stability achieved using II and results in a standard deviation of 2.1 mrad in the horizontal axis (1.7 without the outlier of shot 26) and 1.3 mrad in the vertical axis.

The transition to a peaked spectrum without the low energetic tail is also visible when looking at the energy in Fig. 4.17a. Most of the charge is in the energy range between 60 MeV to 85 MeV, as can be seen in the integrated spectrum shown in the bottom half of the plot. Therefore, the target energy of 64 MeV is well within the energy range achievable using STII. The waterfall plot shown in the upper half indicates a stable acceleration of these beams both in terms of energy and charge. This is also supported in the charge plot in Fig. 4.17b, showing an average charge of 20.8 pC with a standard deviation of 3.6 pC for the 50 consecutive shots shown here.

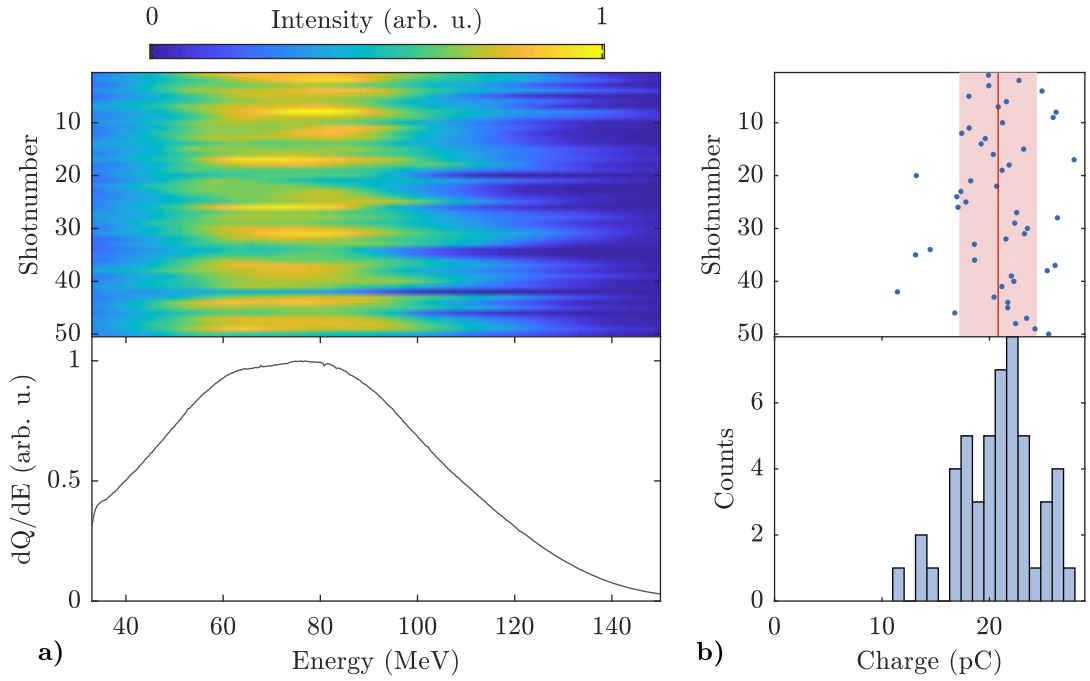

Figure 4.17: (a) Waterfall image (top) and integrated energy spectrum of 50 self-truncated ionisation injection beams. (b) charge of the corresponding beams measured using the DaMon.

Using this new injection regime, some tuning of the electrons is also possible by changing the laser energy. This can be seen in Fig. 4.18, where 50 shots with the same parameters as in Fig. 4.17 are shown, but the laser energy is decreased by 25%. This laser energy is at the edge of the necessary energy required for STII, as can be seen in the charge and waterfall plot of the figure. The peak of the spectrum decreases to an energy of about 57 MeV at these conditions, which is about 20 MeV less compared to the case with more laser energy. The decrease of the peak electron energy comes at the cost of also reducing the charge, as can be seen in Fig. 4.17b. The mean charge decreases to (3.0 ± 1.8) pC and

eight out of the 50 shots shown have a charge of less than 1 pC. However, an analysis with the sensitive channel of the DaMon shows that charges of at least 390 fC were injected, which is almost an order of magnitude above the noise level.

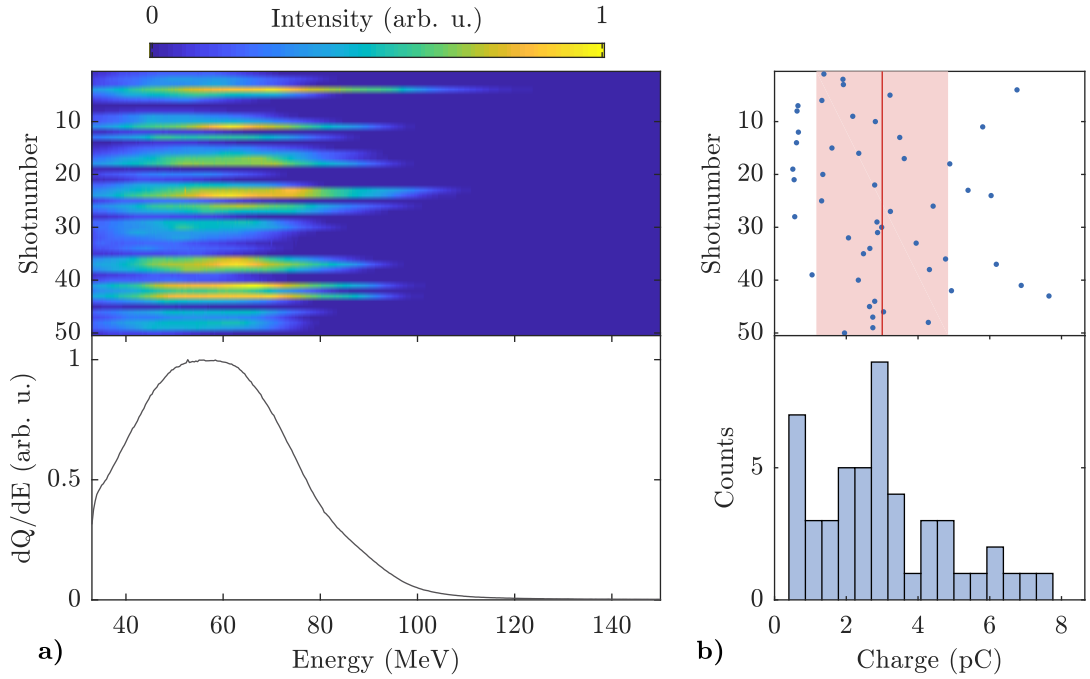

Figure 4.18: (a) Waterfall image (top) and integrated energy spectrum of 50 self-truncated ionisation injection beams. (b) charge of the corresponding beams measured using the DaMon. In comparison to the energies and charges in Fig. 4.17, the laser energy was decreased by 25%.

Overall, the use of STII allowed the production of electron beams with smaller divergences and pointing stability comparable to that achieved in the II case. In addition, spectra peaked around the design energy of 64 MeV are easily achievable using this technique, making it an excellent choice for future Thomson experiments as both a diagnostic and in medical imaging.

4.3.3 Particle-in-cell simulations

The simulations shown here were done to recreate the beams used in Thomson experiments which will be described in Chapter 5. The electron beams are similar to those shown in Fig. 4.18, as a low charge was required for the experiments as will be explained later. The simulations will be used to explain some features of the injection technique using parameters that could not be measured during the experiment and to show the interplay of plasma density, laser intensity and focal plane for STII.

The simulations were done with a simplified density profile based on the measured density profile using the interferometer setup described in Sec. 3.2. A comparison of these profiles in shown in Fig. 4.19.

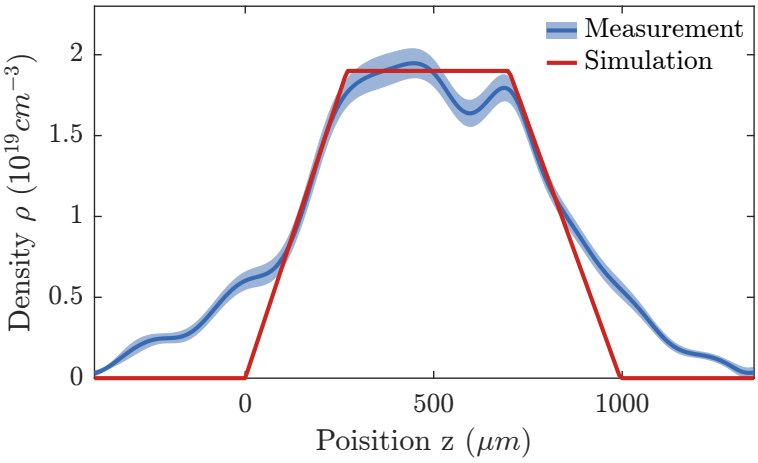

Figure 4.19: Comparison of the measured density profile with the standard deviation (blue curve) and the density profile used for simulations (red curve).

For the laser, a vacuum peak intensity of $a_0 = 0.81$, a $1/e^2$ (approximately 0.135 of the intensity maximum) beam waist of 8.8 µm and a pulse duration of 30 fs was chosen, which is similar to the parameters used in the experiment. The simulation results were compared to experimentally measured values averaged over 300 shots. The charge in the experiment of (2.7 ± 1.0) pC agrees well with the simulated charge of 2.0 pC, as do the measured divergence of (3.9 ± 0.7) mrad $\times$ (7.4 ± 1.6) mrad and simulated divergence of 3.9 mrad $\times$ 7.1 mrad.

To be able to compare the spectra of the simulated electron beam and the measured electron beam, the broadening effects described in Sec. 3.2.2 have to be applied to the simulated beams. As mentioned earlier, the broadening of the electron beam is dependent on the divergence of the electron beams. However, the divergence of the electron beam is energy dependent, as the simulation reveals and is shown in Fig. 4.20a. Therefore, the electron beam cannot be simply multiplied by a tracking matrix such as the example depicted in Fig. 3.18 to include the broadening from divergence effects. Instead, the broadening of the respective energies has to be studied independently. For the beams of the simulation, this was done for five different energies between 40 MeV and 80 MeV. The resulting FWHM broadening of these five energies and their divergences are depicted in Fig. 4.20b. The higher dispersion of high-energy electrons is compensated by their decrease in divergence, such that the resulting FWHM spread on the spectrometer screen is around 9 mm for all depicted energies. To further simplify the calculation of the broadening due to the electron beam divergence, the value of 9 mm was therefore used for all electron energies.

To estimate the broadened of the spectrum due to the pointing fluctuations, again tracking simulations using the five energies depicted in Fig. 4.20 were performed. For each input energy, the tracking was done with seven different pointing offsets between -3 mrad and 3 mrad and including the energy dependent divergence. This is shown for 40 MeV electron in Fig. 4.21a and for 80 MeV in Fig. 4.21b. The resulting energy

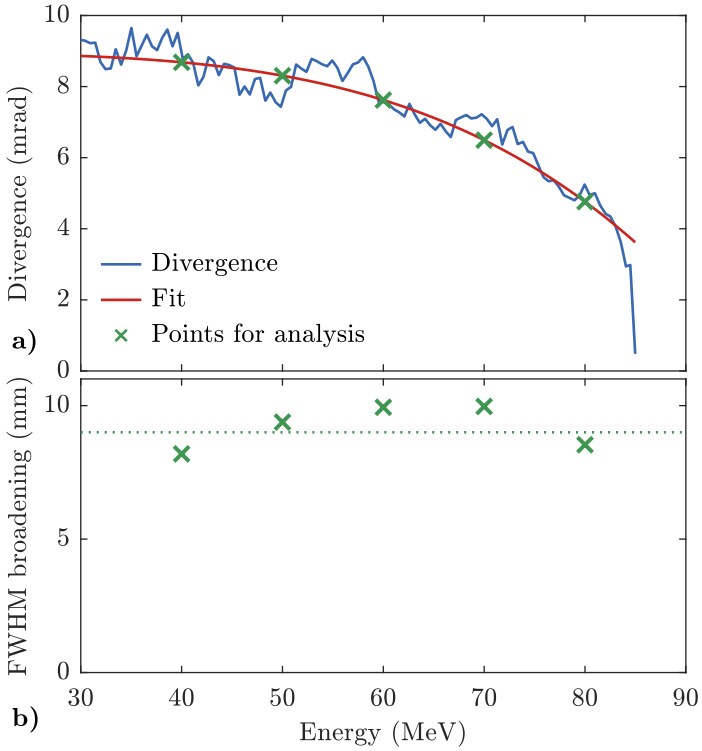

Figure 4.20: Energy dependent divergence of the electron beams and the resulting broadening on the electron spectrometer screen. a) energy dependent divergence of the electron beams according to PIC simulations (blue lines), a fit (red line) and five points of the fit, which were used for further analysis of the broadening on the spectrometer screen (green x). b) The FWHM of the signal on the spectrometer screen for energies between 40 MeV and 80 MeV with the respective divergences plotted in panel a). The green dotted line marks the level of 9 mm.

dependent broadening of the signal on the screen as a function of the pointing fluctuations is depicted in Fig.4.21c. A linear fit of the offsets for the five energies leads to a broadening term of 0.017 mm/mrad/MeV.

In order to compare the simulated and the measured spectrum, the constant broadening terms from the imaging system and the divergence and the linear broadening term from the pointing fluctuations under the assumption of a standard deviation of the pointing of 2 mrad were used to calculate the signal of the simulated bunch on the spectrometer screen. Afterwards, the calculated screen signal was corrected according to the energy width as a function of the screen position. The energy spectrum of the simulation, the simulated spectrum including the broadening effects and the average spectrum of 300 shots from the Thomson experiments are depicted in Fig. 4.22. The energy distributions of the measurement and the broadened spectrum agree reasonably well. There is however a discrepancy, especially at higher energies. Overall, the energy of the measured spectrum seems to be 1 MeV to 2 MeV above the simulated case. This could be explained by simplifications made in the simulation, e.g. the simplified density profile or idealised laser parameters. Furthermore, the real pointing fluctuations or a pointing offset of the

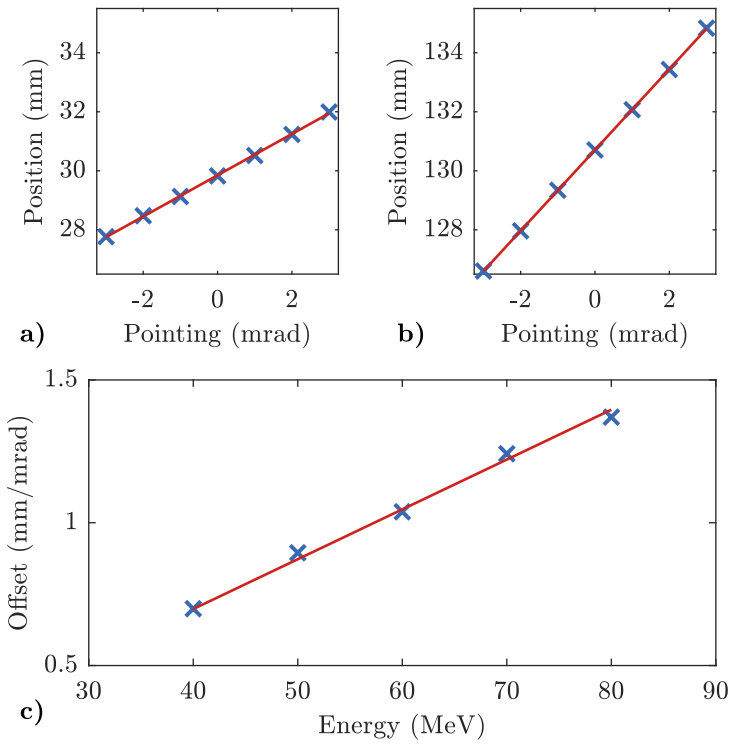

Figure 4.21: Broadening of the electron signal on the electron spectrometer screen originating from pointing fluctuations. a) Shift of the peak position on the screen for 40 MeV for pointing offsets between −3 mrad and 3 mrad (blue crosses) including a linear fit (red line). b) Shift of the peak position on the screen for 80 MeV electrons for pointing offsets between −3 mrad and 3 mrad (blue crosses) including a linear fit (red line). c) energy dependent broadening of the electron beams with energies between 40 MeV and 80 MeV (blue crosses) and a linear fit (red line).

beams could deviate from the assumed parameters, as these could not simultaneously be measured with the electron spectrum. In addition, the measured spectrum is averaged over 300 shots, such that electron bunches with different electron distributions would lead to further broadening effects and remove any substructure in the measured electron distribution.

The simulation enables a more detailed study of the injection technique. For example the evolution of the laser strength a_0 inside the plasma, which can not be experimentally measured, can be studied using PIC simulations, which is shown in Fig. 4.23. As can be seen in the figure, the laser intensity increases via self focussing inside the plasma channel to a value of about 1.8, exceeding the vacuum focus intensity by more than a factor of two. In contrast to other STII experiments, where the injection condition is truncated by further self focussing of the laser and bubble deformation, the laser intensity decreases shortly afterwards in this case. This is possible as the laser pulse is not guided inside the plasma. In total, the laser strength exceeds a value of $a_0 > 1.7$ required for the injection of the nitrogen dopant over a length of less than 200 µm, thus restricting the injection of charge to about the same length as was described in Sec. 4.2.3. The injection meachanism

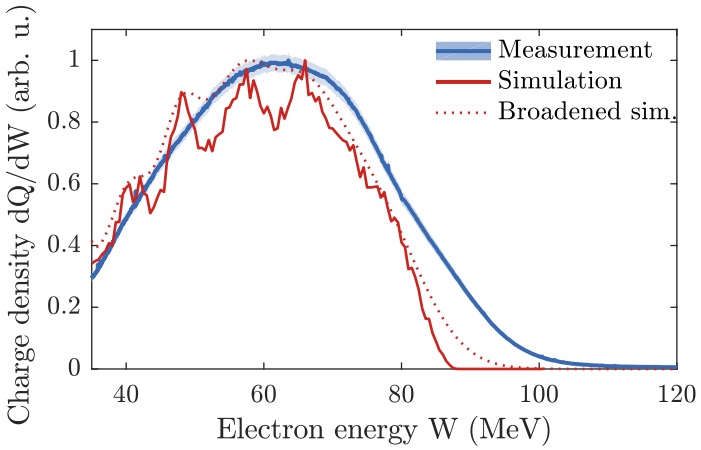

Figure 4.22: Comparison of the measured average electron spectrum of about 300 shots with its standard deviation and the electron spectrum from simulation. For a better comparison, the simulated spectrum is also depicted including the broadening effects of the spectrometer described in Sec. 3.2.2.

shown here describes the first experimental realisation of STII using a weakly relativistic laser as proposed by Kamperidis *et al.* [8].

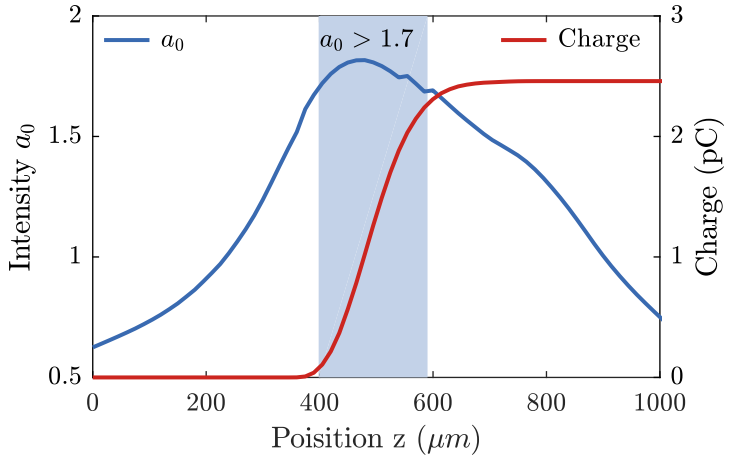

Figure 4.23: Evolution of a_0 and the charge inside the plasma. The light blue area marks the region of $a_0 > 1.7$, where ionisation of inner shell electrons of nitrogen is possible.

The importance of the injection length becomes visible when looking at Fig. 4.24, where the development of the mean energy of the simulated beam is depicted. For easier comparison, the injection region with an $a_0 > 1.7$ is again shown as the blue shaded region. At the position where the a_0 decreases again below the value of 1.7, the mean energy of the bunch is already at 20 MeV, almost 60% of the FWHM width of 35 MeV of the spectrum shown in the inset of the figure, making it a major contributor to the resulting bandwidth of the bunch. Further acceleration of such a bunch could therefore decrease the relative bandwidth of the electron bunches accelerated using this technique. It should be noted that the use of the mean energy in this graph leads to a lower final energy than use of the the peak energy of the same bunch depicted in Fig. 4.22.

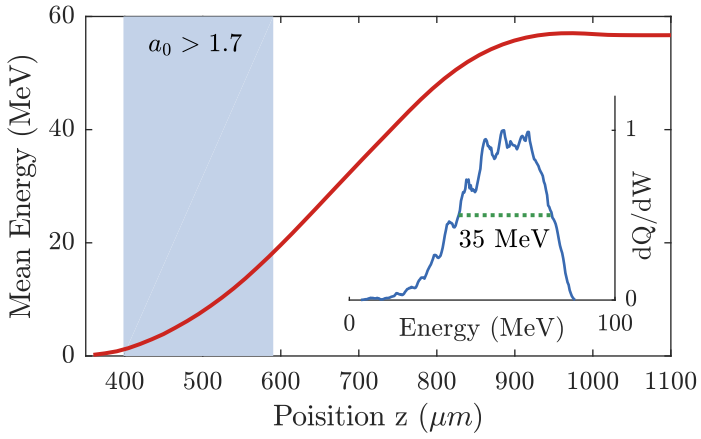

Figure 4.24: Evolution of the mean electron energy inside the plasma. The light blue area marks the region of $a_0 > 1.7$, where ionisation of inner shell electrons of nitrogen is possible. At the end of the injection length, the mean energy is already 20 MeV, almost 60% of the final FWHM energy spread of the final energy spectrum shown in the inset.

The simulations also offer an explanation why more stable beams can be achieved using this method than in the injection techniques discussed in Sec. 4.2. In Fig. 4.25, the energy evolution of the last 150 µm in the plasma for three different input intensities is shown. Both an increase in strength and a decrease of the laser strength by 1.25 %, which is similar to the standard deviation of the laser stability in daily operation, lead to a decrease of the final mean energy. Especially in the case of an increase in the laser intensity, this is surprising. An explanation is the matching of the acceleration length to the dephasing. In the simulation, the laser with a higher initial energy injects electrons earlier, as visible for red and orange lines in Fig. 4.25a. However, the electrons also dephase earlier which in total leads to a lower final energy than in the optimised case (blue line), as is visible in Fig. 4.25b. The opposite is the case for a lower laser strength (green and black lines), where the energy decrease from dephased electrons at the end of the plasma is smaller compared to the higher energies. Therefore, the final energies of the simulations with only a small change in the laser strength with respect to the nominal case reach similar energies. In total, the differences in the final energy for $a_0 \pm 1.25\%$ of 0.42% and 0.16% with respect to the mean energy in the original case are much lower than the change in laser strength of 1.25%. The interplay of the laser intensity, plasma density and focus position therefore leads to plateau region of the self focussing and subsequently of the electron acceleration, allowing a stable acceleration by cancelling out small fluctuations of the input parameters. The energy evolution of $a_0 \pm 5\%$ emphasises that this is a plateau effect, as in both cases the final mean energy is considerably lower than in the optimised case.

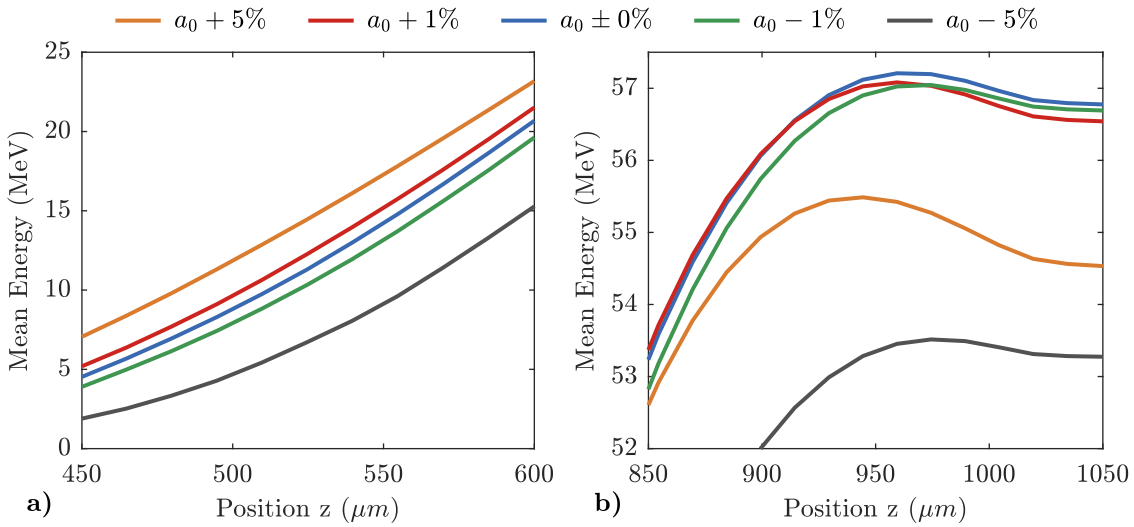

Figure 4.25: Evolution of the mean energy for different laser intensities. a) shortly after injection and b) at the end of the plasma down-ramp.

4.4 Long-term stability tests

The development of this stable, high-repetition-rate electron source enabled detailed stability studies of the produced beams. The data taking for a pointing stability test of 190 shots, as shown for the first electron beams in Sec. 4.1, would only take a little more than a minute compared to the 4 hours it took to get the data shown in Fig. 4.5. At the same time, the pointing fluctuation of the produced beams using the new injection technique decreased by a factor of 4, displaying the advances of the upgraded system and self-truncated ionisation injection. To show the capabilities of the electron source e.g. for use in medical imaging experiments such as XFI, a long-term stability run was performed over the duration of a full working day. The electron energy was tuned to be peaked at 64 MeV to meet the parameters required for XFI Thomson experiments [6]. Over the duration of 8 hours, a total number of 72000 shots were fired at a repetition rate of 2.5 Hz. The results of this stability test described in this section are also prepared for a separate publication [3].

Electron beams were successfully injected and accelerated in all of the 72000 shots, making it one of the highest amount of consecutive electron shots of an LPA experiment with energies of tens of MeV to date. As a reproducible flux is required for future applications of LPA experiments, the focus of the optimisation was on reliable and high average charge rather than minimising charge fluctuations. This was successful, as the average charge was roughly constant over the entire run duration as can be seen in Fig. 4.26, where the average charge of 100 shots is shown together with the standard deviation of these shots.

The mean charge was (14.5 ± 3.8) pC, which corresponds to a flux of about 2 nC per minute and adds up to more than 1000 nC for the 8 hour run. A linear fit of the charge

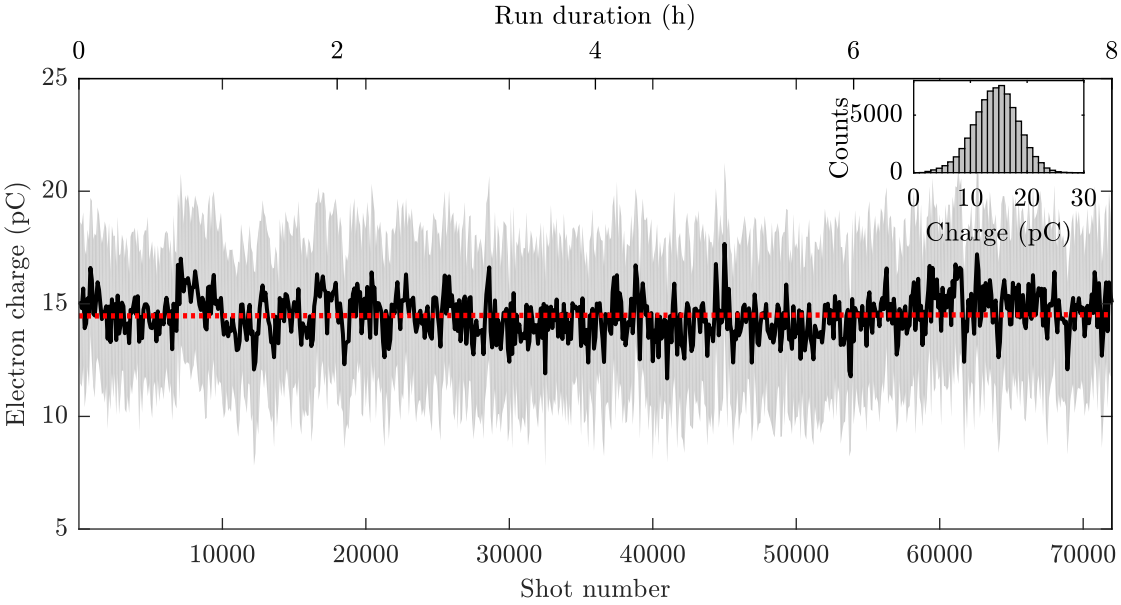

Figure 4.26: Measured charge as a function of shot number and time. The black line shows the average charge of 100 shots with its standard deviation as grey band as a function of time. A linear fit of all charge measurements is shown as the red dotted line. A histogram of the injected charge is shown in the inset.

as a function of shot number shows an average increase of 0.7 aC per shot, resulting in an increase of the mean charge by 0.05 pC or 0.3% after 72000 shots. The minimal measured charge of 1.5 pC is well above the noise level of (0.51 ± 0.01) pC of the high-charge channel of the cavity-charge monitor, showing that electrons were injected and accelerated in all of the 72000 consecutive shots.

The 2D electron divergence and 2D electron-beam pointing of the produced beams were discussed earlier in this chapter. As these measurements were only possible in an invasive way using the profile screen before the electron spectrometer, the pointing and divergence were only measured on the electron spectrometer screen in the non-dispersive (horizontal) axis. Results of the divergence and the pointing of these electron shots are shown in Fig. 4.27. The pointing stability in Fig. 4.27a is plotted as an average of 100 shots at each position with the standard deviation of those shots as the grey band. In the figure, a slow drift from -1 mrad to 1 mrad and back can be seen, which could not be linked to any other parameter measured in the experiment. The stability of the pointing was roughly constant over the entire duration with a standard deviation of 1.9 mrad. From the symmetry in 2D-pointing-stability data of similar beams shown before, a similar if not lower value of the pointing stability can be assumed in the dispersive axis as well, which was not measured here as explained above. For the divergence, again the mean of 100 shots with the standard deviation as the grey band is shown. The divergence in the horizontal axis was (5.5 ± 0.9) mrad. As the laser polarisation was again parallel to the dispersive axis of the electron spectrometer in this run, the vertical divergence can be assumed to be larger by about a factor of 2.

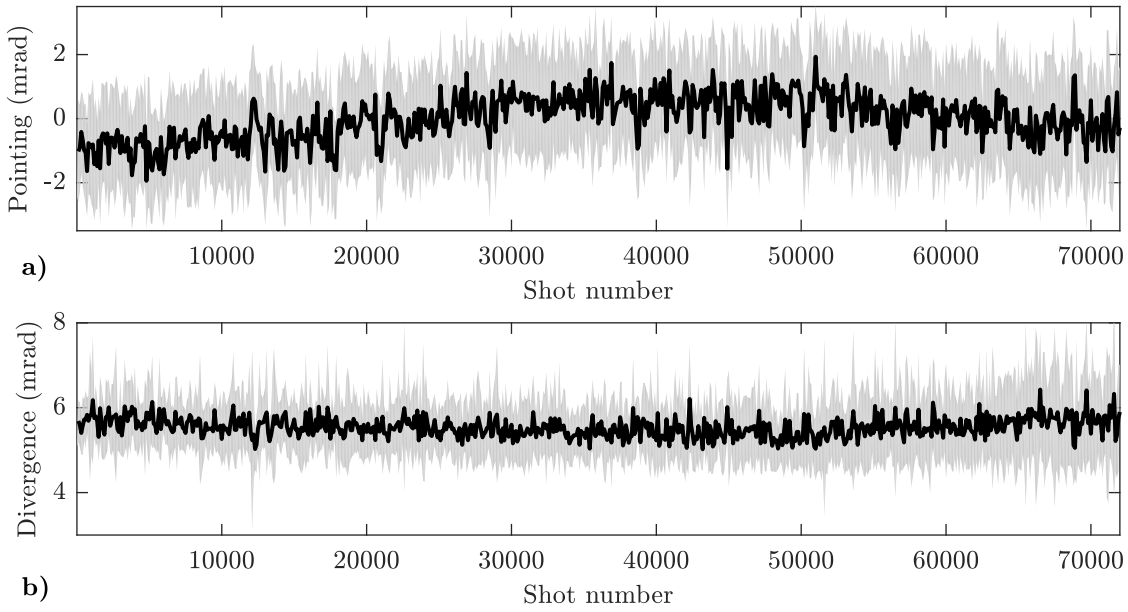

Figure 4.27: a) average pointing (black line) of 100 shots with its standard deviation (grey band) and b) average divergence (black line) of 100 shots with its standard deviation (grey band). Both measurements were done on the electron spectrometer screen in the non-dispersive axis.

The stability of the electron energies is of high importance for many X-ray applications, as the resulting photon energies for planned XFI experiments are mostly dependent on the electron energies. In the presented dataset, a mean peak energy of (63 ± 4) MeV was achieved corresponding to a standard deviation of 6 %. The spectra of these shots are shown in Fig. 4.28a, where each line represents the average spectrum of 100 consecutive shots.

Despite the good reproducibility of the spectrum visible in the waterfall plot, a drift of the peak electron energy over time can be seen in Fig. 4.28a. The effect is more apparent in Fig. 4.28c, where the moving average of 100 shots of the spectral peaks of Gaussian fits is shown together with the moving standard deviation of these fits. A linear fit shows the decrease of the peak energy as the red dashed line. According to the fit, the spectral peak decreases from 65.3 MeV to 60.6 MeV after 72000 shots. This represents a decrease of the spectral peak energy by 7.2 % or 65 eV per shot. Despite the decrease of the energy, the standard deviation of the spectral fluctuation stays around 6 % during the entire run. An explanation for the decrease of the peak energy at constant average charge could be a shift of the laser focus position in the plasma due to heating and deformation of the gratings, leading to a shorter acceleration distance [153, 154]. For the LPA setup in the BOND lab, a test of the heat deposition on the gratings was conducted after the long-duration stability test, which showed a temperature rise of the gratings and a shift of the focus position on similar timescales [155].

In addition to the parameters directly measured in this run and presented above, the

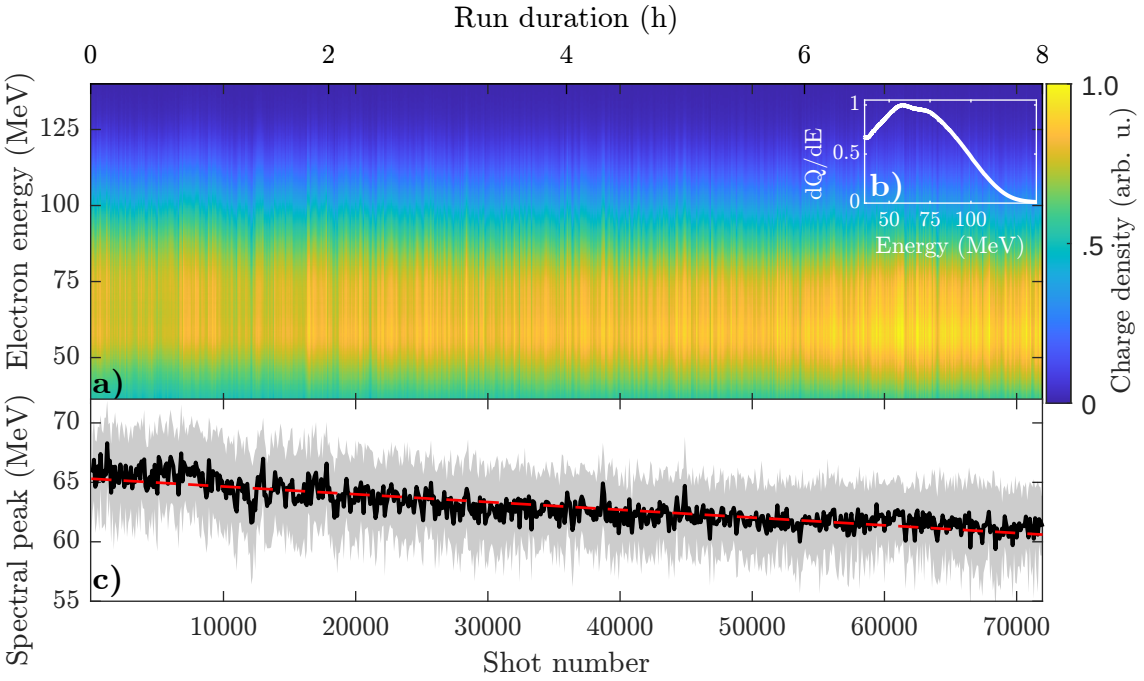

Figure 4.28: Electron energy as function of shot number and time. (a) waterfall plot, (b) average energy spectrum and (c) position of the peaks of Gaussian fits averaged over 100 shots at each position with their standard deviations shown as grey band

high-repetition-rate tests already hint at problems arising from transitioning LPA from few-shot demonstration setups to high-repetition-rate facilities in the future. An example is the amount of data these experiments produce. Saving all available diagnostics of the setup leads to a disk usage of hundreds of gigabyte per hour. Therefore, only a small subset of the available diagnostics was saved during this run in order to minimize the amount of storage required, still resulting in a disk usage of 25 GB/h. These diagnostics were used to correlate the electron charge and energy to the laser energy and plasma density in order to understand the source of variations and improve the stability of the used setup in the future.

Results of these correlations are shown in Fig. 4.29, where a subset of 3600 shots (24 minutes) was investigated to minimize the influence of long-term drifts on the correlations. The highest correlation was found between electron peak energy and electron charge, resulting in a correlation coefficient ρ of 0.72. Consequently, fluctuations of the peak energy are unlikely to arise from beam loading as this would lead to a negative correlation. In addition, a clear correlation between plasma density and charge can be seen in Fig. 4.29b with a correlation of $\rho = 0.50$, showing the importance of the stabilisation of plasma parameters to the percent level and below. An increase of the stability of the plasma density might be achieved by using continuous-flow targets rather than a pulsed gas jet to work in a steady-state regime. The electron charge seems to have a higher dependence on electron density and laser energy (4.29b and 4.29c) compared to the dependence of the electron energy on electron density and laser energy (4.29d and 4.29f), indicating that

the electron energy is mostly dependent on laser parameters such as laser pointing and longitudinal focus position or pulse duration, which were not measured during this run. The weak dependence of the final energy on laser parameters can be explained by the injection technique. The evolution of the mean energy for different laser energies was already depicted in Fig. 4.25. It was shown that a higher (lower) laser intensity also led to stronger (weaker) dephasing of the bunches in the plasma downramp and hence only to a small change of the final energy. The technique is therefore very robust against small changes of the laser energy and its impact on the final electron-bunch energy. The weak dependence of electron density and laser energy shown in Fig. 4.29e can be expected, as full ionisation of the gas can be assumed for the laser intensities in this experiment.

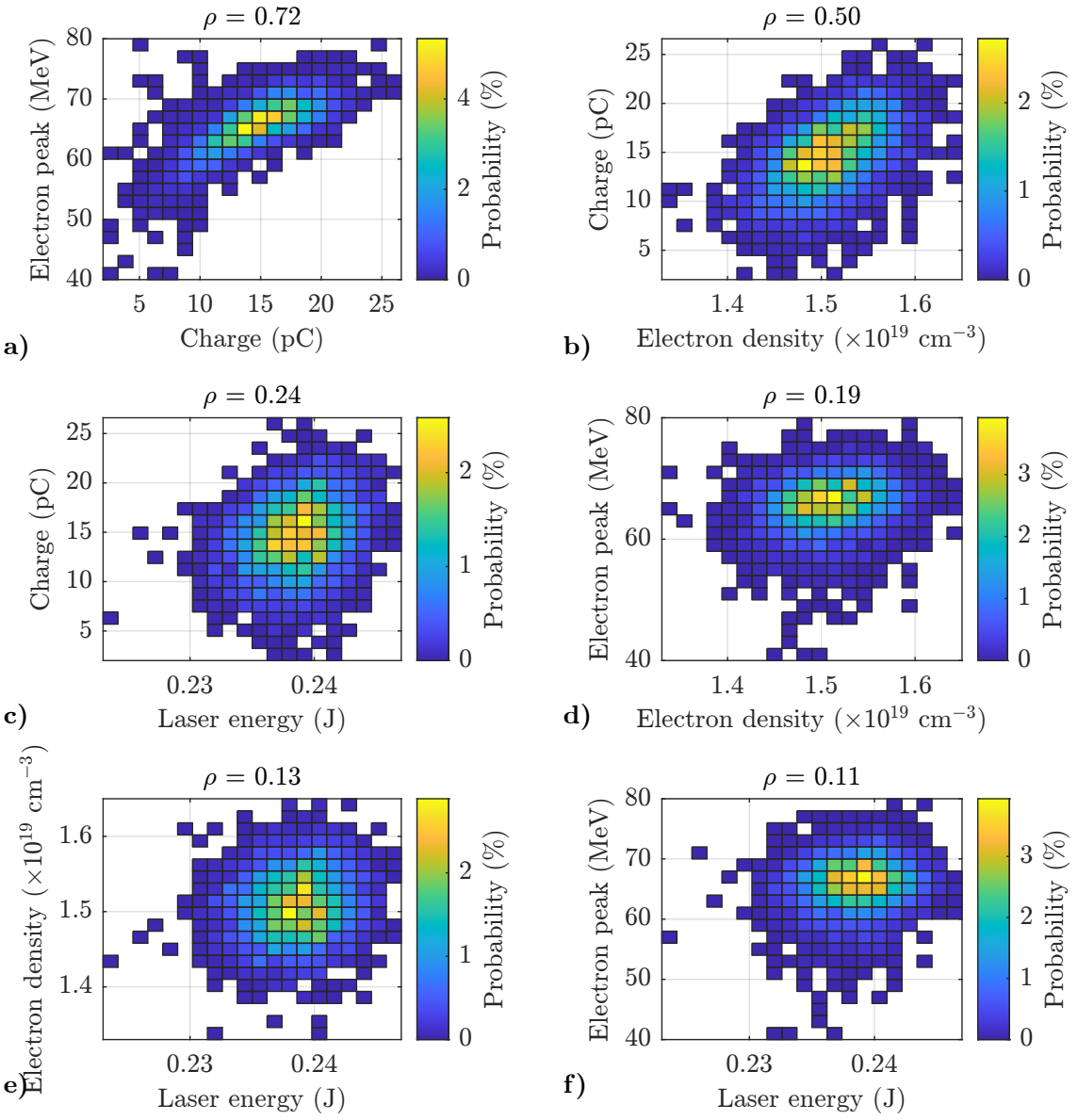

Figure 4.29: Correlations of (a), charge and electron energy; (b), charge and plasma density; (c), charge and laser energy; (d), electron energy and plasma density; (e), electron density and laser energy; (f) laser energy and electron energy.

Furthermore, in this experiment the plasma density seems to have a higher influence on the electron parameters compared to the laser energy in general. It should however be noted that the laser energy refers to the energy and its fluctuations in the near-field of the last amplifier stage (MP2). From this value, the on target energy is calculated, assuming a compressor and beamline transmission of 60%. Consequently, the value stated here is not sensitive to changes of the beamline transmission origination for example from burned optics. The extrapolation of the on-target energy from the energy in the last amplification stage was necessary as the actual on-target energy was not measured during the run. More diagnostics would be required in future if the setup is to be improved. This would allow for a more detailed analysis of the origin of electron-beam fluctuations and their dependence on specific laser and plasma parameters.

4.5 Results of the electron optimisation and future work

The goal of the work described in this chapter was to set up an electron source and optimise it towards the use in tests of XFI experiments using LPA electrons. Self injection, shock-front injection and ionisation injection were tested for their ability to produce beams with stable pointing, spectrum and charge at an energy around 64 MeV, which was required for the planned tests. Using the LPA setup at FLASHForward, ionisation injection offered more stability than the other two injection techniques. This is most likely due to the high fluctuations of the gas backing pressure and consequently the plasma density in the early setup, as this parameter has been shown to influence the stability [55]. After the comparison, the ionisation-injection beams were further optimised by employing a self-truncated ionisation injection regime with moderate laser intensities, suitable for the planned Thomson experiments. The development of a differential pumping cube led to an increase of the repetition rate of the system by almost two orders of magnitude. A change of the gas system enabled stabilisation of the plasma density to the percent level. The spectral bandwidth, overall stability and repetition rate of these electron beams was sufficient to successfully conduct the planned XFI tests [7] and the development of an in-situ diagnostic using Thomson scattering which will be described in the next chapter.

In addition, a long-term stability test of the produced electron beams was performed over a duration of 8 hours. The 72000 consecutive shots in this test surpassed previous stability studies at this energy regime, where the stable generation of consecutive [55, 156–158] electron shots was reported and is only comparable to recent studies also conducted at DESY [4]. The study improved the understanding of the fluctuations of the produced electron beams and showed strong correlations between the plasma density and the final electron parameters. Furthermore, a drift of the final electron energy was measured, most likely originating from heat deposition of the laser pulse onto the compressor gratings and a subsequent deformation of the gratings. As no far-field information was saved during

this run this effect was not directly measured, but measurements of the heat deposition conducted afterwards showed a deformation on similar timescales [155].

To improve the electron beams further, several optimisations are possible. The development of a continuous-flow target could increase the beam stability even further, as the plasma density has been shown to have a large impact on the produced beams. To increase the number of electrons around the desired energy of 64 MeV, the injection mechanism could be further optimised e.g. by the implementation of shock-front assisted ionisation injection which has been shown to produce narrow bandwidth electron beams [57] or further tests of shock-front injection with the improved gas system and additional controls to tune the shock front, such as rotations of the blade. The development of continuous-flow targets could again be beneficial in these cases to decrease fluctuations experienced in previous tests potentially arising from density changes. Furthermore, a new grating was installed that shows less temperature dependent deformation and enabled the focal spot quality to be maintained even when firing at the maximum repetition rate of 10 Hz [155]. It is expected that this will help to operate the setup at a constant energy at high repetition rates for several hours.

The decrease of the peak energy by less than 1% per hour shows that thousands of shots taken over several hours are required to determine the stability of LPA for future applications as such slow and minor drifts require need to investigated over long timescales and with high statistical significance. Furthermore, work regarding data storage and live analysis needs to be done in order to operate LPA experiments at high repetition rates over several hours on a daily basis while maintaining an economic disk usage. Camera images could for example be immediately analysed to store information such as centroids, total counts or beam widths rater than entire camera images. TThe experiments described here are an ideal starting point as they were performed in a regime with similar parameters expected from the first generation of high-power kHz laser systems such as KALDERA [159] and optimised for the medical application XFI.

Chapter 5

Measurement of electron parameters using Thomson scattering

The non-invasive measurement of electron beam parameters is crucial for many experiments or applications of plasma acceleration. An example is the measurement of the electron energy. In staging experiments [160] the energy after the first stage needs to be known in order to determine the energy gain of following stages. Also in the case of medical applications based on Thomson scattering, such as X-ray fluorescence imaging (XFI) [5, 6, 25], the electron energy needs to be known. Thomson scattering is the interaction of a photon with an electron, where in the rest frame of the electron, the photon energy is much smaller than the electron rest mass. In this case, the electron recoil can be neglected and the interaction can be viewed as an energy transfer from the electron to the photon resulting in an X-ray. The electron energy therefore defines the energy of a resulting Thomson X-ray and thus is a critical parameter for potential medical treatment. An obvious technique for a non-invasive measure of the electron energy is therefore to measure the energy of Thomson X-rays to determine the initial electron energy.

The use of Thomson scattering as a diagnostic to determine the energy of LPA electron beams has been proposed multiple times [26, 161–164], but was only demonstrated using conventional accelerators [10, 165]. In the case of LPA beams, the general concept was applied to the data of tunable Thomson sources [166, 167] in an overview of diagnostic methods for plasma accelerators [26], which is depicted in Fig. 5.1. In this example, the quadratic relation between electron energy and resulting Thomson energies can be seen for the two cases, but a relative shift between the two experiments is visible due to different experimental conditions such as the a_0 and the electron divergence in the interaction. This example shows that a detailed understanding of the process and the detectors is necessary for a precise measurement, as will also be explained in the following. The Thomson beam can also be used to determine other electron parameters such as divergence [162, 163] or emittance [12]; only the latter has been measured using electrons from a plasma accelerator.

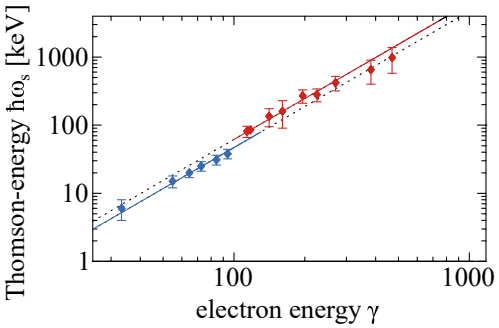

Figure 5.1: Image taken from [26] and modified. Shown is the quadratic relation between the electron gamma factor and the resulting Thomson energies in the interaction. The data shown here is taken from demonstrations of tunable Thomson sources by Khrennikov *et al.* ([166], blue) and Powers *et al.* ([167], red). The dotted lines are extrapolations of the fitted areas (solid lines) for an easier comparison.

However, the use of Thomson scattering to measure the electron energy has some drawbacks, explaining why it is not commonly used in accelerator physics. The measurement of electrically neutral X-rays is much more complicated than that of electrons. This is especially true for X- and γ-ray energies of tens of keV and above as will be shown later. In addition, broadening effects complicate the measurement of electron parameters from a Thomson beam.

While there are some difficulties in the Thomson experiments, they offer the advantage that the interaction process and the measurement can be decoupled due to the low interaction-probability of X- and γ-rays with matter. It is therefore possible to transport a Thomson beam containing information about the electron beam for several meters through vacuum or gases before detecting it to extract information about the electrons. This opens up the possibility to interact the Thomson beam inside the plasma [161] and gather information on the electron bunch during its acceleration. This information can help to study issues such as dephasing or emittance growth in more detail and help to further improve the quality of electrons accelerated in plasmas. So far, information such as injection position [168] or dephasing length [52, 169] could only be acquired by changing the injection position or the plasma length at the cost of also changing the final state of the electrons. Other proposed techniques to get information about the electron-bunch properties during acceleration in a non-invasive measurement such as streaked betatron radiation require transverse density gradients [170], which makes the experimental realisation complicated and could lead to potential conflicts with other restrictions to the setup.

In this chapter, the first measurement of electron properties during acceleration is presented. Thomson scattering was used as a non-invasive tool to measure the energy evolution of the electron beam inside the wakefield. The chapter starts with an introduction of the theory of Thomson scattering with laser plasma electrons in Sec. 5.1. Afterwards, the experimental setup is described in Sec. 5.2. To break down the complexity of the experiment, aspects of detection of the Thomson X-rays and the alignment

process are described in separately in Sec. 5.3, and Sec. 5.4. The measurement of the electron energy using Thomson scattering is described in Sec. 5.5. This principle is then expanded to the measurement of the energy evolution of the electrons in the plasma in Sec. 5.6. Finally, the experimental results are compared to the results obtained from Particle-In-Cell simulations in Sec. 5.7, where the power of the method is shown in an investigation of dephasing for the accelerated electron beams. Results of the measurement described in this chapter are also prepared for a separate publication [147].

5.1 Thomson scattering

As described before, Thomson scattering (TS) is the interaction of a photon with an electron, where energy is transferred from the electron to the photon. In case of relativistic electrons, the energy of the photon after the process is usually in the X- or γ-ray regime and, due to momentum conservation, is moved into the direction of the electron. Thomson scattering describes the low-energy limit of inverse Compton scattering and therefore neglects the recoil of the electron in the process. For the parameters studied in this work, this electron recoil is negligible, which is why the term Thomson scattering will be used throughout this thesis.

In this section, basic principles of TS will be discussed, often with respect to the use of TS in the context of plasma acceleration. First, the final energy of a single photon scattering with a single electron is derived in Sec. 5.1.1. Afterwards, effects from the scattering process of electron bunches with laser pulses are described in Sec. 5.1.2. The results of this section are based on work done previously, where the use of TS as a diagnostic for plasma based accelerators was studied using simulations [33].

5.1.1 Scattering of a single electron and a single photon

To start with, the energy gain of a single photon scattering with a single electron is derived [163, 171]. The scattering of electron and photon is considered to be in an arbitrary coordinate system. The electron can be described by a four momentum vector $q_i = \gamma m(c, v_i)$, where γ is the electron's relativistic gamma factor defined as $\gamma = \sqrt{1-(v/c)^2}$, c is the speed of light, m is the rest mass of the electron, and v_i the velocity components of the incoming electron. Similarly, the incoming photon with initial energy E_i moving in the direction $\hat{n}_i$ can be described by a four-momentum vector $p_i = E_i/c(1, \hat{n}_i)$. The same representation can also be chosen for the electron and the photon after the scattering process, defined as $q_s = \gamma m(c, v_s)$ and $p_s = E_s/c(1, \hat{n}_s)$. The process is depicted in Fig. 5.2.

For the calculation of the energy of the final-state photon, obviously the conservation of energy and momenta before and after the scattering as in the depicted case can be assumed:

$$q_i + p_i = q_s + p_s. \tag{5.1}$$

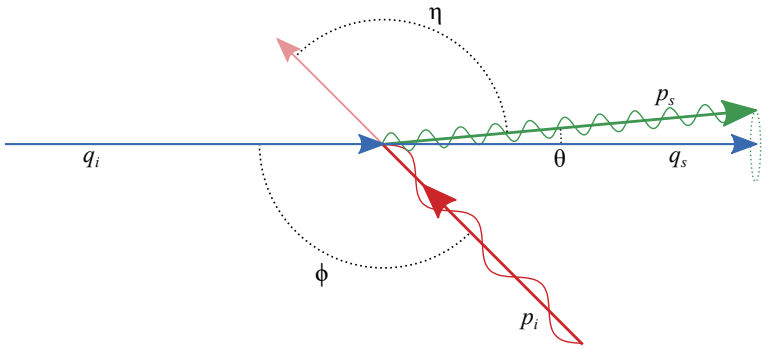

Figure 5.2: Geometry of the scatter process of electron and photon in TS. Shown is the scattering of an incident electron q_i with an incident photon p_i under a angle ϕ resulting in a highly energetic scattered photon with an opening angle θ, relative to the incident electron path. Electron and photon after the interaction are defined as q_s and p_s, respectively. In addition, the angle between incident and scattered photon η is shown.

In addition, the Lorentz invariants for electrons and photons defined in Eqs. 5.2 and 5.3 are used to simplify further calculations

$$\begin{aligned} q_\mu q^\mu &= \gamma^2 m^2 (v^2 - c^2) = m^2 \frac{v^2 - c^2}{1 - v^2/c^2} = -m^2 c^2, \\ p_\mu p^\mu &= 0, \end{aligned} \tag{5.2}$$

$$\begin{aligned} (p_i + q_i)_\mu (p_i + q_i)^\mu &= (p_s + q_s)_\mu (p_s + q_s)^\mu, \\ 2{p_i}_\mu {q_i}^\mu - m^2 c^2 &= 2{p_s}_\mu {q_s}^\mu - m^2 c^2, \\ p_i q_i &= p_s q_s. \end{aligned} \tag{5.3}$$

The combination of the conservation of energy and momenta in Eq. 5.1 with the invariants from Eq. 5.2 and Eq. 5.3 leads to

$$p_i p_s + p_s q_s = p_i q_i. \tag{5.4}$$

Here, the four-momenta for the electron and photon stated earlier can be inserted

$$\frac{E_i}{c}\frac{E_s}{c}(\hat{n}_i \hat{n}_s - 1) + \frac{E_s}{c}\gamma m(\hat{n}_s v_i - c) = \frac{E_i}{c}\gamma m(\hat{n}_i v_i - c). \tag{5.5}$$

For the simplification of Eq. 5.5, the occurring scalar products will be presented as angles according to Fig. 5.2. The scattering angle, which is the angle between the incident photon and the incident electron can be described as $\hat{n}_i v_i = v_i \cos\phi$. The angle between incident electron and scattered photon is defined as $\hat{n}_s v_i = v_i \cos\theta$, while the angle between the incident photon and scattered photon is $\hat{n}_i \hat{n}_s = \cos\eta$. Inserting these angles into Eq. 5.5

leads to

$$\frac{E_i}{c}\frac{E_s}{c}(\cos\eta - 1) + \frac{E_s}{c}\gamma m(v_i\ \cos\theta - c) = \frac{E_i}{c}\gamma m(v_i\ \cos\phi - c). \tag{5.6}$$

Introducing the dimensionless velocity of the incoming electron $\beta = v_i/c$, simplifies this equation to

$$\frac{E_i}{c^2}E_s(\cos\eta - 1) + E_s\gamma m(\beta\ \cos\theta - 1) = E_i\gamma m(\beta\ \cos\phi - 1). \tag{5.7}$$

Rearranging this equation leads to an expression for the energy of the scattered photon E_s:

$$E_s = \frac{E_i(1 - \beta\ \cos\phi)}{\frac{E_i}{\gamma mc^2}(1 - \cos\eta) + 1 - \beta\ \cos\theta}. \tag{5.8}$$

This equation can be further simplified when considering the electron from a plasma accelerator and the geometry of the planned experiments. For a relativistic electron and an incoming photon with a wavelength of 800 nm (1.5 eV), the first term in the denominator is very small. The term reaches its maximum for head on scattering of electron and photon, which is also a close approximation of to the geometry in the experimental setup. Using this maximum as a further approximation, η can be substituted by $\pi - \theta$ and a Taylor expansion of the cosine leads to:

$$\cos\eta = \cos(\pi - \theta) = -\cos\theta = -1 + \frac{\theta^2}{2} - (...). \tag{5.9}$$

Inserting this into into Eq. 5.8 leads to

$$\begin{aligned} E_s &= \frac{E_i(1 - \beta\ \cos\phi)}{\frac{E_i}{\gamma mc^2}(1 + 1 - \frac{\theta^2}{2}) + 1 - \beta\ + \beta\frac{\theta^2}{2}} \\ &= \frac{E_i(1 - \beta\ \cos\phi)}{1 - \beta\ + \beta\frac{\theta^2}{2} + 2\frac{E_i}{\gamma mc^2} - \frac{E_i}{\gamma mc^2}\frac{\theta^2}{2}}. \end{aligned} \tag{5.10}$$

Applying the approximation $1/\gamma^2 \approx 2 - 2\beta$, that is valid in the ultra relativistic limit, Eq. 5.10 can be simplified to

$$\begin{aligned} E_s &= \frac{E_i(1-\beta\ \cos\phi)}{\frac{1}{2\gamma^2} + \beta\frac{\theta^2}{2} + 2\frac{E_i}{\gamma mc^2} - \frac{E_i}{\gamma mc^2}\frac{\theta^2}{2}} \\ &= \frac{2\gamma^2 E_i(1-\beta\ \cos\phi)}{1 + \beta\theta^2\gamma^2 + 4\frac{E_i\gamma^2}{\gamma mc^2} - \frac{E_i\gamma^2}{\gamma mc^2}\theta^2} \\ &= \frac{2\gamma^2 E_i(1-\beta\ \cos\phi)}{1 + \theta^2\gamma^2(\underbrace{\beta - \frac{E_i}{\gamma mc^2}}_{\approx 1}) + 4\gamma\frac{E_i}{mc^2}}. \end{aligned} \tag{5.11}$$

Using the last approximation, the energy of the photon in the finial state from the scattering of a single electron with a single photon simplifies to

$$E_s = \frac{2\gamma^2 E_i(1-\beta\ \cos\phi)}{1 + \theta^2\gamma^2 + 4\gamma\frac{E_i}{mc^2}}, \tag{5.12}$$

for the case of inverse Compton scattering. For $\gamma \ll \frac{E_i}{4mc^2}$, which for an incoming laser of 800 nm implies $\gamma \ll 1.4 \times 10^6$, the last term in the denominator can be neglected, leading to an energy of the scattered photon of

$$E_s = \frac{2\gamma^2 E_i(1-\beta\ \cos\phi)}{1 + \theta^2\gamma^2}. \tag{5.13}$$

As the electron beams described in Chapter 4 are far from reaching the gamma values stated here, the process will be considered as Thomson scattering and the recoil of the electron will be neglected in further calculations. The energy of the scattered photon obviously reaches its maximum for $\phi = \pi$ (head-on scattering) and $\theta = 0$ (scattering in the direction of the electron) and the energy of the produced photon can be given by

$$E_{s,max} = 4\gamma^2 E_i. \tag{5.14}$$

The maximum energy of Thomson photons calculated using Eq. 5.14 for electron energies between 1 MeV to 100 MeV is depicted in Fig. 5.3

The minimum energy (for a given scattering geometry) is half of the maximum energy, when the opening angle of the radiation is $1/\gamma$. As in the case of synchrotron radiation, the necessity for an opening angle of $1/\gamma$ becomes immediately clear when considering the Thomson interaction in the rest frame of the electron and then Lorentz transfer the radiation back into the laboratory frame.

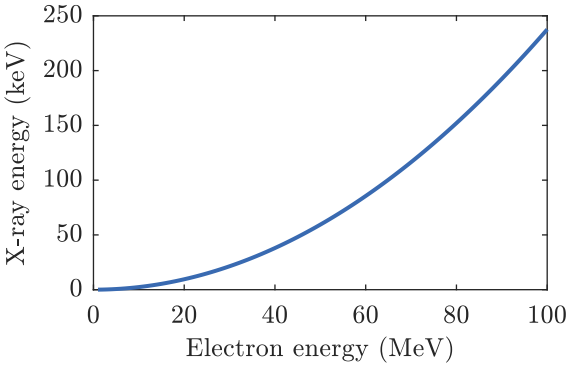

Figure 5.3: Maximum energy of TS photons after scattering of electrons with an energy from 1 MeV to 100 MeV head on with 800 nm photons.

5.1.2 Scattering of an electron bunch with a laser beam

After deriving expected energies for the scattering process of a single electron with a single photon, several effects are discussed that need to be taken into account when looking at the Thomson spectrum from the interaction of an electron bunch with a laser beam. First of all, the effect of the laser is discussed. Thereby, only the linear case, that is an $a_0 < 1$ is discussed here. For the effects of the laser beam in a non-linear case, please refer to additional literature [149, 172].

The high-intensity electrical fields of a laser pulse lead to transverse oscillations, as was already described in Chapter 2. These oscillations reduce the longitudinal velocity of the electrons, thereby reducing its γ-factor in the interaction. The reduced γ-factor can be defined as [173]

$$\gamma^* = \frac{\gamma}{\sqrt{1 + \frac{{a_0}^2}{2}}}, \tag{5.15}$$

Inserting this factor into Eq. 5.13 leads to

$$\begin{aligned} E_s &\approx \frac{2\gamma^{*2} E_i (1 - \beta \ \cos\phi)}{1 + \theta^2 \gamma^{*2}} \\ &= \frac{2\gamma^2 E_i (1 - \beta \ \cos\phi)}{(1 + \frac{a_0^2}{2})(1 + \frac{\theta^2\gamma^2}{1 + a_0^2/2})} \end{aligned} \tag{5.16}$$

which can be simplified to the well known formula for the energy of a scattered photon in Thomson scattering:

$$E_s = \frac{2\gamma^2 E_i (1 - \beta \ \cos\phi)}{1 + \frac{a_0^2}{2} + \theta^2\gamma^2}. \tag{5.17}$$

The use of an ultrashort laser pulse also introduces some broadening of the resulting Thomson spectrum [33, 162, 164, 172], as can be seen from Eq. 5.17. When the two beams pass each other, the electrons interact with regions of the pulse with different intensities. The resulting Thomson spectrum will therefore be broadened, even for a

theoretical scattering on monochromatic electrons. In addition, pulses on the order of tens of femtoseconds and below require large bandwidths, as was described in Sec. 3.1.1. The resulting Thomson spectrum will therefore also be broadened by the same amount as the incoming laser, in this case almost 10%. Another broadening effect due to the laser arises from the focussing geometry. Focussing of the laser leads to differences in the scattering angle ϕ for different photons in the interaction, introducing further broadening. However, this effect is small compared to the other effects described here and can be neglected [172].

More broadening effects arise when considering the scattering with electron bunches rather than single particles. The introduction of an energy spread of the electron bunch obviously leads to a broadening effect. Compared to broadening due to the laser bandwidth, this is more significant due to the quadratic factor of the electron energy in the Thomson formula and twice as big as the broadening from the laser bandwidth [172]. Another broadening effect from the electron bunch comes from the electron-beam divergence. Here, it is important to consider an actual measurement of the Thomson photons using a detector, as becomes clear when looking again at the equation for the electron energy in Eqs. 5.17 and 5.13. In contrast to bandwidth from the laser and electron beam, the divergence has no direct effect on the final photon energy apart from small changes of the scattering angle ϕ for electron with different divergences. This effect is similar to the laser focussing and can be neglected and the total Thomson spectrum does not significantly change for electron beams with different divergences. However, an electron with a pointing angle of θ compared to the main electron axis can still emit a photon onto the main axis with its energy reduced by a factor of $1/(1+\theta^2\gamma^2)$. Therefore, a detector measuring only a small cone with respect to the opening angle of the total Thomson beam, as is done in many actual measurements or applications, will detect photons emitted under different opening angles. In the case of electrons from a LPA, the broadening due to electron-energy spread and electron beam-divergence are often the dominant factors for the broadening of the measured TS source. The different contributions leading to broadening of the spectrum can be combined leading an estimation of the relative bandwidth defined as the fraction of the bandwidth of the source $\Delta\omega_{TS}$ and its mean energy ω_{TS} and estimated by [33, 162, 172]

$$\frac{\Delta\omega_{TS}}{\omega_{TS}} \approx \sqrt{\frac{\gamma_e^4\sigma_e^4}{16} + 4\frac{\Delta\gamma_e^2}{\overline{\gamma_e^2}} + \frac{\Delta\omega_{Laser}^2}{\omega_{Laser}^2} + \frac{a_0^4}{4}}. \tag{5.18}$$

In addition to broadening effects, the electron divergence and the intensity of the scattering laser also decrease the peak energy and the mean energy compared to values expected from Eq. 5.14. This effect was studied in detail using a linear accelerator, which allowed a stable electron beam to be used and permitted control over the electron-beam divergence [162]. In these experiments, the divergence was varied by changing the final focussing of the electron beam and thereby the divergence of the electrons overlapping

with the laser pulse. Results of this study are shown in Fig. 5.4.

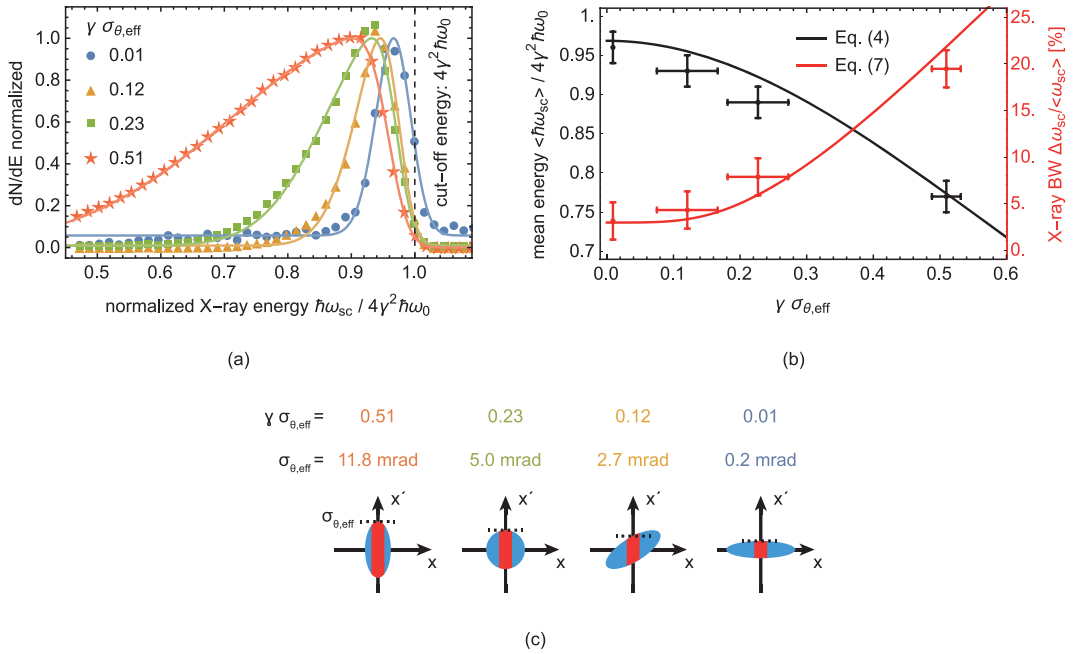

Figure 5.4: Image taken from [162]: Influence of the electron beam divergence on the Thomson spectrum. a) shift of the peak energy with respect to the expected maximum energy calculated using Eq. 5.14 for four different cases of the dimensionless parameter $\gamma\sigma_{\theta,eff}$. b) shift of the mean energy as function of the dimensionless parameter $\gamma\sigma_{\theta,eff}$ and influence on the bandwidth. c) overlap of electron beam and laser beam for different cases of the final focusing.

In the experiment, the results are then generalised by looking at the influence of the product of electron energy (γ-factor) and divergence (σ) for a laser intensity of $a_0 = 0.25$. For this, only the part of the bunch that is interacting with the laser is considered (see Fig. 5.4c). The divergence of this part is then defined as effective divergence (σ_{eff}). A deviation of the peak and the mean energy with respect to the maximum on-axis energy is shown in Fig. 5.4a and Fig. 5.4b respectively. When using Thomson scattering as a diagnostic for the electron energy, one has to consider the difference of the Thomson peak energy compared to the calculated cut-off energy defined in Eq. 5.14. This can be achieved by including the shift of the peak of the Thomson spectrum originating from the electron divergence as is shown in Fig. 5.4. To overcome this issue, the peak of the Thomson spectrum can therefore be determined by including a correction factor K, which is defined by the effective divergence of the electron beam in the interaction. The peak of the Thomson scattering spectrum is then given by including this factor in Eq. 5.17, resulting in:

$$E_{s,peak} = K \cdot \frac{2\gamma^2 E_i(1 - \beta\ \cos\phi)}{1 + \frac{a_0^2}{2} + \theta^2\gamma^2}. \tag{5.19}$$

From the correlation of the photon energy and the γ-factor in Eq. 5.19, it becomes clear that an on-axis measurement of the electron energy is possible using Thomson scattering

by rearranging the equation to

$$\gamma_{peak} = \sqrt{\frac{E_{s,peak}}{K \frac{2\ E_i\ (1-\cos\ \theta)}{1+a_0^2/2}}}. \tag{5.20}$$

Afterwards, the electron energy can be calculated via $E_e = (\gamma - 1) \cdot m_e c^2$, where $m_e c^2$ is the electron energy at rest.

5.2 Experimental setup

The experiments to measure the energy evolution of the electron beam inside the wakefield required a complicated layout inside the chamber with several possibilities to adjust the beam path, multiple diagnostics and full control of the optics to enable the precise alignment of three laser beams on the level of micrometers in space and femtoseconds in time, stretching the capapilities of the wakefield chamber to its limits. A detailed sketch of the most important optics and diagnostics for the experiment is shown in Fig. 5.5.

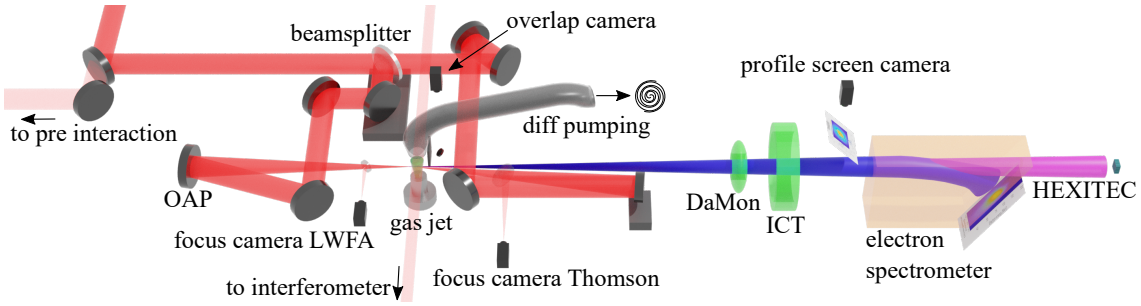

Figure 5.5: Schematic drawing of the setup for the Thomson experiments. The beam enters the main vacuum chamber and the leakage of the first mirror was sent to the pre-interaction diagnostics for alignment. After the first mirror, the beam splits into LPA and Thomson part. The reflected part was sent to a 3" f/11 off-axis parabola (OAP), which focusses the beam onto the gas jet to accelerate electrons. The remaining part of the laser was focussed using a spherical mirror that is positioned on a linear stage. The beam path of the LPA laser could be adjusted using a second linear stage on which the beamsplitter and a mirror were positioned. To check the focus quality of the two beams, wedges could be driven into the focussed laser beams, sending it into focal-spot cameras. A probe beam was used for plasma-density measurements and timing of the two laser arms. To characterise the electron beams, the DaMon, an ICT, a profile screen and an electron spectrometer were available. The Thomson beam was measured using the HEXITEC or with a phosphor screen imaged with a camera.

The beam entered the chamber and the leakage of the first mirror was sent to the pre-interaction diagnostics table for alignment of the laser beam into the chamber. The reflected part was split using a 5 mm thick MgF beamsplitter, resulting in 2/3 of the laser power being in the LPA laser arm and 1/3 of the energy in the Thomson arm. To enable the femtosecond alignment of these two arms, a delay stage was installed in the LPA laser arm, consisting of the beamsplitter and an additional mirror. A similar delay stage was

implemented outside the chamber in the beamline of the perpendicular probe beam, to enable femtosecond adjustment of the three laser beams for the relative timing of LPA and Thomson laser arms. The LPA laser beam was focussed onto the gas jet using the 500 mm f/11 off-axis parabola (OAP) with an angle of 21 degrees and dielectric coating. As no parabola with an angle of incidence required for these experiments was available, the Thomson laser arm was focused using a spherical mirror with the same focal length. The angle of incidence of about 8 degrees onto the spherical mirror led to an astigmatic focus of the Thomson arm, reducing the peak intensity in the interaction to $a_0 = 0.3$. To change the focal plane and thereby the interaction position of the Thomson laser, the spherical mirror was placed on a stage with its axis of movement parallel to the electron axis. The focus quality of both laser arms could be measured using beam samplers that could be put into the beam, sending the beam into cameras that were installed in the vacuum chamber. A third camera imaged a screen which enabled the spatial overlap of the two laser arms at a desired overlap plane. A camera placed outside the chamber supported this alignment by imaging of the plasma from the top.

Additional mirrors not shown in the schematic could be put into the beam before the two focussing optics, sending the beam through a 1 mm window into the Wizzler for pulse-duration measurements of both LPA and Thomson laser independently. To have full control over the laser beam, the OAP, spherical mirror and the two mirrors before the focussing optics were controllable in the vertical and horizontal plane using pico motors. In addition, each laser arm could be blocked independently, which was required for alignment. An image of full setup in the LPA chamber can be seen in Fig. 5.6.

As was the case before, the electrons were diagnosed in the vacuum beamline after the interaction chamber. Diagnostics available were again DaMon and ICT for charge measurements, a profile screen that could be driven in for measurements of electron beam divergence and pointing and the magnet spectrometer to measure the electron beam energy. In addition, the magnet enabled the separation of electron and Thomson beam. The Thomson beam was then sent through a 200 µm thick aluminium window and was diagnosed using either a DRZ screen imaged with an EMCCD camera or the HEXITEC detector. As this detector was the major diagnostic for the Thomson beam, it is described in more detail in the next section.

5.3 The HEXITEC detector

The main parameter of the Thomson beam required for the determination of the electron energy is the spectrum of the produced X-ray beam. According to Fig. 5.3, X-ray energies of up to 100 keV can be expected for the electron beams described in Chapter 4. To measure the energy of such a Thomson beam, the choice fell on the HEXITEC (**H**igh **E**nergy **X**-ray **I**maging **Tec**hnology) detector [174, 175]. The HEXITEC detector is a pixelated cadmium-telluride detector for energy measurements of X-rays with energies

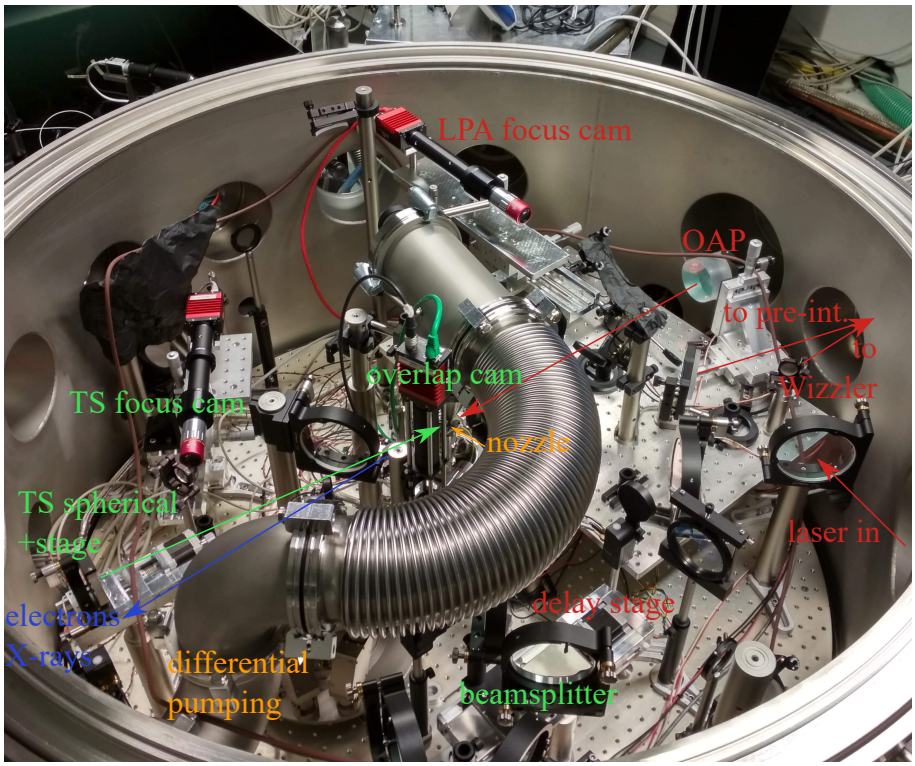

Figure 5.6: Image of the setup in the wakefield chamber for the Thomson experiments.

of 4 keV to 200 keV. While the HEXITEC allows a direct measurement of the photon energies via single photon counting, a detailed understanding of the physics processes involved in the measurement and detector effects arising from those is necessary for a precise assessment of the X-ray spectrum. The detector and its working principle are therefore described in this section in more detail.

To begin with, the attenuation of X-rays is discussed in Sec. 5.3.1 to understand the processes in the detector in more detail. Afterwards, the detector is described in detail and important characteristics of the detection in case of the HEXITEC are explained in Sec. 5.3.2, including a description of calibration experiments performed using radioactive sources. Finally, simulations of the detector using Geant4, which were performed to estimate effects of the detector and the attenuation of the beamline on the measured spectrum are described in Sec. 5.3.3.

5.3.1 Measurement of X-rays

The detection of X-rays has three main challenges. The first problem is that X-rays can pass matter without interaction as they are not charged. Therefore, properties of an X-ray beam are not measured simultaneously (as for example is the case with the measurement of electron-charge or profile using the techniques described above), but instead individual photons are removed from the X-ray beam by statistical events. While this property explains the medical utility immediately after the discovery of X-rays by Röntgen in 1895

[14], it complicates a precise measurement of the energy of all particles in a beam and leads to the second problem: the X-rays themselves are not detected directly, but rather secondary particles created from them. To correctly measure the energy of an X-ray, it is therefore required to measure all secondary particles and, in the case of an X-ray beam consisting of multiple photons, to correctly assign the energy of the secondaries to their source. Lastly, the secondary particles are produced by three processes, namely photoelectric absorption, Compton scattering and pair production, with different cross sections depending on the material of interaction and the energy of the incoming radiation. To understand issues in the detection process, these processes are described here together with the working principle of (pixelated) semiconductor detectors such as the HEXITEC. This section is again based on previous work [33].

Photoelectric absorption

In photoelectric absorption, the X-ray is absorbed by an electron of the absorber material [176–179]. The electron then leaves the atom with a kinetic energy equal to the difference of the energy of the incoming X-ray and the binding energy of the electron. Due to momentum conservation, absorption of inner shell electrons is more likely to happen. The vacancy in such an inner shell is then filled by an outer-shell electron, resulting in the emission of fluorescent radiation or more electrons. Photoelectric absorption is the dominant process, especially in high-Z materials for the X-ray energies in these experiments. Its principle is depicted in Fig. 5.7

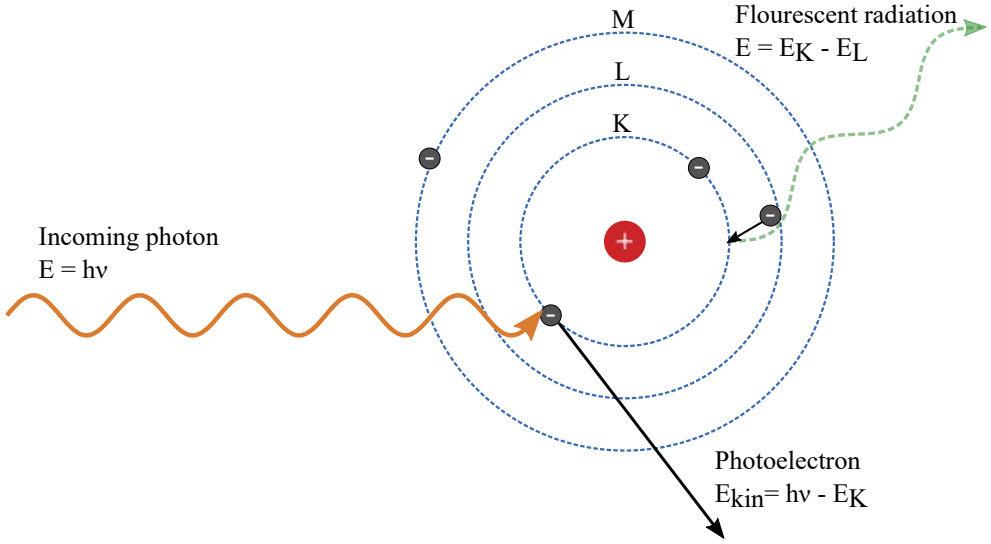

Figure 5.7: Illustration of the photoelectric effect. An incoming photon with an energy of $E = h\nu$ is absorbed by an electron of an inner shell. This leaves the atom with a kinetic energy of the inital photon minus the binding energy $E_{kin} = h\nu - E_{bind}$. The missing inner shell electron is filled by an electron from an outer shell. The energy gained in this process is either emitted by fluorescent radiation or by the emission of further electrons.

Compton scattering

In Compton scattering, the photon scatters on a quasi-free electron in the absorber material and transfers a part of its energy to the electron [178, 179] as depicted in Fig. 5.8. As the energy of the incoming photon is usually higher than in the case of photoelectric absorption, the binding energy of the electron can be neglected and the process is often considered as elastic scattering between a free electron and the photon. In the case of the HEXITEC, the cross section can be neglected for energies below 50 keV and only becomes the dominant process for energies above 250 keV. For the measurement of the Thomson spectrum, it is therefore less important than the photoelectric absorption described above, while still being significant. Furthermore, Compton scattering contributes to detected background, as the energy of the photon after the scattering process is usually still high, allowing it to leave the detector without detection. In such a case, only the energy of the electron after the scattering process would be detected, leading to an incomplete measurement of the X-ray energy.

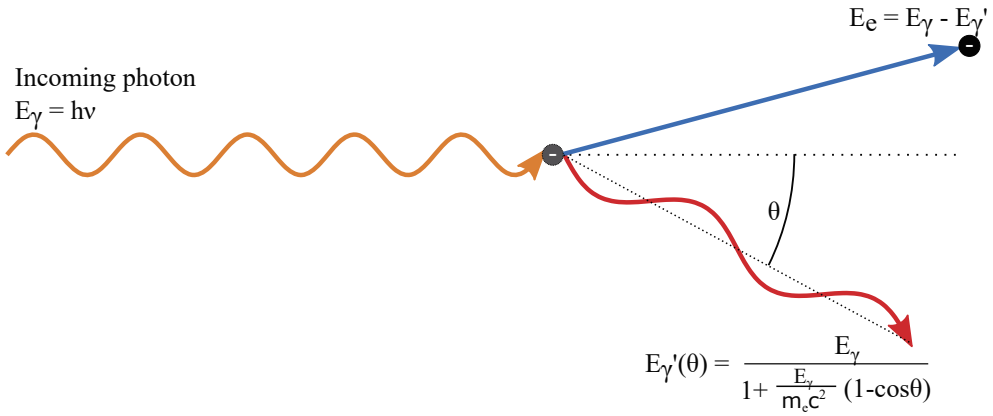

Figure 5.8: Illustration of Compton scattering. An incoming photon with an energy of $E_\gamma = h\nu$ scatters on a quasi free electron from the absorber material, whereby the electron gains part of the energy of the incoming photon.

Pair production

In the case of pair production, the photon converts into an electron-positron pair in the electric field of a nucleus. In stronger fields, the process is more likely to happen, explaining its higher cross sections for high-Z materials. The produced positron will annihilate in the presence of matter, resulting in the production of two photons with an energy of 511 keV. Due to energy conservation, pair production can only occur for initial photon energies of 1022 keV and above. It is therefore not of interest for the measurement of Thomson X-ray beam in this case. Nonetheless, this process needs to be considered for the experiments as bremsstrahlung present in the experiments does lead to a significant background, especially as the relatively high energy of the secondaries makes effective shielding challenging.

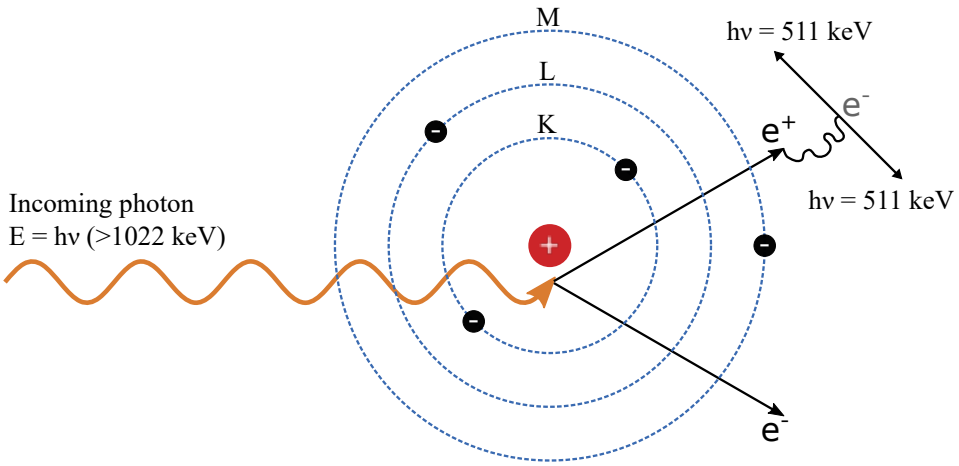

Figure 5.9: Illustration of pair production. An incoming photon with an energy of $E = h\nu >$ 1.022 MeV converts in the electric field of a nucleus of the absorber material into an electron and a positron, transferring all its energy to these particles. The positron then further annihilates with another electron into two 0.511 MeV photons.

Semiconductor detectors

To measure the energy of the secondary particles created in a detector, usually semiconductor detectors are used. The peculiarity of semiconductors is in their configuration of conduction and valance bands as depicted in Fig. 5.10. In semiconductors, there is a small gap between the conduction band and the valence band, allowing electrons to overcome the band gap if they gain energy by thermal excitation. In conductors, there is no gap between the two bands, meaning charge can move freely, while in insulators, the band gap is too high to allow electrons to transition from the valance band to the conduction band [180–182]. This band configuration also explains why in contrast to conductors, the conductivity of semiconductors increases with temperature.

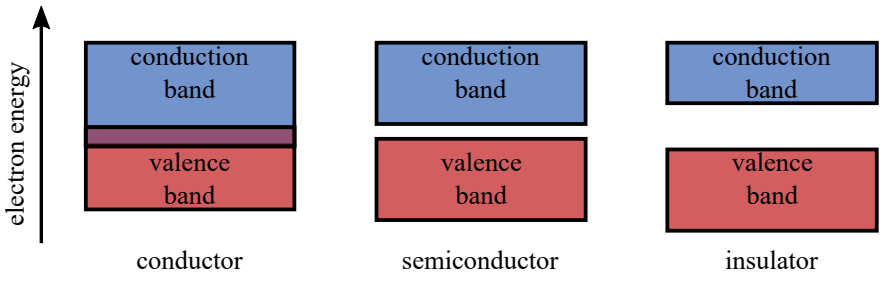

Figure 5.10: Band structure for electron energies in conductors, semiconductors and insulators.

The principle of a semiconductor detector is similar to that of gas-filled detectors but allows for a more compact setup at higher cross sections as the density of the solid semiconductors are several order of magnitude higher. To measure the energy deposited in the material, a voltage is applied to the semiconductor. Fast-moving charged particles

create electron hole pairs in the detector material. The created charge is then collected by the applied voltage. The size of the collected charge is proportional to the particle energy.

Several semiconductor materials can be used for the detection of X-rays; silicon, germanium and cadmium telluride are commonly used. While silicon detectors are the cheapest and most common, their attenuation is too low to detect X-rays with energies around 100 keV. Germanium detectors have a much higher attenuation and offer high resolution due to a small band gap, which is why they are often used in γ spectroscopy. However, germanium detectors are very costly and require cooling with liquid nitrogen, complicating their use and potential pixelated designs. Cadmium telluride offers the highest stopping power of the three materials. In addition, pixelated detectors exist at moderate costs compared to germanium detectors. The major downside is the limited chip size available so far. Nevertheless, the CdTe based HEXITEC was chosen as a detector as it offers the best properties of the available materials, especially in terms of stopping power. This is highlighted in Fig. 5.11, where the total attenuation and the contributions from photoelectric absorption and Compton scattering of 1 mm-thick silicon, germanium and cadmium telluride are compared.

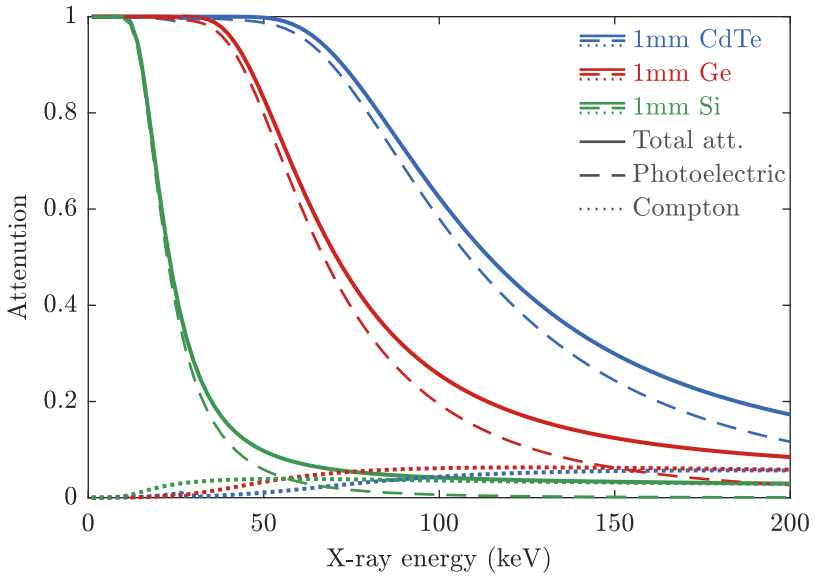

Figure 5.11: Attenuation of X-rays in silicon, germanium and cadmium telluride. Shown are the total attenuation, the attenuation from photoelectric absorption and the attenuation from Compton scattering for all three materials.

5.3.2 HEXITEC layout, calibration and detector effects

As the Thomson beams from LPA are intrinsically short and on the order of femtoseconds, the detection and readout of multiple photons per shot in a single detector crystal is not possible. Therefore, a detector layout with multiple semiconductor crystals is required. The HEXITEC [174, 175] consists of a total of 6400 crystals arranged in a grid of 80 $\times$ 80

crystals. Each pixel has a size of 250 µm by 250 µm and a thickness of 1 mm, resulting in a total area of the chip of 4 cm^2. The size of the individual pixels allows the full energy of the secondary particles created by an incoming X-ray to be deposited in just one pixel in most cases, while at the same time allowing the integration of low-noise electronics in a low-cost bonding process [174]. Including the readout electronics and air cooling, the detector has a size 22 cm × 6 cm × 6 cm, and a weight of 700 g, enabling easy alignment and setup in the laboratory. An image of the detector can be seen in Fig. 5.12

Figure 5.12: Image of the HEXITEC detector (from [175]). The active area of the chip is visible on the right side of the detector. For the experiments, the detector chip was covered by a 1.5 mm thick aluminium plate to reduce the flux of low-energy X-rays on the detector chip.

The detector can be read out at a rate of 10 kHz, which is three orders of magnitude higher than the maximum repetition rate of the laser. For the Thomson experiments, the HEXITEC was operated with an occupancy of about 10%, to minimise the accumulation of several X-rays in one pixel. In addition, charge-sharing algorithms were used to get a better signal-to-noise ratio. Two algorithms that could either add the signal from neighbouring pixels to the pixel with the highest signal (charge-sharing addition) or remove an event in case of any measured signal in the neighbouring pixels (charge-sharing discrimination) are available.

The detector was calibrated using radioactive sources to enable a precise measurement of the X-ray energy with the individual pixels. This was done using ^{241}Am and ^{57}Co sources, offering emission lines at 59.54 keV and 122.06 keV respectively. An example of the spectrum measured using ^{241}Am and the different discrimination modes described above is shown in Fig. 5.13.

The measured spectrum before the calibration shows a peak at an energy of 60.75 keV for all cases with and without charge sharing algorithms, highlighting the necessity of the calibration for a precise measurement of the X-ray energy. Furthermore, the ability to reduce the false counts using a charge-sharing algorithm becomes clear when comparing the detected spectrum without an algorithm in Fig. 5.13a, to that using the addition and discrimination algorithms in Fig. 5.13b and Fig. 5.13c. However, for the addition algorithm, the fluorescence peak develops a low-nergy shoulder, due to the relatively low sensitivity for energies below 4 keV, therefore not being able to fully resolve events where a small amount of the energy is deposited in one or more neighbouring pixels [175]. This also leads to the worst resolution of the main peak of ^{241}Am, with a FWHM of 1.2 keV, compared to the resolution of roughly 1.0 keV for discrimination and the measurement without an

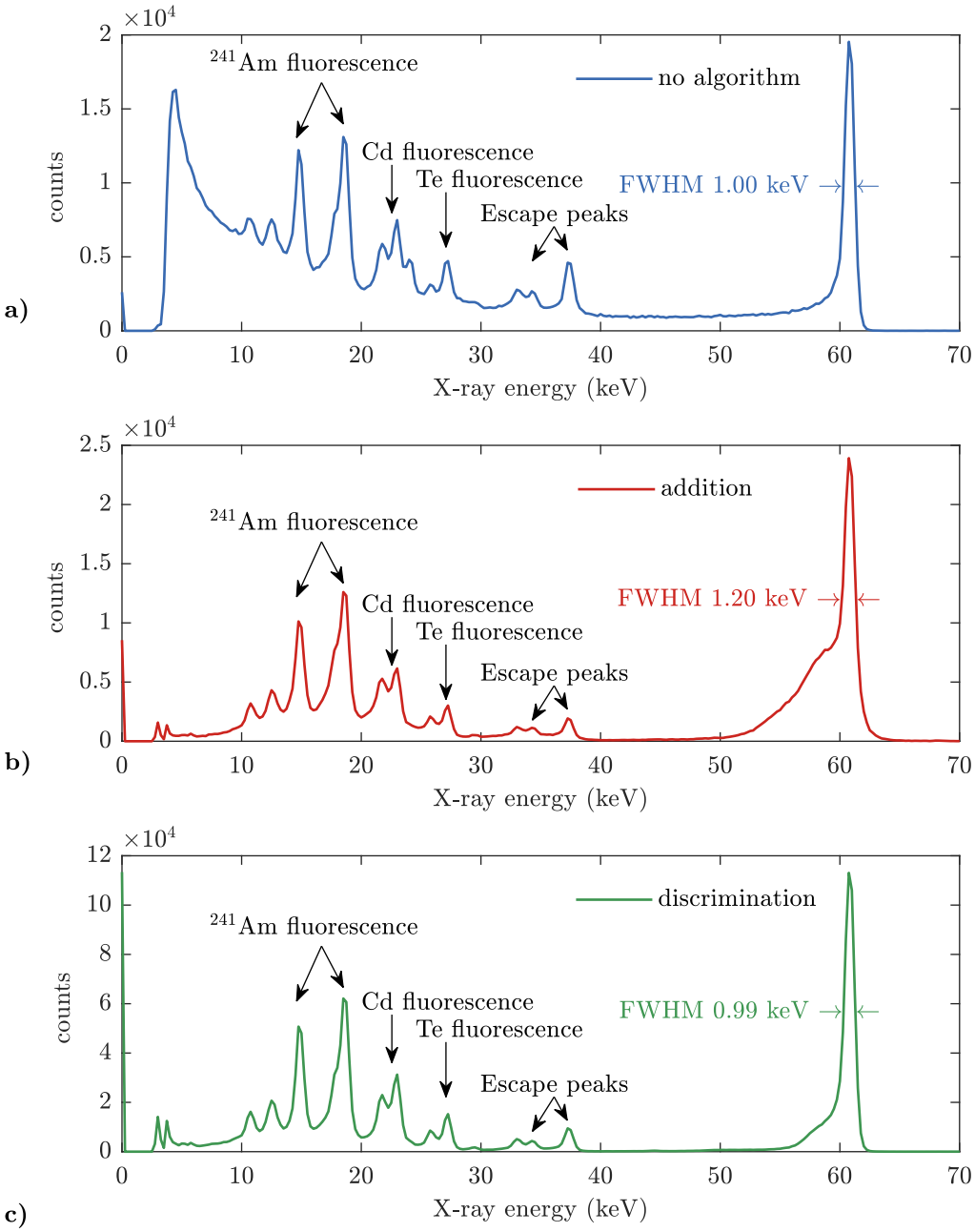

Figure 5.13: Calibration of the HEXITEC using ^{241}Am using different charge-sharing algorithms. a) no algorithm, b) charge-sharing addition, c) charge-sharing discrimination.

algorithm. As the charge-sharing discrimination mode offered the best reduction of false counts while maintaining good resolution, it was also used in the measurements of the Thomson X-ray spectrum.

The fluorescence spectra in Fig. 5.13 also show detector effects that are important for the accurate measurement of the X-ray spectrum. In addition to the ^{241}Am lines, fluorescence lines of cadmium (23 keV) and telluride (27 keV) are visible. These occur when the fluorescence radiation leaves the pixel where the incident X-ray was detected. As an event is either combined (addition) or rejected (discrimination) if the fluorescence X-ray is detected in the neighbouring pixel, the CdTe lines are less dominant with the use of a correction algorithm. However, the lines are visible in all three cases depicted here. Consequently, there is also a significant number of events where the energy of the CdTe fluorescence lines is missing from the full reconstruction of the main ^{241}Am line at 59.54 keV. The detected spectrum has therefore escape peaks at an energy of approximately 25 keV less than the main peak. The height of these escape peaks is also dependent on the X-ray energy due to different cross sections for the interactions of the incoming and fluorescence radiation.

5.3.3 Geant4 simulations

While the detector effects described in the previous section are easily resolvable in the case of a narrow bandwidth X-ray source, as is the case with radioactive isotopes, the effects become more challenging for Thomson spectra with a bandwidth of tens of keV. In such a case, the different energies contribute with different cross sections and peaks cannot be as easily resolved, sometimes even overlapping each other. However, a detailed knowledge of these effects is important for an accurate measurement of the X-ray spectrum. Therefore, the detector was modelled in Geant4 [183–185] to enable a detailed study of detector effects for arbitrary X-ray spectra. Geant4 is a Monte Carlo toolkit for simulating the passage of particles through matter. Using its features such as tracking, variable geometries and run management, an investigation of the processes described above is possible.

In the simulation, not only the interaction of the particles with the detector, but also the passage of the X-rays through materials in front of the HEXITEC chip were simulated. In the experiment, a 200 µm-thick aluminium flange that functioned as vacuum window at the end of the beamline and a 1.5 mm aluminium plate were installed in front of the HEXITEC chip. The latter plate was required to block low-energy radiation present in the lab during the experiments from reach the detector chip, as this would increase the detector occupancy and therefore make a measurement of the X-ray spectrum impossible. Furthermore, the X-ray attenuation probability in the HEXITEC, which is depending on the X-ray energy, as depicted in Fig. 5.11, is taken into account in the simulations. In combination with the charge-sharing algorithms, the energy deposit of X-rays can be corrected using the Geant4 simulations to calculate the initial beam energies from a measurement using the HEXITEC. A comparison of an input spectrum and an output spectrum (energy deposited in the pixels after applying the charge-sharing algorithm) from a Geant4 simulation [186] is shown in Fig. 5.14.

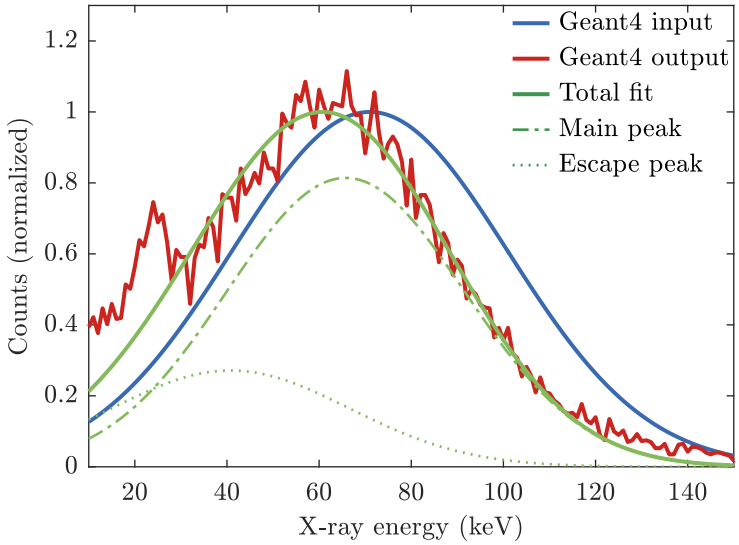

Figure 5.14: Comparison of the input (blue) and output(red) X-ray spectrum from a Geant4 simulation [186]. In addition, the fitting routine, consisting of a Gaussian fit for the main peak and a second Gaussian for the escape peak is shown. The peak of the output spectrum around 25 keV arises from CdTe fluorescence and is neglected in the fitting routine as is described above.

In the figure, the fitting routine, consisting of the sum of two Gaussian fits, is shown. The larger Gaussian fit corresponds to the directly measured X-rays from the incoming beam and is defined as the main peak. In the case shown here, the main peak is shifted to lower energies compared to the input spectrum due to the lower total attenuation of high-energy X-rays in general and the higher cross section for Compton scattering at high energies. The high-energy X-rays are therefore less likely to be detected and especially to be fully resolved in one pixel as is required due to the charge-sharing algorithm. The second Gaussian fit corresponds to the contribution from the escape peaks. The second Gaussian is therefore defined to have a central energy of 25 keV less than the main fit, due to the fluorescence lines of cadmium and telluride between 23 keV and 27 keV visible in Fig. 5.13. The amplitude of the second fit was scaled to 1/3 of the height of the main fit, which was found to be optimal for fitting using simulated distributions from X-ray beams with mean input energies between 30 keV and 100 keV. The region around the fluorescence peaks of 22 keV to 28 keV were excluded from the fitting routine. Lastly, counts with an energy of less than 10 keV were excluded from the fitting routine and are usually not shown in the graphs. These counts are very unlikely to originate from X-rays hitting the detector, as the 1.7 mm-thick aluminium in front of the detector chip leads to a transmission probability of less than 10^{-5} for energies below 10 keV [65]. These counts will therefore most likely originate from noisy detector pixels or not fully resolved events.

To estimate the influence of detector performance, transmission of the X-ray beamline

and attenuation cross section of the detector on the measured Thomson spectra, simulations similar to the scenario depicted in Fig. 5.14 were performed for X-ray beams with central input energies from 30 keV to 100 keV. The peak position of the main Gaussian distribution of the fit of the output spectrum as a function of the central input energy is shown in Fig. 5.15.

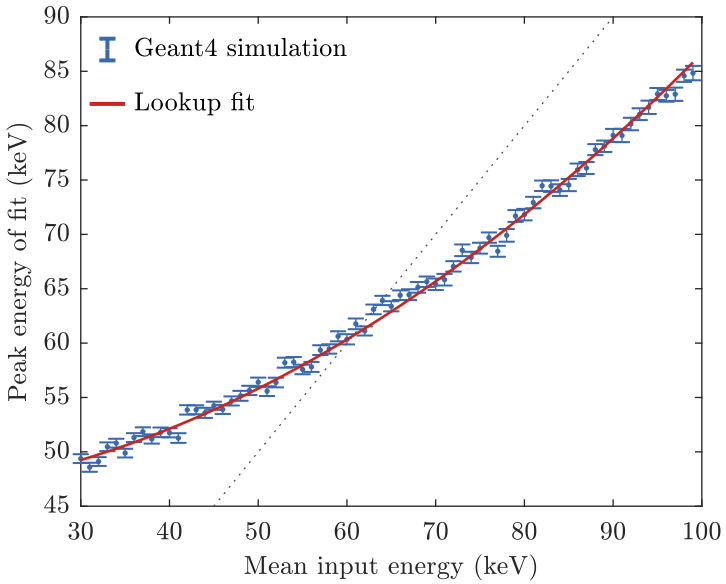

Figure 5.15: Peak position of the mean Gaussian fit as a function of the mean input energy from a Geant4 simulations with central beam energies of 30 keV to 100 keV [186]. In addition, a quadratic fit is shown that is used for the calculation of the peak energy from measured input spectra. The grey dotted line corresponds to a ratio of 1.

The measurement will overestimate the peak X-ray energy for beams with a central energy with 55 keV or less. Beams with a central energy of 30 keV or less cannot be resolved at all. This is due to the filtering of X-rays from the aluminium, which was required to filter out background radiation present in the experiments from e.g. bremsstrahlung. Furthermore, X-ray beams with an energy of more than 65 keV are measured with lower energy by the HEXITEC and the fitting routine due to a lower detection cross sections of these X-ray energies. A quadratic fit to the simulation results was used to correct the HEXITEC measurements of the Thomson spectrum to obtain the central energy of the incoming X-ray beam.

5.4 Alignment and optimisation of the Thomson signal

In Thomson experiments, the alignment of the scattering laser and the electron beam is very challenging as it needs to be done with a resolution of femtoseconds in time and micrometers in space. In previous collaborations with other groups [187, 188], the two focussed laser pulses were overlapped in time using a diffraction grating, which enabled

temporal alignment by spectral interferometry on the order of tens of femtoseconds [189]. In the experiments planned in the BOND lab, this method could not be implemented as the spherical mirror and the parabola had the same focal length, meaning the focused Thomson laser could potentially be recollimated and sent backwards into the laser chain, leading to serious damage to the laser system. Therefore, the ionisation of the gas of both laser pulses was imaged using the perpendicular probe beam, similar as was done previously in the other Thomson experiments [166]. By shifting the gas jet and the timing of the three individual beams, this technique allows the temporal overlap at a desired plane to be found. A drawback of the method is that the temporal overlap is independent of the spatial overlap and the scattering angle of 7 degrees requires the spatial overlap and the temporal overlap to be done in the same plane, since, in contrast to head-on scattering, the beams only overlap over a distance of a few hundred micrometers.

The spatial overlap was done indirectly by overlapping the two laser pulses rather than by overlapping electron beam and Thomson focus. For the alignment of the two laser pulses, a small scattering screen with a size of roughly $1\,\mathrm{cm}^2$ and a thickness of 120 um was driven into the overlap plane and imaged with a camera. Due to the imaging quality of the screen, the rough surface of the scattering screen, as well as the size of the main laser pulse, which was not in focus at the desired overlap plane this method was only accurate to tens of micrometer. In addition, small tilts and bends of the overlap screen extended its thickness of 120 µm to an effective thickness of about 300 µm when imaged by the probe laser. For example, a tilt of the 1 cm wide scatter screen by 1 degree would increase the effective size by approximately 175 µm. The longitudinal position of the spatial-overlap plane can therefore only be determined with an accuracy of the effective thickness leading to an uncertainty with respect to the temporal overlap plane of 300 µm, which corresponds to a relative timing uncertainty of the the beams of approximately 1 ps.

After performing the temporal and spatial overlap as described above, the fine tuning of the timing had to be done by optimisation of the Thomson yield. The signal was measured using a scintillator which was imaged using a very sensitive EMCCD camera. At first, a 10 mm thick CsI(Tl) crystal was used as the scintillator, which offers high light output and 100% detection efficiency for the energies of interest. However, the relatively thick scintillator also has a high attenuation of the broadband bremsstrahlung background and any possible Thomson signal was overlaid by bremsstrahlung background with bremsstrahlung energies of up to tens of MeV. The CsI(Tl) crystal was therefore exchanged with the same type of DRZ screen that was used for measurements of the electron pointing, energy and charge described in the previous chapter. The thickness of the phosphor layer of 310 µm resulted in a reasonable attenuation and detection of the Thomson X-rays while reducing the attenuation of the high-energy bremsstrahlung and its energy deposition by several orders of magnitude.

Using this improved signal-to-noise ratio, the Thomson yield could be optimised by timing scans. To verify that the signal is coming from Thomson radiation, alternating

measurements were performed with and without the Thomson laser at five scan points each, with 25 shots at each scan point. Results of this scan are depicted in Fig. 5.16. The

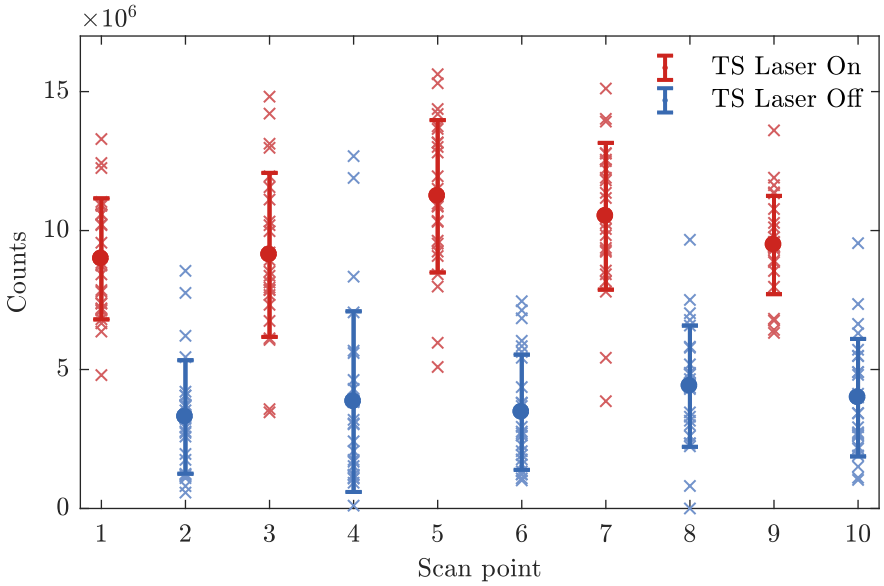

Figure 5.16: Signal on EMCCD camera imaging the scintillator screen with and without Thomson laser. At each scan point 25 shots were taken.

figure shows a clear difference of the signal level with and without the Thomson laser. The camera detects three times as many photons in scans where the Thomson laser is turned on. The difference in the signal level is also mostly outside the error bounds, which is the standard deviation of the counts of the 25 individual shots at each scan point. As the measurements are shown in the order they were taken and stable electrons with the same amount of charge were recorded during the entire time, a difference in the signal level due to drifts can be ruled out. Figure 5.16 represents the first successful Thomson interaction measured in the BOND laboratory.

5.5 Measurement of the electron energy

After optimisation, the Thomson signal was used to measure the energy of the electron beam. As there is a direct correlation of the Thomson photon energy and the electron energy via Eq. 5.20, this required the measurement of the Thomson spectrum. Therefore, the scintillator setup was exchanged with the HEXITEC as described in Sec. 5.2. Afterwards, the signal level on the HEXITEC was adjusted to enable single-photon counting. For the optimisation of the Thomson alignment, the number of photons was maximised for a better signal-to-noise ratio. When using the HEXITEC, the amount of photons that were detected using these settings exceeded the limit required for single photon counting of a few hundred counts per shot on the chip. Hence, the distance from the HEXITEC to the Thomson interaction point was maximised in order to reduce the flux on the chip.

The distance was limited by the electron-beam block installed in the Thomson path, leading to a maximum distance of 7.8 m from the gas jet. This distance was used in the experiments, which meant that the size of the detector chip of 2 cm by 2 cm resulted in an opening angle of ± 1.25 mrad. To further decrease the amount of Thomson signal as well as the background of bremsstrahlung and enable single-photon counting, the charge of the electron beams was reduced to about 2 pC by reducing the laser intensity, resulting in approximately 500 photons measured by the detector chip per shot. These photons originate from both the Thomson beam and background from bremsstrahlung and its secondary radiation hitting the detector. A comparison of the counts on the HEXITEC with and without the Thomson laser revealed that roughly (48 ± 12) % of the registered counts were coming from background radiation in these experiments. Furthermore, roughly 55% of the events are shared between multiple pixels [175] and therefore dismissed from the charge-sharing discrimination as was described above. In total, this results in an energy measurement of roughly 125-150 photons per shot. Consequently, the Thomson spectrum was measured in a multi shot approach in order to get a meaningful spectrum.

To be able to average the spectrum from multiple shots, a stable electron source is required. Therefore, the STII electron source was used, which can deliver stable electron beams over several hours and tens of thousands of shots as was described in Chapter 4. As explained above, the charge of these beams was tuned down to reduce the flux on the detector resulting in (2.7 ± 1.0) pC per shot. The electrons had a divergence of 8.4 mrad FWHM with a pointing fluctuation of 1.7 mrad and an energy spectrum peaked at 62 MeV. The product of divergence and gamma factor resulted in a value of 0.7. According to the measurements by Krämer *et al.* [162] this results in a correction factor of 0.9, which was used for this work. For the measurement of the Thomson spectrum, the signal of 280 shots was integrated. To estimate the background contribution in the measured spectrum, the measurement was repeated without the Thomson laser. The measured on-axis spectra with and without the Thomson laser as well as the resulting background-subtracted spectrum is depicted in Fig. 5.17. The background measurement was repeated three times and averaged to reduce the noise.

The Thomson spectrum can be used to determine the electron energy as the relation in Eq. 5.20 shows, but a full reconstruction of the electron spectrum from the on-axis Thomson spectrum is usually very complicated. In general, it requires a full analysis of the Thomson interaction to determine the effective electron and laser overlap [150, 162, 172]. The broadening effects described in Sec 5.1 further hinder the reconstruction and numerical integration is required to solve the broadening exactly [172]. However, in case of the electron beams used here, the relative Thomson bandwidth defined in Eq. 5.18 is dominated by the electron bandwidth rather than other factors, so it can be used to approximate the full electron spectrum. For a more precise reconstruction of the electron spectrum from the Thomson beam a detailed knowledge of the interaction geometry of electron beam and laser pulse is required. Due to uncertainties in the overlap procedure

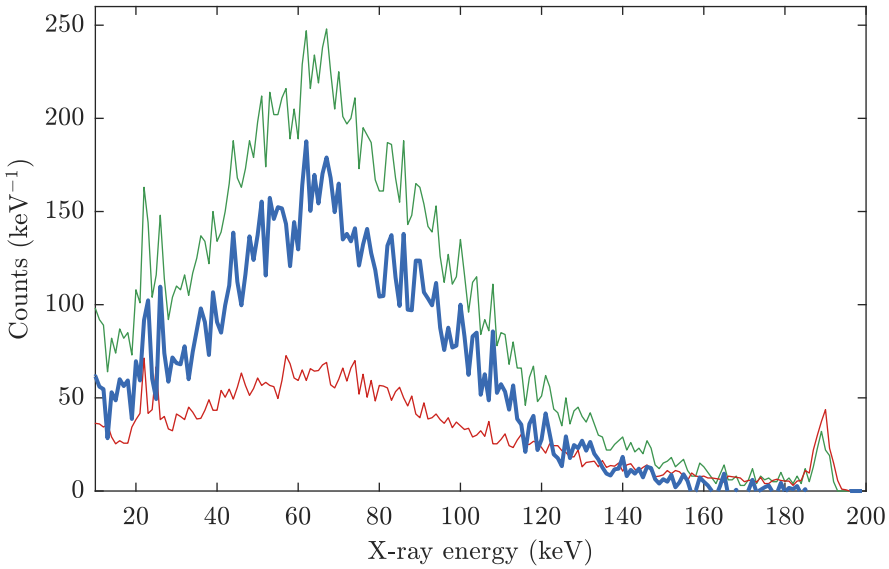

Figure 5.17: Comparison of the signal spectrum (green), the background spectrum averaged over three runs (red) and the resulting background subtracted Thomson spectrum (blue).

described in Sec. 5.4, such an analysis is not possible in this case.

To use the Thomson spectrum to calculate the electron energy, it has to be corrected for attenuation effects described in Sec. 5.3. Therefore, the same fitting routine which was used for the HEXITEC data obtained from Geant4 simulation was applied to the background-subtracted Thomson spectrum shown in Fig. 5.17. This is depicted in Fig. 5.18, where a background-subtracted measured spectrum, its fit, and a HEXITEC spectrum from the Geant4 simulation with similar fitting parameters are shown. As can be seen in the figure, both measured and simulated spectra are very similar. Therefore, the input spectrum of the Geant4 simulation is used to compensate for detector effects and beamline attenuation of the Thomson measurement in further calculations. For a more general solution, it is also possible to use the peak position of the main fit and correct it using the lookup fit shown in Fig. 5.15. While this comes at the cost of losing bandwidth information, this method can be applied to any peaked Thomson spectrum, regardless of the cause of the broadening; the reconstruction of the electron peak energy is sufficient for many applications, as will be shown later.

The input spectrum for the Geant4 simulation which resulted in the best fit results compared to the measured Thomson spectrum is then used to calculate the electron spectrum using Eq. 5.20 and under the assumption of constant emission and detection rate for all X-ray energies. As there is a quadratic correlation between Thomson and electron energies, the resulting spectrum has to be scaled to give the amount of charge in a constant energy bandwidth. The resulting spectrum is depicted in Fig. 5.19, where it is also compared to the measured spectrum and results of a PIC simulation of the acceleration

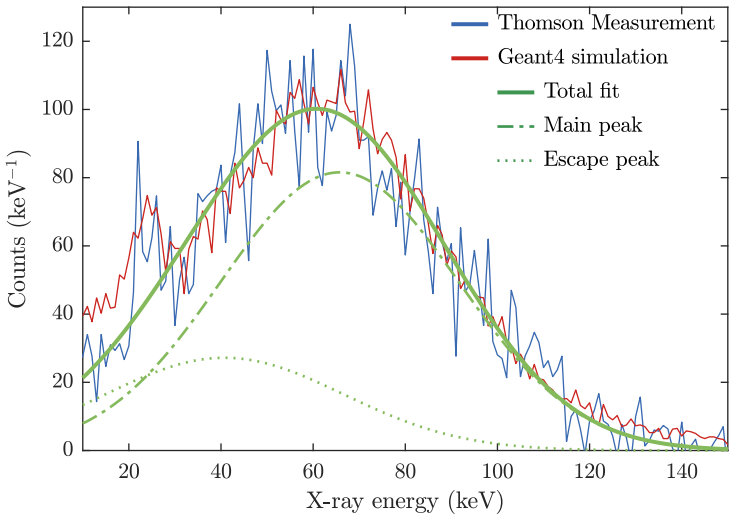

Figure 5.18: Comparison of measured Thomson spectrum and spectrum obtained from Geant4 simulation [186] with similar fitting parameters. In addition, the fit for the measured Thomson spectrum is shown with its contribution from the main fit and the escape peak.

previously shown in Fig. 4.22 and good agreement of the mean energy of the spectrometer measurement, the PIC simulation and the reconstruction of the spectrum from the Thomson measurement is visible in Fig. 5.19. However, the reconstruction of the Thomson measurement underestimates the resulting electron bandwidth due to simplifications made for the calculation, especially for lower energies. This is most likely originating from three major factors which are partly linked and would require exact knowledge of overlap of laser and electron beam for a correct implementation. A compensation to overcome errors due to the simplifications is therefore not possible here, but their effects on the spectrum will be briefly discussed. It should also be noted that the measurement of the electron spectrum using both the electron spectrometer and the Thomson spectrum are are done by averaging hundreds of shots. A substructure of the electron energy distribution as is the case for the depicted spectrum of the PIC simulation is therefore unlikely to be present, for the spectrum obtained with the electron spectrometer or via Thomson measurements.

The input beam of the depicted Geant4 simulation is only an estimate of the produced Thomson beam. While the result of the Geant4 simulation and measured Thomson spectrum seem to agree quite well, small differences cannot be resolved. Due to the statistical nature of the attenuation effects described earlier, a lot more counts would be required to see differences in the two spectra. However, the use of the input spectrum is probably the best solution to correct the measured Thomson spectrum for detector effects and attenuation of low-energy X-rays from the beam transport through the aluminium and the lower probability of detection for high-energy X-rays. Especially in the wings of the spectrum where fewer counts are present, this method lacks accuracy due to the low number of

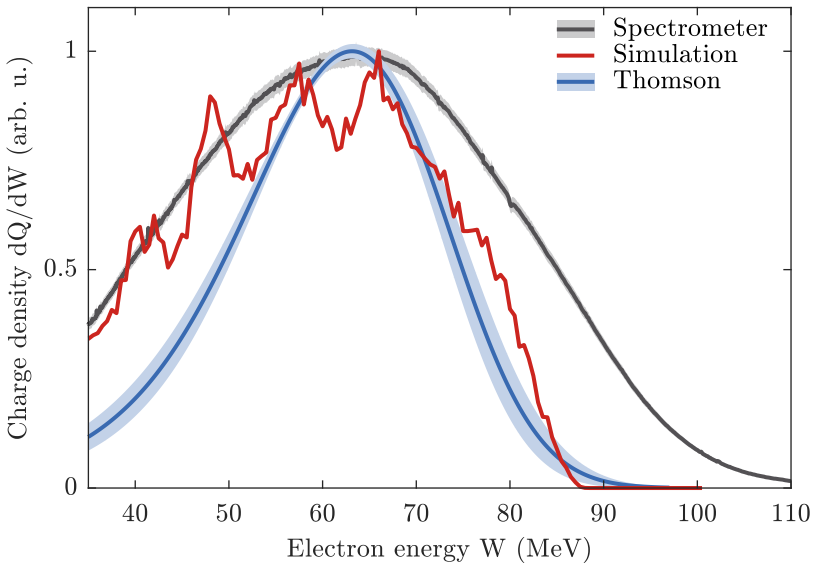

Figure 5.19: Comparison of electron spectrum obtained from measurements using the electron spectrometer, PIC simulation and conversion of the measured Thomson spectrum using Eq. 5.20.

expected counts and consequently high statistical uncertainties.

Another important factor is the assumption of uniform production of radiation for all electron energies. This assumption is important for the transformation of the photon energies into electron energies. In the experiment, the laser spot size of the focussed laser exceeds the expected electron-beam size and the overlap was done behind the plasma. However, the exact position of the overlap (other than it being outside the plasma) and the initial size of electron beam are unknown. In combination with the electron divergence it is therefore possible that electrons with different energies might experience different laser intensities and thus also emit a photon with different probabilities as the scattering of photons is more likely using a high-intensity laser. For example, the low-energy electrons could diverge faster, such that they are overlapped with low-intensity regions of the laser focus and less Thomson photons are scattered from low-energy electrons. Similarly, the astigmatic focus of the Thomson laser could lead to different cross sections for different electron energies if the electron energies separate in a short drift due to different divergences.

Lastly, the detection probability of a photon scattered by an electron was assumed to be constant. However, this condition only holds as long as the electron beam divergence is constant and larger than the emission angle ($1/\gamma$), as in this case the probability of a scattered photon reaching the detector chip would be constant for all energies. According to FBPIC simulations, this condition does not hold and there is a negative correlation of electron energy and divergence (as expected), as is depicted in Fig. 4.20a in Chapter 4. In addition, the Thomson scattering opening angle ($1/\gamma$) is higher than the divergence of the

electrons in the PIC simulation, especially for electrons with low energies. Consequently, the probability of a Thomson photon from an electron with a small energy reaching the detector chip with an acceptance angle of 1.25 mrad is lower than that of a highly energetic electron, which is more likely to emit a photon close to the axis. This is probably the most important factor, as can be seen when comparing the spectra in Fig. 5.19. Again, to compensate this effect, the exact geometries of the overlap and the resulting emission rates would have to be studied.

Nevertheless, the electron spectrum resulting from the calculation from the TS measurement seems to be a good estimation of the electron beams obtained from PIC simulations, as depicted in Fig. 5.19. However, while the electron spectrometer might overestimate the electron bandwidth due to the divergence of the beams in the dispersive axis and the low resolution of the phosphor screen used, the method described above will most likely underestimate the bandwidth. It should however again be noted that this direct measurement is restricted to a Thomson beam with a bandwidth determined by broadening from the electron bandwidth. In other cases, a deconvolution of the Thomson spectrum is required to get information on the spectral shape of the electron beam. The more general reconstruction of the electron peak energy from the peak of the Thomson beam is applicable to all (quasi-monoenergetic) electron beams and will be used to measure the acceleration gradient in the next section.

5.6 Measurement of the energy evolution

After demonstrating the general concept of measuring the electron peak energy from the peak of the Thomson spectrum, the principle was extended to the measurement of the electron-energy evolution inside the plasma. For this measurement, the ability of transporting a Thomson beam, which contains information about the electron beam, was used, to extract the electron beam information at a distance of several meters from the interaction point. Using the translation stage of the spherical mirror and the delay stage in the LPA laser arm, the overlap of Thomson laser and electron beam was moved into the plasma and the measurement described in the previous section was performed at different overlap positions. Three measured Thomson spectra and corresponding electron spectra at these positions are depicted in Fig. 5.20.

In the figure, a decrease of the Thomson energy when the overlap region is outside the plasma (Fig. 5.20a) compared to inside the plasma (Fig. 5.20b+c) is clearly visible. As the final electron energy measured using the spectrometer shows no significant change for the three different overlap positions (right panels of Fig. 5.20), and only the energy calculated from the Thomson signal using Eq. 5.20 decreases, the change in energy must originate from a Thomson interaction with electrons inside the plasma that have not yet reached the final energy. The good agreement of peak energy obtained from calculations and the spectra measured using the electron spectrometer in case of an overlap outside the

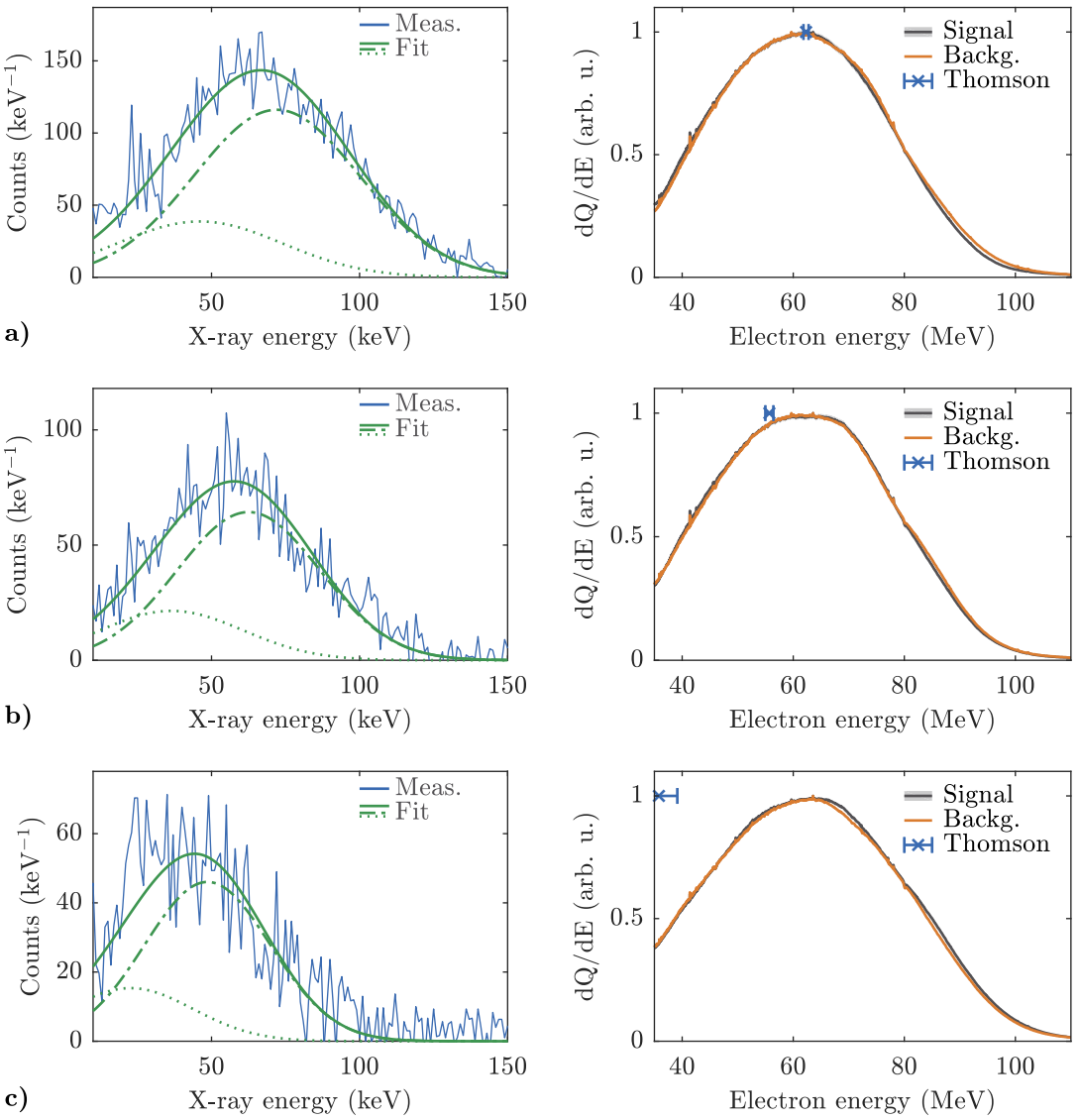

Figure 5.20: Comparison of Thomson and electron spectra at three different overlap positions. The overlap is moved from a) outside the plasma, to b) the end of the plasma and c) towards the center of the plasma. On the left side, the background subtracted Thomson spectra are shown together with the fitting routine introduced in Sec. 5.3. The dashed-dotted line represents the main Gaussian fit and the dotted line the contribution from the escape peaks. On the right side, signal (Thomson laser on, black) and background (Thomson laser off, orange) electron spectra are shown, which were measured using the electron spectrometer. For a comparison, the electron energy calculated via Eq. 5.20 using the corresponding Thomson spectra on the left side is also plotted as blue cross.

plasma shows the potential of Thomson scattering to determine the electron peak energy. In addition, a comparison of the average electron spectra measured using the electron spectrometer where the Thomson laser was on (signal, black line) and without the Thomson laser (background, orange line) in case of all three depicted cases clearly emphasises the non-invasive character of these measurements, since no significant difference outside

the error bounds is visible for signal and background spectra.

To get a full picture of the energy evolution of the electron beam inside the plasma, the measurement was performed at 20 different overlap positions. This way, the energy evolution of the electrons could be measured over a distance of approximately 400 µm. The results of this scan are shown, together with the energy evolution obtained from PIC simulations in Fig. 5.21. To align the energy gain of the experimental data with the simulation results, least-square minimisation was used. This was necessary due to the relative uncertainty of the overlap position, as explained in Sec. 5.4. It should be noted that the relative distance of the measurement positions was well known in the experiment and not shifted in this process. Only the absolute coordinate of the measurement block was determined with respect to the energy evolution obtained from the simulation.

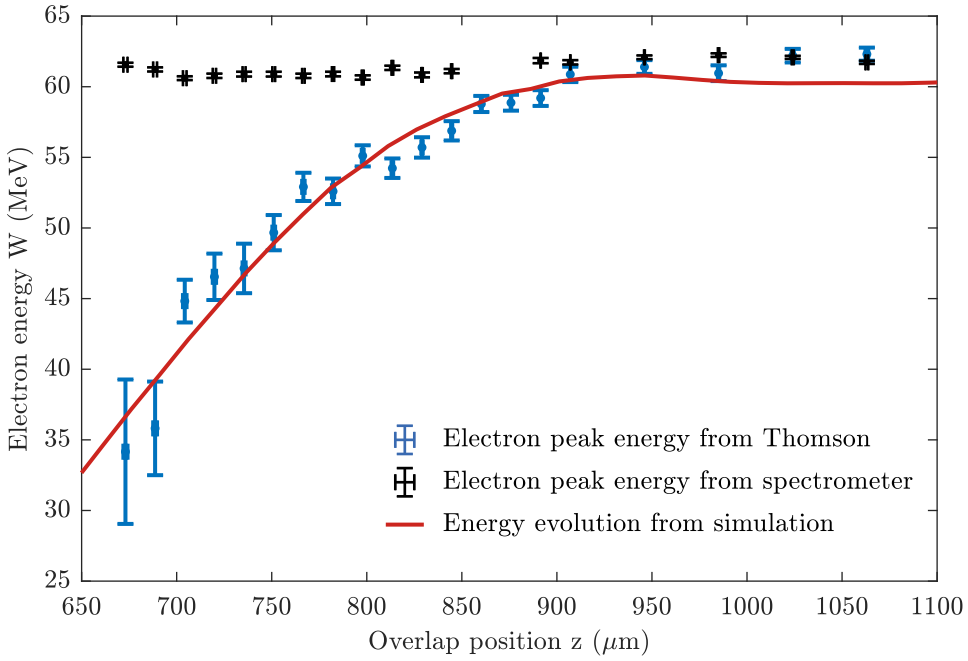

Figure 5.21: Energy evolution during acceleration in the wakefield measured via Thomson scattering (blue). In addition, the energy evolution obtained from simulations (red) and the final energy of the electrons at each measurement position is shown (black). The error bars of the Thomson measurement represent the quadratic sum of the 1 sigma confidence interval of the fit and 500 eV to account for the detector resolution. Afterwards, this photon-energy uncertainty is converted into an uncertainty of the electron energy using the quadratic fit introduced in Fig. 5.15. The error bars of the spectrometer peak consists of the standard deviation of the peak position of Gaussian fits of the 350 individual shots at each measurement position.

The measurement via Thomson scattering shows an energy increase from 33 keV to about 61 keV over a distance of 250 µm. Over the following 150 µm, the energy stays constant at the level of the spectrometer measurements, showing that these measurements were done after the electrons left the plasma and no longer change their energy. Throughout the measurement, the peak energy measured on the spectrometer does not change,

again indicating the non-invasive measurement of the electron energy via Thomson scattering. In addition, the Thomson measurement of the energy evolution has very good agreement with the simulated energy evolution as is shown in the figure, displaying the power of the technique. Only in the region beyond 1000 µm does the energy evolution in simulation and measurement deviate. This could be explained by the approximation of the plasma density depicted in Fig. 4.19 which deviates from the measured profile in this region and therefore might lead to differences in the simulated acceleration process.

The method demonstrated here to measure the electron-energy evolution is the first non-invasive in-situ measurement of electrons from a wakefield accelerator. As only the measurement of the peak energy of the Thomson spectrum is required, as was shown above (assuming a quasi mono-energetic electron spectrum), this technique is applicable to a wide energy range due to the availability of a variety of different spectrometer types for X- and γ-ray energies between a few keV and hundreds of MeV. Examples are X-ray cameras [190] also used at synchrotrons for up to tens of keV, pixelated semi-conductors as the HEXITEC [175] or Ross-filters [191] for energies up to a few hundred keV, stack calorimeters [192, 193] and Compton-based detectors [194] for energies of up to tens of MeV and finally scintillator based methods that can measure energies of beyond 10 MeV [195]. Furthermore, the output energy of the Thomson beam can be slightly tuned by changing the wavelength of the scattering laser to be able to detect X- or γ-rays in a favourable energy regime.

The measurement of electron beams during acceleration can therefore be applied at many plasma-based facilities and could help to understand and improve the acceleration process and subsequently increase the quality of the beams. The usefulness of such in-situ measurements is shown in the next section, where studies of the dephasing of the STII electron beams are described using the experimental data of the measurement of the energy-evolution.

5.7 Dephasing studies using in-situ energy measurements

The measurement of the energy evolution inside the plasma described in the previous section revealed acceleration of the electron bunch over a distance of about 250 µm. At the point of the first measurement position depicted in Fig. 5.21 the electron energy is already at an energy of 34 MeV. Therefore, the total acceleration length can be assumed to be much longer than the investigated length of 250 µm. According to simulations, it is approximately 500 µm, exceeding the theoretical value of the dephasing length of 350 µm for the measured plasma density of $1.9 \times 10^{19}\,\mathrm{cm}^{-3}$, which can be calculated from Eq. 2.11, as discussed in Chapter 2. Furthermore, the energy of the electron beams presented here and measured using the electron spectrometer and via Thomson scattering is higher than predicted by 3D non-linear theory [78]. Consequently, some effect must increase the dephasing length of the beams present in this acceleration scheme.

As mentioned in Sec. 2.5, several techniques were proposed and demonstrated to accelerate over distances exceeding the dephasing length [79–83]. A parameter not yet investigated in the context of dephasing is the laser strength a_0, despite its known influence on the plasma wavelength [196]. In the case of the STII electron beams introduced in Chap. 4, a_0 is decreasing over the entire acceleration length as was depicted in Fig. 4.23. The use of these simulations allows the speed of the maximum accelerating field in the simulations to be compared to the phase velocity of a wake expected from theory. The phase velocity of the wake v_ϕ can be defined as the difference of the group velocity of the laser and the etching velocity, resulting in [78]:

$$v_\phi = c\left(1 - \frac{3\omega_p^2}{2\omega_0^2}\right). \tag{5.21}$$

This comparison is shown in Fig. 5.22, where also the plasma density profile and the evolution of a_0 are shown again for easier comparison.

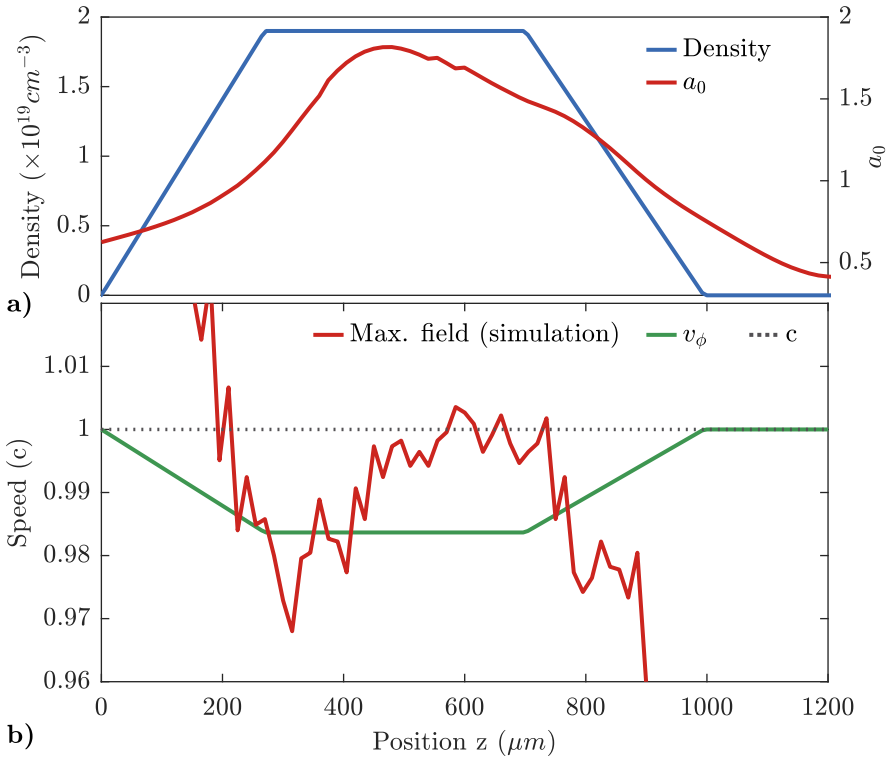

Figure 5.22: (a) plasma density evolution and evolution of a_0 from simulation as shown in Fig. 4.19 and Fig. 4.23. (b) comparison of the speed of the maximum of the accelerating field, the theoretical phase velocity of the wake according to [78] and the speed of the electron bunch (speed of light c)

As can be seen in the figure, the speed of the maximum of the accelerating field in the simulation exceeds the theoretical phase velocity of the wake for most of the accelerating distance. Both values agree quite well only around the peak value of the a_0, where a_0 is roughly constant. In areas of a decreasing (increasing) a_0, the speed of the maximum of the

accelerating field is higher (lower) due to the decreasing (increasing) plasma wavelength from the influence of the laser intensity. In case of a decreasing a_0, as in this case, the acceleration over larger distances is therefore possible as shown in Fig. 5.22b.

To be able to quantify the influence of this effect on the presented acceleration scheme, the experimental data and the results from simulation are compared to a model that calculates the energy gain of the electron bunch while neglecting the effect of the laser intensity on the plasma wavelength. For this model, the longitudinal lineout of the on-axis accelerating field at the position of the first measurement point is taken from the simulation. The lineout and the position of the electron bunch at this point are shown in Fig. 5.23.

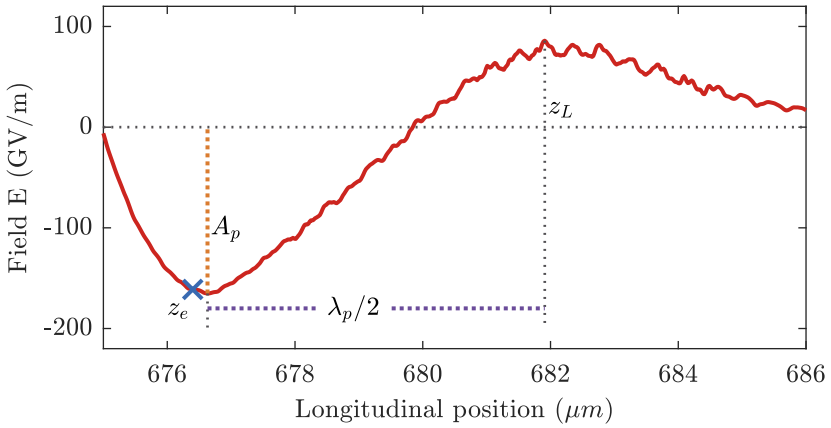

Figure 5.23: The on-axis longitudinal accelerating field at the position of the first Thomson measurement (red line). In addition the position of the electron bunch (z_e), the position of the laser (z_L) and the amplitude of the accelerating field (A_p) are shown. The distance between A_p and z_L is defined as half the plasma wavelength ($\lambda_p/2$) to allow the scaling of this lineout according to the density later on.

To calculate the energy gain over the remaining distance without the effect of the decreasing a_0 on the plasma wavelength, four steps are performed. First, the amplitude of the longitudinal on-axis field A_p is scaled according to the amplitude at that position in the simulation (compare black dotted line in Fig. 5.24). Afterwards, the length of the electric field is scaled by the plasma wavelength λ_p as a function of the plasma density, as most of the measurements were performed in the plasma down-ramp region. In the third step, the electrons are moved forward with the speed of light and the resultant energy gain is calculated using the field at the position of the electron bunch z_e. Lastly, the laser position z_L is then moved forward with v_ϕ according to the plasma density as shown in Fig. 5.22b.

A comparison of the electric field seen by the electron bunch in the simulation and the field calculated using the model described above as a function of electron-bunch position is depicted in Fig. 5.24. The field is also compared to the maximum available field at each electron-bunch position according to the simulation that was used for the scaling of the

field amplitude. A significant effect of the laser intensity on the dephasing is visible when comparing the two cases. It should be noted that at the position of the first measurement ($z_e \approx 675\,\mu m$), the electron bunch is located behind the maximum field amplitude as is shown in Fig. 5.23. In the calculations using the simplified model, the electron bunch is much faster than the field amplitude and therefore reaches the amplitude after only a few microns of propagation. In the simulations, this process only occurs in the density down-ramp, where the wakefield is elongated due to the decrease of the plasma density. Consequently, in the model, the electron bunch dephases faster and is even decelerated for more than 100 µm at the end of the plasma.

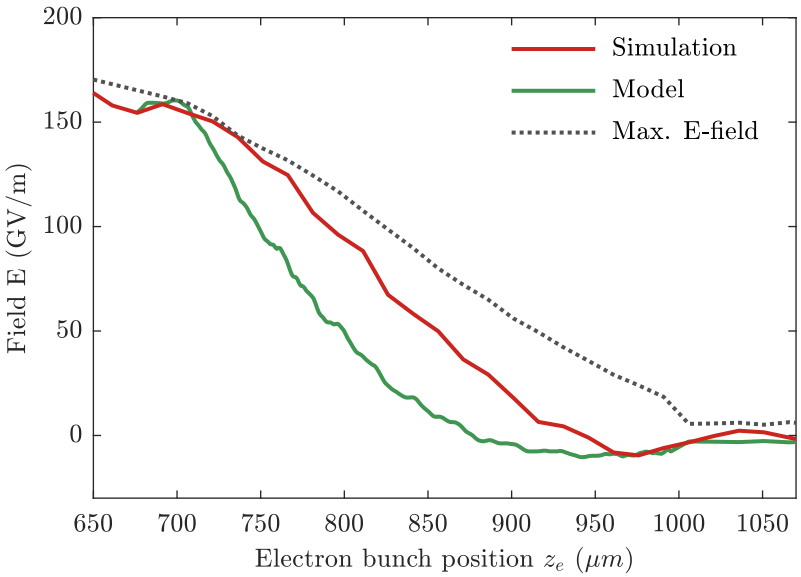

Figure 5.24: Accelerating field as function of the electron-bunch position in the simulation, for the model, and the amplitude of the accelerating field. The sign of the field is flipped for an easier comparison.

The integral of the fields shown in 5.24 allows a comparison between the calculated energy gain from the model and the simulated energy gain. Both energy evolutions were then compared to the measured energy evolution using Thomson scattering, as described in Sec. 5.6. This is depicted in Fig. 5.25. Here, the electron energies calculated from the model fail to predict the energy evolution measured using Thomson scattering. Already after about 100 µm there is a clear difference between the modelled energies and the measurements, showing the suitability of Thomson measurements for detailed studies of the electron bunches during acceleration. In addition, the differences between Thomson measurement and simulation on the one hand and the energy evolution calculation without the influence of the laser intensity on the wakefield length on the other hand shows that this factor needs to be taken into account to increase the quality of electron bunches accelerated using laser wakefield acceleration.

These studies of dephasing using Thomson scattering have shown the importance of

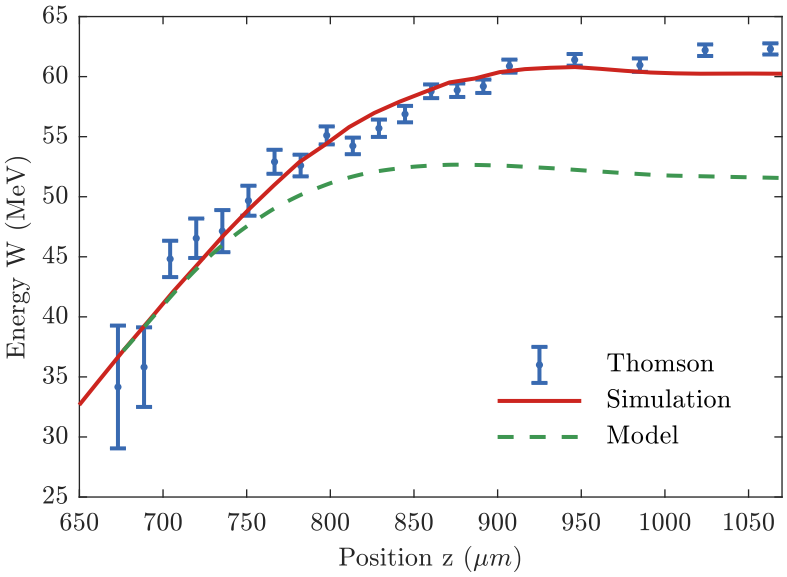

Figure 5.25: Comparison of the electron evolution measured using Thomson scattering, the simulation and the simplified model.

in-situ measurements for wakefield acceleration. The variety of detectors available for a wide range of X- and γ-ray energies make these measurements applicable to many plasma acceleration setups, such as e.g. FLASHForward, where acceleration distances of several centimeters were already demonstrated. A measurement of the electron-energy evolution of both driver and witness beams could therefore help to increase the energy of the produced beams.

In addition, this method could also be extended to further electron parameters such as pointing, divergence, or emittance measurements [10–12], which have been achieved previously with Thomson scattering. The method described here could therefore be used to get a full picture of the electron bunch and its evolution both inside and outside the plasma. For many issues of plasma acceleration, such as for example hosing [197–199] or emittance growth [200, 201] in-situ Thomson measurements could be a key tool to study these effects experimentally as has been shown in the dephasing studies reported here.

Chapter 6

Summary and outlook

In this thesis, fundamental work towards the use of laser-plasma acceleration (LPA) in industrial and medical applications was done by investigating the long-term stability of an LPA setup and developing a new diagnostic technique that is capable of measuring electron parameters inside the wakefield. Several injection techniques were tested on their ability to produce stable electron beams that can be used for the development of new diagnostic techniques and proof-of-principle experiments for new medical applications using LPA. The electron beams accelerated via ionisation injection offered more stable beams compared to the self-injected and shock-front-injected electron beams, especially in terms of pointing and spectral stability, which were crucial for the planned experiments. By optimising the experimental parameters, the injection method was transferred to a self-truncated ionisation-injection regime, thereby decreasing the spectral bandwidth and the divergence of the produced electron beams. Further work regarding stabilisation of laser and plasma parameters and a new differential pumping system to increase the repetition rate of the system enabled the electron source to be used to perform first tests of X-ray fluorescence imaging using an LPA electron beam.

The electron source has been shown to produce stable electron beams at high repetition rate over 8 hours. A total of 72000 electron bunches were produced at a repetition rate of 2.5 Hz with 100% injection efficiency. The average charge of these beams stayed constant over the entire duration of the run, showing the stability of the injection mechanism. At the same time, the peak energy of the produced beams decreased by 7%. The decrease in energy cannot be fully explained, especially as only a small subset of the available diagnostics were saved during this run to decrease the disk usage. A likely explanation for decrease of the peak energy is heating of the laser compressor gratings and a resulting shift of the longitudinal focus position. This effect was later observed in studies of the grating behaviour at high repetition rates [155].

This long-term stability study has demonstrated that further investigations of the topic are necessary. In the meantime, a new grating with better thermal properties was installed, which has been shown to maintain the focal-spot quality even at the maximum repetition rate of the laser system of 10 Hz. Furthermore, correlations of the experimental parameters and the produced electron beams have exposed a high influence of the plasma density on the electron-beam parameters, such as charge. A stabilisation of the plasma density e.g.

by the use of continuous-flow gas targets could therefore help to improve the beams even further. The test has also shown that new methods of data storage, live analysis of camera images and potentially trigger systems similar to those in particle physics detectors are required when operating LPA experiments at high repetition rates on a daily basis, as this test resulted in a total of 200 GB of data while saving only a small fraction of the total dataset.

Furthermore, the stable electron source was used to develop a new diagnostic method based on Thomson scattering. The method enables a non-invasive measurement of the electron-bunch energy. Using this technique, the peak energy of the electron bunch was accurately reconstructed. By shifting the overlap position of the electron bunch and laser into the wakefield, it was possible to measure the electron-energy evolution over a distance of 400 µm. The measured energy increase from 35 MeV to 61 MeV shows excellent agreement with PIC simulations of the acceleration process, demonstrating the first in-situ measurement of electron parameters in the wakefield. The measurement was further used to study the dephasing of the electron bunch in the process, showing the importance of the evolution of the laser strength parameter for dephasing.

In the future, in-situ measurements based on Thomson scattering could be expanded to other electron parameters such as divergence or emittance, which have been previously measured using Thomson scattering. This way it could be possible to obtain a full picture of the electron bunch during the acceleration and experimentally study issues of plasma wakefield acceleration such as dephasing, hosing or emittance growth. The studies presented here could therefore help to increase the quality of electron bunches from plasma accelerators and use the advanced acceleration gradients achievable with plasma-based acceleration in medical and industrial applications.

Appendix A

Tritium cross-calibration

The phosphor screens used as profile screen and in the electron spectrometer were absolutely calibrated using the ELBE accelerator at the Helmholtz-Zentrum Dresden-Rossendorf (HZDR) [132, 133]. In this calibration, the amount of photons emitted per solid angle and charge of different screen types was measured. To apply this calibration, it is necessary to calculate the collection efficiency of the imaging system, which can be rather complex, especially if many optics are involved. Therefore, the imaging system used in this measurement campaign was also calibrated against a constant light source, in this case a small phosphorescence tritium source. The constant light source can be used for cross-calibration of other imaging systems to enable a direct application of the absolute screen calibration without knowledge of the efficiency of the imaging system. Another advantage of this method is that uncertainties of the calibration arising from the imaging system are not transferred to the cross-calibrated system as the same imaging systems are used for the calibration of the phosphor screen and the light source. The process of a cross-calibration of constant light sources and the application of the absolute calibration of the screens using tritium sources is described in this chapter.

A.1 Cross-calibration of tritium sources

Tritium (^{3}H) is a radioactive isotope of hydrogen consisting of a proton and two neutrons. The isotope is not stable and decays via beta decay into ^{3}He under emission of an electron and a neutrino. The half-life τ of tritium is 12.32 years [202]. In combination with a phosphor material, the emitted electrons cause phosphorescence. This process is analogous to the working principle of phosphor screens described in Sec. 3.2. Due to the small size and half-life of more than ten years, tritium sources are suitable candidates for the cross-calibration of imaging systems.

In the context of this work, the tritium source used for the calibration campaign (here called HZDR) was calibrated against five tritium sources of the FLASHForward project (called HH_{S1} to HH_{S5}) to enable the application of the results of the absolute calibration to phosphor screens used in the FLASHForward project. For the cross-calibration, all sources were imaged in a light-shielded box with exposure times of 0.0 s to 1.0 s. At every exposure setting, 100 images were taken. A comparison of the average, background subtracted

counts with the standard deviation errors of the 100 shots at each exposure setting is depicted in Fig. A.1. In addition, a linear fit of the form countsHH = $a*$ countsHZDR was applied to each of the sources HH_{S1} to HH_{S5}. The fit results are summarised together with the 1 sigma error bounds of the fit in Tab. A.1. As all measurements were done within a few hours, the influence of the decay of tritium is negligible for these measurements due to the half-life of several years and was not included. However, the half-life of the tritium source has to be included when using one of the sources for a cross-calibration of the imaging systems and a correction factor of $2^{-t/\tau}$ needs to be included, where t is the time passed since the date of the calibration campaign, which is the 5^{th} of November 2016.

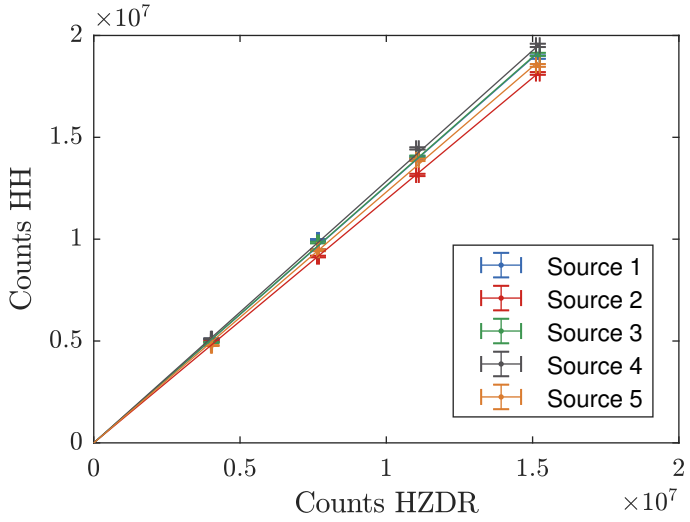

Figure A.1: Cross-calibration of the tritium sources of HZDR and FLASHForward

.

Source	fit result	fit error
HH_{S1}	1.260	0.012
HH_{S2}	1.195	0.006
HH_{S3}	1.263	0.008
HH_{S4}	1.284	0.015
HH_{S5}	1.231	0.012

Table A.1: Calibration factors with standard deviation errors from the cross-calibration of tritium sources

A.2 Absolute calibration of the profile screen

In a next step, the cross-calibration was used to apply the absolute calibration of the DRZ-High screen to the imaging system of the profile screen in the BOND lab. In the calibration at HZDR, DRZ-High resulted in a count rate of $(1.35 \pm 0.13) \times 10^7$ counts/pC for the used imaging system. Imaging of the tritium source HZDR with the same system resulted in $(1.56 \pm 0.02) \times 10^7$ counts/s [132, 133]. These values can be used to apply

the absolute charge calibration to the profile screen using the cross-calibrated tritium sources as described above. For the cross-calibration of the imaging system in the BOND lab, the source HH_{S1} was used. The source was imaged with eleven different exposure times from 0.01 s to 1 s. A linear fit of the camera counts shown in Fig. A.2a resulted in a count rate of the imaging system of $(1.46 \pm 0.01) \times 10^6$ counts/s. An image of the tritium source on the profile screen is depicted in Fig. A.2b. The cross-calibration of the imaging system was done at the 11th of October, 2018, which is 705 days after the initial calibration of the screens at HZDR. Consequently, the count rate of the imaging system has to be corrected for the decay of the tritium by a factor of $2^{-705/4499}$ [202], resulting in $(1.56 \pm 0.01) \times 10^6$ counts/s.

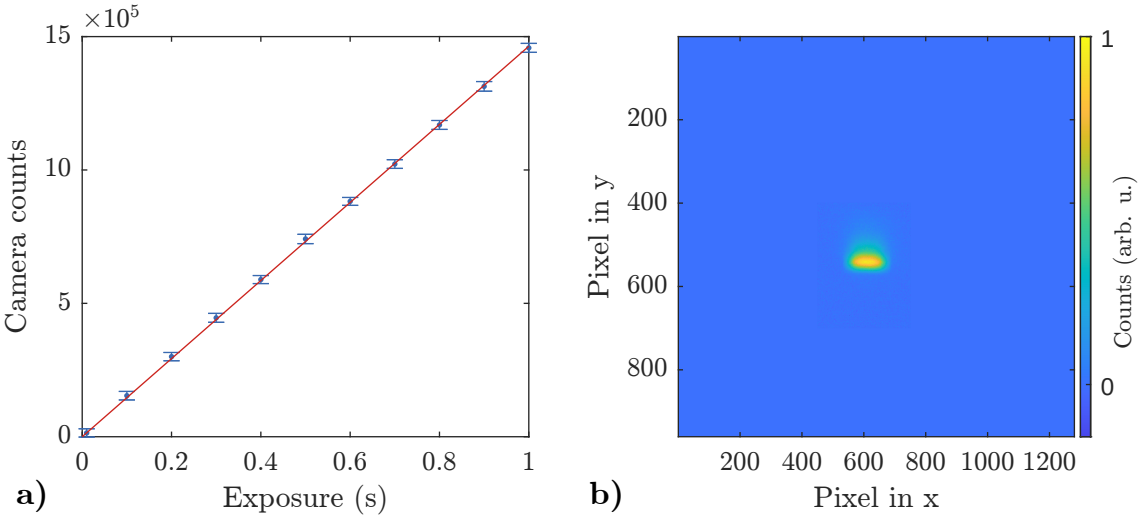

Figure A.2: (a) Result of the calibration of the imaging system of the profile screen using a tritium source attached to the screen. A linear interpolation was applied to the measurement with different exposure times of the camera. (b) Image of the tritium source on the profile screen

.

To apply the calibration it is also important to consider the geometry of the screens in both setups. At HZDR, the screen had an angle of 22 degrees with respect to the electron axis, therefore increasing the active layer of the screen by $1/\cos(22)$, while the imaging axis was perpendicular to the screen axis. In the BOND lab, the screen is rotated at an angle of 45 degrees, and imaged from the top under an angle of 45 degrees with respect to the back surface of the phosphor screen. As the phosphor screens can be considered Lambertian emitters [126, 127], the correction factors from the increased width due to the rotation $(1/\cos(45))$ and from the decrease in intensity due to the imaging angle $(\cos(45))$ cancel out. Consequently, only the screen angle in the HZDR experiment has to be considered.

Combining all values stated above, the amount of photons collected by the imaging system in the BOND lab per electron beam charge can be calculated as:

$$\begin{aligned} C_{BOND} &= C_{HZDR} \cdot \cos(22) \frac{I_{HH}/2^{-t/\tau}}{I_{HZDR}} \frac{1}{cc_{HZDR,HH_{S1}}} \\ &= (1.35 \pm 0.13) \times 10^7 \,\text{counts/pC} \cdot \cos(22) \frac{(1.56 \pm 0.01) \times 10^6 \,\text{counts/s}}{(1.56 \pm 0.02) \times 10^7 \,\text{counts/s}} \frac{1}{1.26 \pm 0.01} \\ &= (9.9 \pm 1.2) \times 10^5 \,\text{counts/pC}. \end{aligned} \tag{A.1}$$

Appendix B

Comparison of charge diagnostics

Using the electron beams described in Chapter 4, three absolutely calibrated charge diagnostics were compared for their use in plasma wakefield acceleration. In this chapter, the results of a comparison campaign of the three diagnostics are discussed.

The charge diagnostics used in this work are a DRZ-type phosphor screen, an integrating current transformer (ICT, also called toroid) and a cavity based charge monitor (DaMon). While phosphor screens and ICTs are used in many LPA setups, this is the first plasma accelerator setup that uses the cavity-based DaMon to measure charges. In addition, the DRZ screen offers higher light yield compared to other types of phosphor screens used in previous LPA experiments which is beneficial for electron beams with a low charge density. The basic principles of the charge diagnostics are explained in Sec. 3.2.

B.1 Previous charge measurements in the BOND lab

Some preliminary tests of the three diagnostics were already done in previous theses [112, 148]. However, several problems with the early setup hindered an accurate comparison of the three diagnostics. First, the measurements were done without an absolute calibration of the imaging of the DRZ screens, such that the charge measured by the two absolutely calibrated diagnostics DaMon and ICT could only be compared to the amount of counts measured by the profile screen, which only resembles a relative charge measurement. In addition, the profile screen was installed in front of the two non-invasive diagnostics, resulting in the broadening of the electron before it could be measured by DaMon and ICT. Lastly, the DaMon with the smallest aperture of the three diagnostics was installed last in the chain, which made it impossible to guarantee that all three diagnostics measured the same parts of the bunches, especially after the electron bunch size has been expanded from travelling through the DRZ screen. This is depicted in Fig. B.1, where a sketch of the configuration of the charge diagnostics during early experiments is shown.

The influence of the DRZ screen on the measurement of the non-invasive diagnostics can be seen in a comparison of the charge measured with the DaMon in this configuration. In Fig. B.2, charge measurements using the DaMon are shown for electron beams where the profile screen is either in front of the DRZ screen or out of the beamline. In this experiment,

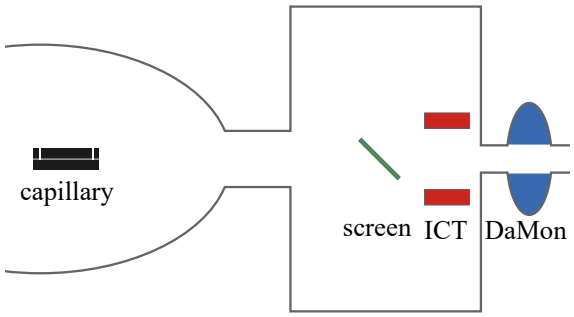

Figure B.1: Sketch of the charge diagnostics for early experiments.

density scans were performed to find suitable parameters for ionisation injection using the sapphire capillary target.

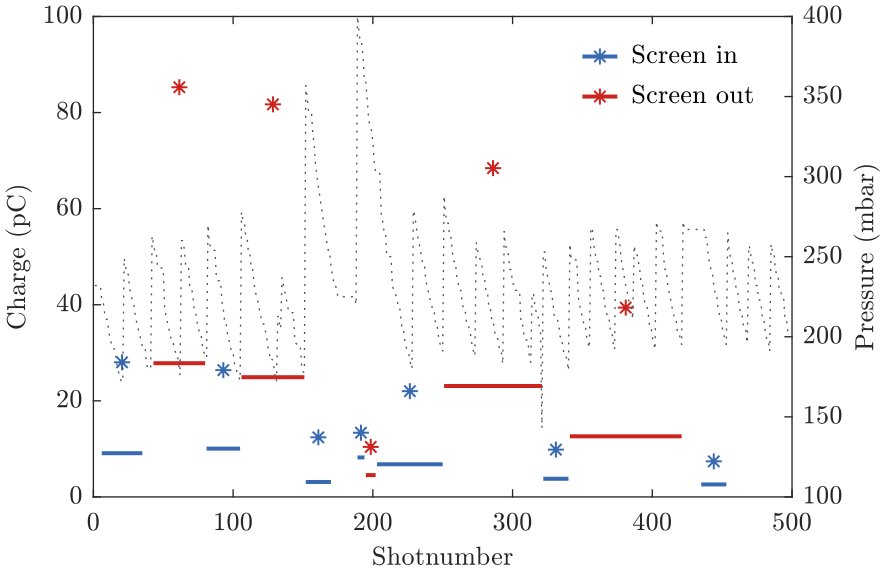

Figure B.2: Comparison of DaMon measurements with and without the profile screen in front of the DaMon. In the run depicted here, ionisation injection with different pressures was tested using a sapphire capillary. During the measurement, the screen position was changed several times. The average charge for consecutive shots with the same screen position is shown here as solid lines. For each block, the maximum charge of that block is depicted as an asterisk. Only blocks with 5 or more consecutive shots in the same screen position are shown. The backing pressure of the sapphire capillary is depicted as grey dotted line.

While the acceleration is far from stable (the gas reservoir for the capillary was filled and shot empty several times, thereby changing the plasma density at every shot), both average charge (bars) and maximum charge (asterisks) of consecutive shots where the profile screen was either in or out show a significant difference. At the same time, the pressure shown as grey dotted line has a similar development for neighbouring sets of shots, making it unlikely that the difference in the measured charge is originating from differences in the plasma parameters. Overall, the average charge of the 182 electron

beams, where the profile screen was in front of the DaMon resulted in 6.1 pC with the highest measured charge being 29.3 pC. During the 289 electron beams without the profile screen, the average charge was almost three times as high, resulting in 18.2 pC, with the highest charge reaching 85.3 pC. In total, more than 25% of all electron beams without the profile screen resulted in higher charge values than the maximum charge measured with the profile screen, demonstrating the influence of the screen on the charge measurement.

Despite these problems of the setup, it was possible to show that the DaMon enables a measurement of electron beams with a high dynamic range [148]. An example is shown in in Fig. B.3, where the charge measured using the DaMon is compared to the counts detected on the profile screen and the charge measurements using the ICT. As changes to the imaging of the profile screen were made prior to the cross calibration using tritium sources, the absolute calibration of the screens can not be applied to this data.

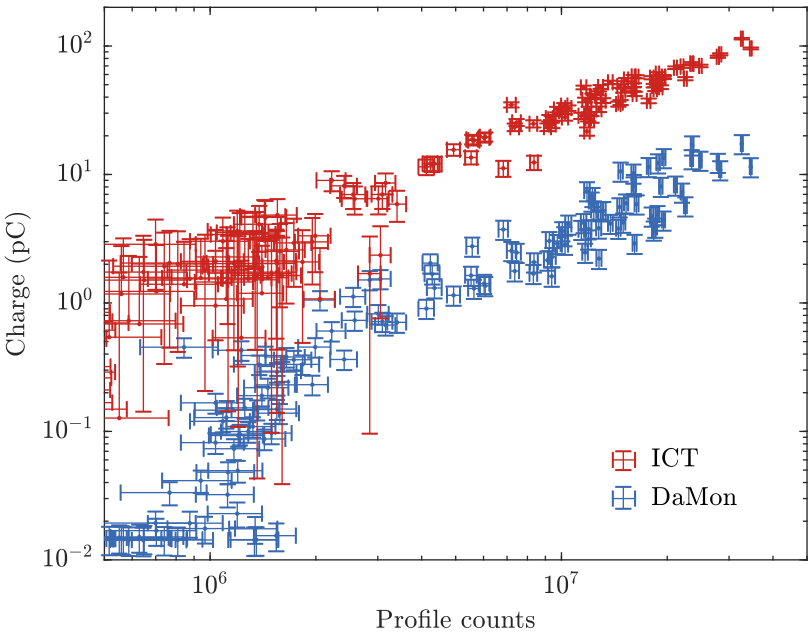

Figure B.3: Comparison of of the measured charge using the DaMon and the ICT as a function of counts on the profile screen. The errors shown here represent the standard deviation of the shots where no electrons were accelerated, defined as less than 1×10^6 counts on the profile screen and less than 20 fC measured using the DaMon. For the DaMon a systematical error of 17% was added [134].

In the figure, the capability of the DaMon to detect charges of tens of femtocoulombs is visible. Both profile screen and ICT are not able to resolve charges this low due to noise. In addition, a discrepancy between the charge measured using the ICT and the DaMon can be seen. The charge measured using the ICT is higher by approximately a factor of four. Such a behaviour has been seen in other LPA experiments and an overestimation of the charge by the ICT of factors between 3 and 10 have been reported [26, 135]. However, also the influence of the DRZ screen on the measurement could be a reason for this factor,

as explained above. As the aperture of the DaMon of 37 mm is less than half the diameter of the ICT, which is 82 mm and the DaMon is placed further behind the profile screen, the difference in the measurements could also originate from the order of the diagnostics in the setup.

B.2 Change of the order of the charge diagnostics

To enable a precise measurement of the electron charge, several changes have been made to the setup in the context of this thesis. First of all, the order of the three diagnostics was changed, such that the two non-invasive diagnostics, DaMon and ICT, are placed in front of the profile screen. To guarantee that the beams in all three diagnostics are the same and no part of an electron beam is e.g. absorbed from the beam pipe between the DaMon and the ICT, a copper collimator with an aperture of 20 mm was installed in front of the DaMon. A sketch of the changed setup and the resulting order of the diagnostics is depicted in Fig. B.4. Furthermore, the absolute calibration of the DRZ screen using the ELBE accelerator at HZDR [132, 133] was applied to the profile screen as described in Sec. A.2.

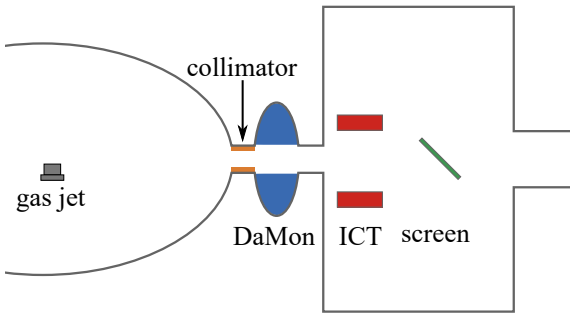

Figure B.4: Sketch of the changed order of the charge diagnostics. The order was changed such that the diagnostic with the smallest aperture (DaMon) is the first diagnostic. The invasive profile screen was positioned at the end.

B.3 Comparison of charge diagnostics in the BOND lab

Using the enhanced setup and the absolutely calibrated profile screen, all three absolutely calibrated charge diagnostics could be compared and the DaMon, which is not used at other plasma experiments could be investigated towards its use in plasma accelerators.

As described in Sec. 3.2.2, the DaMon uses two antennae to achieve a high dynamic range of up to seven orders of magnitude. As this exceeds the dynamic range expected from the LPA experiments, the two channels, here called DaMon Signal and DaMon Charge, were partly overlapped such that both channels were able to measures charges from 1 pC to 40 pC. The DaMon Signal channel is able to detect charges from 50 fC up to 40 pC. The Charge channel has a working region between 0.5 pC and a few hundred pC. In a first

step, the charge measurement of these two channels was compared in order to define areas in which the two channels can be used. A comparison of the charge measurements of the two DaMon channels is depicted in Fig. B.5. In the region between 1 pC and 20 pC, very good agreement of the two channels can be seen. The low charges from 50 fC to 500 fC can only be resolved from the DaMon Signal channel as can be seen in the inset of the image. Starting from 20 pC, the charge measured by the Signal channel deviates from the results of the Charge channel, until the channel saturates at approximately 40 pC (50 pC according to the Charge channel). From comparison to the profile screen, it becomes clear that the measurement of the Signal channel becomes inaccurate as will be shown later. Therefore, The DaMon Signal channel is used for charges below 1 pC in the following, while the DaMon Charge channel is used for charges above 1 pC.

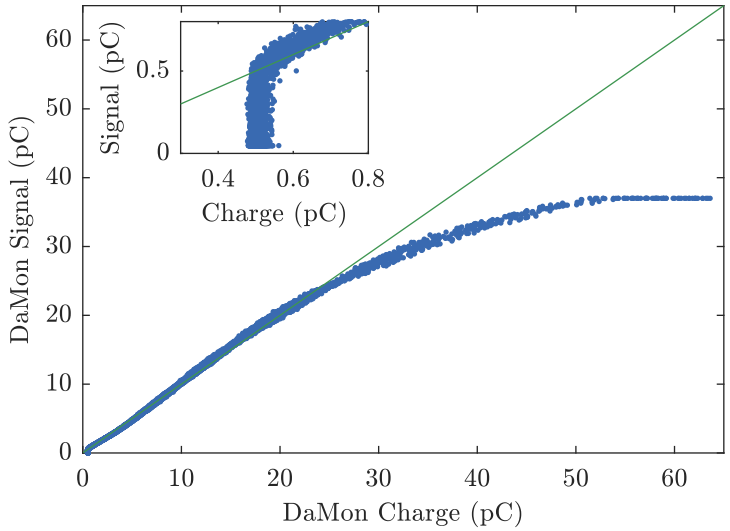

Figure B.5: Comparison of the charge measurement of the two DaMon channels. Unity is shown as green line. In the inset in the top left corner, the charge measurements below 0.8 pC are shown in more detail.

In a next step, all three charge diagnostics are compared, which is depicted in Fig. B.6 in a linear scale (a) and a logarithmic scale (b). Similar as in Fig. B.3, differences in the measured charges between ICT and DaMon are visible, which seems to approach a factor of two for high charges. Over the entire charge range covered, the charge measured by the DaMon is roughly half of the charge measured by the calibrated profile screen, which is resembled by the dotted green line in both scales. For high charges, above 100 pC, the measurement of ICT and profile screen seems to agree quite well, but the ICT massively overestimates low charges. Again, only the DaMon seems to be able to detect low charges of tens of femtocoulombs.

Overall, the charge measured using the DaMon seems to have a more linear correlation to the charge measured on the profile screen than the ICT has, which is especially visible in the logarithmic scale of Fig. B.3. This might be explained by noise from electromagnetic pulses (EMP) that is picked up by the ICT.

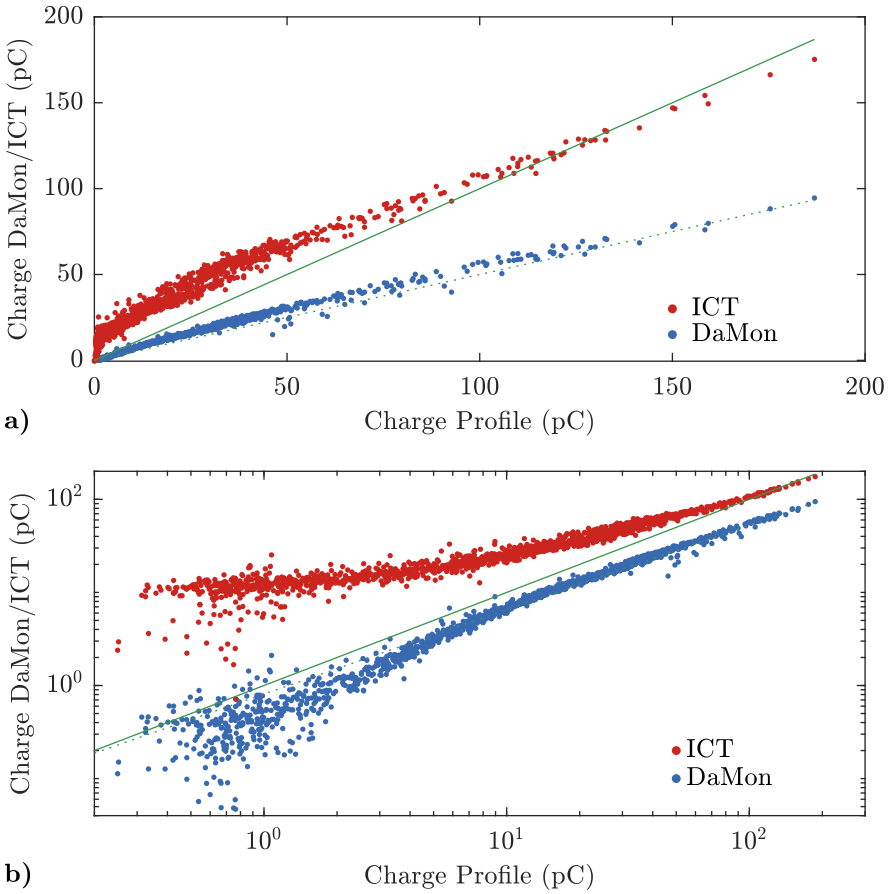

Figure B.6: Comparison of the charge measured by DaMon and ICT to the charge measured by the profile screen in linear scale (a) and logarithmic scale (b). The green (dotted) line indicates a ratio of 1 (0.5). Due to the amount of more than 5000 data points in this plot, no error bars are shown.

To investigate this phenomenon, the charges detected from the three diagnostics were compared while slowly increasing the laser power. This way, the possible influence of plasma EMP and in the case of the profile screen, plasma and laser light on the measured charges can be studied. In order to increase the sensitivity of the profile screen, the ND1 filter in front of the profile screen camera was removed for this measurement. Consequently, the charges detected by the profile screen were scaled by a factor of 10. Results of this test are depicted in Fig. B.7.

The comparison of the three diagnostics in Fig. B.7a is clearly dominated by the noise of the ICT signal, which has a standard deviation of about 1 pC for the first fifty shots where the laser was turned off, compared to 88 fC of the profile screen and even less than 1 fC for the DaMon. In order to visualize the low fluctuations of profile screen and DaMon, they are shown in more detail in Fig. B.7b without the ICT. Here, it becomes also visible that the background level of the profile screen measurement increases when the laser energy is increased, which is probably due to laser or plasma light reaching the camera. The ability of the DaMon to detect very low charges of tens of femtocoulombs is

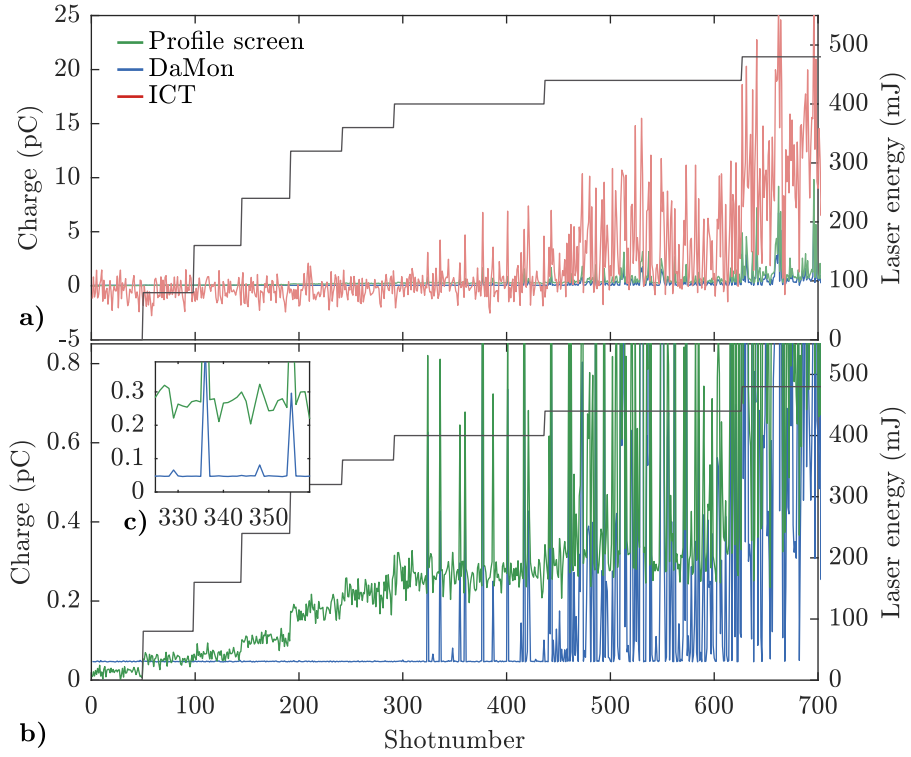

Figure B.7: (a) Comparison of charges measured by ICT, DaMon and profile screen at low laser energies. The laser energy for the shots is shown as grey line. (b) Zoom of the charges measured by profile screen and DaMon. (c) Zoom of the charges measured by profile screen and DaMon for shotnumbers 325 to 360.

also visible in this test. In the inset in Fig. B.7c, a comparison of the charge measured by DaMon and profile screen for shot numbers 325 to 360 is shown. Here, charges of a few hundred femtocoulombs are detected by both diagnostics and are clearly visible as peaks. In the case of the DaMon however, there are two more small spikes above the noise level of 50 fC, showing measured charges of 66 fC and 81 fC. These two peaks are not visible in the noise of the profile screen counts.

The tests of the noise show the advantage of the DaMon as the device is not influenced by EMP noise such as the ICT or additional radiation from laser light, plasma light or X-rays such as the profile screen. The advantage of the DaMon compared to the other non-invasive diagnostic ICT in an inherently noisy environment from a plasma accelerator is even more obvious when comparing the diagnostics during the use of an active plasma lens (APL). This can be seen when looking at Fig. B.8. There is almost no difference in the ADC trace for an electron beam without the APL firing and with the APL firing as is depicted in Fig. B.8b. In case of the ICT, a lot of noise is picked up, which is visible in Fig. B.8d. Compared to the ADC trace of the ICT measurement without the APL which is depicted in Fig. B.8c, the amplitude of the noise is almost two orders of magnitude higher, thus entirely overlaying the trace without the APL such that the peak that is visible in Fig. B.8c can no longer be seen in the comparison in Fig. B.8d.

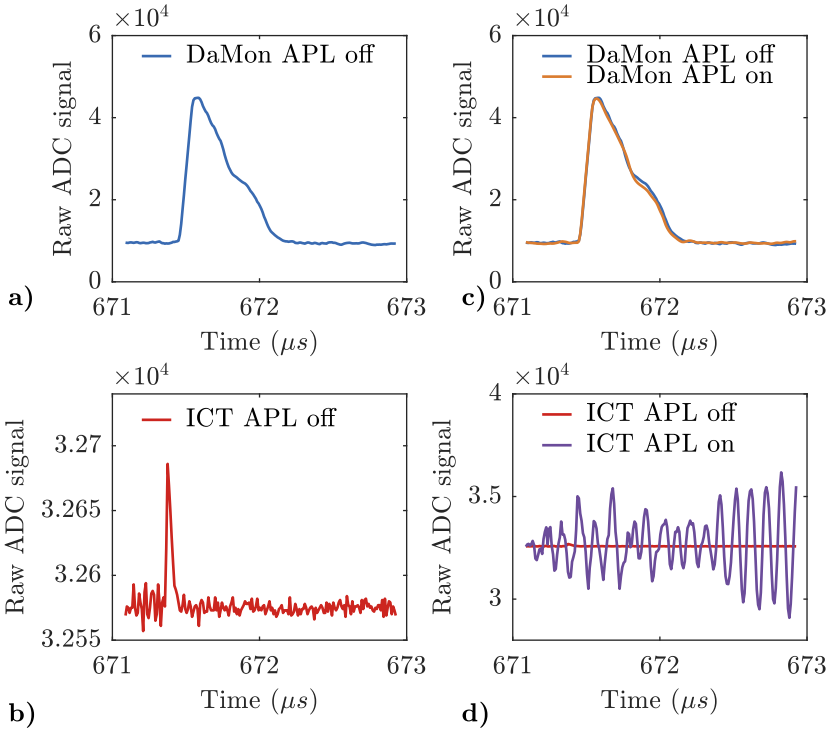

Figure B.8: ADC traces of DaMon and ICT with and without an APL.

In summary, the DaMon seems to enable the non-invasive detection of electron bunches from plasma acceleration with charges from tens of femtocoulombs up to hundreds of picocoulombs. It is insensitive to EMP noise as the tests using low laser intensities and an APL have shown. Compared to the charge measured using the calibrated profile screen, there seems to be a deviation of a factor of two. The source of this deviation is not known, but the agreement of ICT and profile screen for high charges could indicate that the DaMon underestimates the charges. A recalibration of the DaMon or the comparison to an additional diagnostic e.g. an activation based measurement [203] should solve this issue as the correlation between DaMon and profile screen is linear. The ICT is heavily influenced by EMP noise, and is therefore only partially usable in plasma acceleration setups. Especially for low electron bunch charges, no reliable measurement is possible. These findings agree well with previous tests of ICTs in plasma acceleration [26, 135]. A possible solution could be to increase the distance between the plasma target and the ICT. In other experiments, this has enabled a precise measurement of the electron bunch charge using an ICT [203].

Appendix C

The FLASHForward experiment

FLASHForward [40, 41] is designed for precision PWFA research. It uses the superconducting radio frequency (SRF) accelerator FLASH [204, 205], which can deliver high quality, low-emittance electron bunches with an energy of up to 1250 MeV. An overview of the experiment can be seen in Fig. C.1.

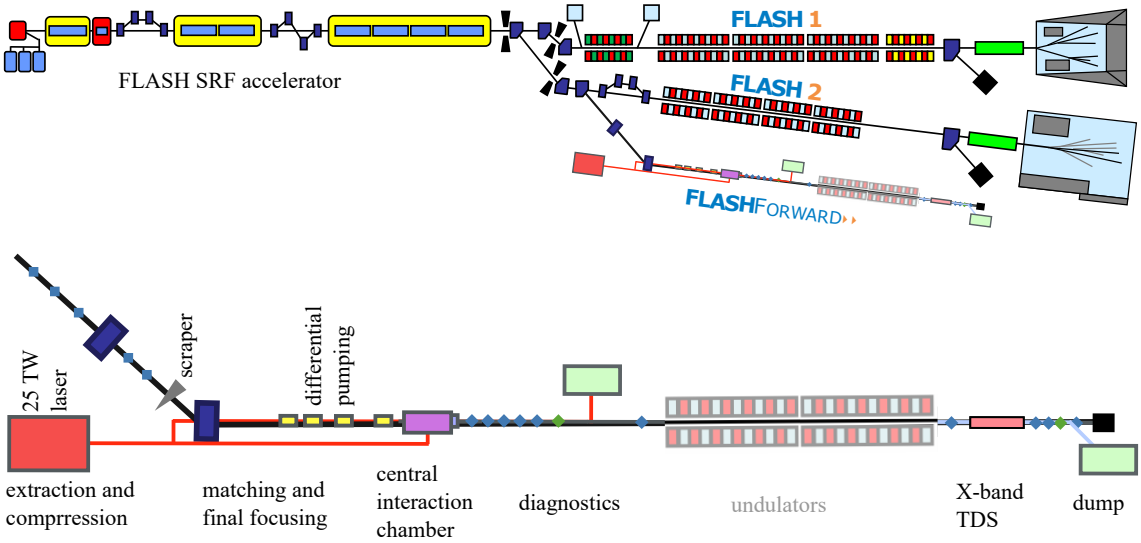

Figure C.1: Overview of the FLASH accelerator with the FLASHForward experiment as third beamline. A more detailed version of the FLASHForward beamline is shown in the bottom part of the image [41].

The FLASHForward experiment can be divided into seven sections. The first section is the extraction and compression from the FLASH1 and FLASH2 FEL beamlines. In addition, a scraper [206] enables to split the FLASH electron beam into driver and witness bunches at this stage. Afterwards, the beam is matched and focused to the central interaction chamber. The differential pumping in this part enables a windowless transport of the electron beam to the experiment. In the central interaction chamber, the plasma targets as well as transition radiation and scintillating screens are located. Furthermore, the SPECTRE laser with a power of up to 25 TW which will be described in more detail in the following section can be longitudinally and transversely coupled into the chamber. The fourth section is used for diagnostics and consists of quadrupoles to capture the electron beam and a dipole magnet to act as a long range electron spectrometer. The installation

of undulator modules remains contingent on the successes of the core FLASHForward experiments. The X-band transverse deflecting structure in section six was commissioned in 2019 and enables longitudinal analysis of driver and witness bunches at fs-scales. The last section of the setup is the beam dump.

FLASHForward has three major scientific goals which are X-1: generation of high brightness beams from internal injection, X-2: demonstration of acceleration at preservation of FEL beam quality and X-3: high-average-power studies. The X-1 experiment will investigate different techniques proposed to produce internal injection beams, which are expected to have high brightness [207–211]. The first successful generation of such a bunch was done in 2019 [87] by local ionisation of using the 25 TW laser to create a density down-ramp to inject the electrons [211]. The X-2 experiment uses the scraper to create driver and witness electron bunch pairs. The experiment enabled the mapping of the wakefield, as well as showing energy doubling, driver depletion and acceleration of electron beams while decreasing the energy spread [85, 212]. X-3 aims to study plasma effects at high repetition rates. The MHz micro pulse structure of the FLASH beam enables these studies at FLASHForward.

In addition to these major experimental goals, FLASHForward has several ancillary projects that are closely linked to the main experiments or a result of the progress made in these experiments. These include the study of the hosing instability [197], development and improvement of active plasma lenses (APL) [120, 213] and transformer ratio optimisation [214]. A plasma-based energy dechirper was already successfully shown at FLASHForward in 2019 [84].

The laser laboratory housing the SPECTRE laser system and a dedicated laboratory for studies related to FLASHForward, the BOND lab, are located on top of the FLASH accelerator hall. A layout of the laboratories is shown in Fig. 3.1. The BOND lab offers a setup to characterise the plasma targets that are used in the central interaction chamber via different diagnostic techniques [86, 215, 216]. In addition, the BOND laboratory houses an LPA setup to develop new diagnostic techniques and investigate new methods of using LPA for medical imaging.

Bibliography

[1] T. Tajima and J. M. Dawson. "Laser electron accelerator". In: *Physical Review Letters* 43.4 (1979), pp. 267–270. ISSN: 00319007. DOI: 10.1103/PhysRevLett.43.267.

[2] Félicie Albert and Alec G R Thomas. "Applications of laser wakefield accelerator-based light sources". In: *Plasma Physics and Controlled Fusion* 58.10 (2016), p. 103001. ISSN: 0741-3335. DOI: 10.1088/0741-3335/58/10/103001.

[3] Simon Bohlen et al. "Long-duration stability studies of laser-wakefield acceleration for applications". In preparation.

[4] Andreas R. Maier et al. "Decoding Sources of Energy Variability in a Laser-Plasma Accelerator". In: *Physical Review X* 10.3 (2020), p. 031039. ISSN: 2160-3308. DOI: 10.1103/PhysRevX.10.031039.

[5] Florian Grüner et al. "Localising functionalised gold-nanoparticles in murine spinal cords by X-ray fluorescence imaging and background-reduction through spatial filtering for human-sized objects". In: *Scientific Reports* 8.1 (2018), p. 16561. ISSN: 2045-2322. DOI: 10.1038/s41598-018-34925-3.

[6] Theresa Staufer et al. "Development of a laser-wakefield Thomson x-ray source for x-ray fluorescence imaging". In: SPIE-Intl Soc Optical Eng, 2019, p. 21. ISBN: 9781510627406. DOI: 10.1117/12.2520685.

[7] Theresa Staufer. "X-Ray Fluorescence Imaging with a Laser-Driven X-Ray Source". PhD thesis. Univerity of Hamburg, 2020.

[8] C. Kamperidis et al. "Low energy spread electron beams from ionization injection in a weakly relativistic laser wakefield accelerator". In: *Plasma Physics and Controlled Fusion* 56.8 (2014), p. 084007. ISSN: 13616587. DOI: 10.1088/0741-3335/56/8/084007.

[9] J. J. Thomson. "Conductivity of Electricity through Gases". In: *(Cambridge University Press)* (1906).

[10] A. Jochmann et al. "High Resolution Energy-Angle Correlation Measurement of Hard X Rays from Laser-Thomson Backscattering". In: *Physical Review Letters* 111.11 (2013), p. 114803. ISSN: 0031-9007. DOI: 10.1103/PhysRevLett.111.114803.

[11] K. Chouffani et al. “Determination of electron beam parameters by means of laser-Compton scattering”. In: *Physical Review Special Topics - Accelerators and Beams* 9.5 (2006), p. 050701. ISSN: 1098-4402. DOI: 10.1103/PhysRevSTAB.9.050701.

[12] G. Golovin et al. “Intrinsic beam emittance of laser-accelerated electrons measured by x-ray spectroscopic imaging”. In: *Scientific Reports* 6.1 (2016), p. 24622. ISSN: 2045-2322. DOI: 10.1038/srep24622.

[13] Raghavan Jayakumar. *Particle Accelerators, Colliders, and the Story of High Energy Physics*. Springer Berlin Heidelberg, 2012. DOI: 10.1007/978-3-642-22064-7.

[14] W. C. Rontgen. “Ueber eine neue Art von Strahlen”. In: *Sitzungsberichte der Physikalisch-Medizinischen Gesellschaft zu Würzburg* (1895), p. 132. ISSN: 00033804. DOI: 10.1002/andp.18983000103.

[15] J. J. Thomson. “ XL. Cathode Rays ”. In: *The London, Edinburgh, and Dublin Philosophical Magazine and Journal of Science* 44.269 (1897), pp. 293–316. ISSN: 1941-5982. DOI: 10.1080/14786449708621070.

[16] K Wille. *The Physics of Particle Accelerators: An Introduction*. Oxford University Press, 2000. ISBN: 9780198505495.

[17] Donna Strickland and Gerard Mourou. “Compression of amplified chirped optical pulses”. In: *Optics Communications* 55.6 (1985), pp. 447–449. ISSN: 00304018. DOI: 10.1016/0030-4018(85)90151-8.

[18] C. G. R. Geddes et al. “High-quality electron beams from a laser wakefield accelerator using plasma-channel guiding”. In: *Nature* 431.7008 (2004), pp. 538–541. ISSN: 0028-0836. DOI: 10.1038/nature02900.

[19] S. P. D. Mangles et al. “Monoenergetic beams of relativistic electrons from intense laser–plasma interactions”. In: *Nature* 431.7008 (2004), pp. 535–538. ISSN: 0028-0836. DOI: 10.1038/nature02939.

[20] J. Faure et al. “A laser–plasma accelerator producing monoenergetic electron beams”. In: *Nature* 431.7008 (2004), pp. 541–544. ISSN: 0028-0836. DOI: 10.1038/nature02963.

[21] Xiaoming Wang et al. “Quasi-monoenergetic laser-plasma acceleration of electrons to 2 GeV”. In: *Nature Communications* 4.1 (2013), pp. 1–9. ISSN: 20411723. DOI: 10.1038/ncomms2988.

[22] Hyung Taek Kim et al. “Enhancement of electron energy to the multi-gev regime by a dual-stage laser-wakefield accelerator pumped by petawatt laser pulses”. In: *Physical Review Letters* 111.16 (2013), p. 165002. ISSN: 00319007. DOI: 10.1103/PhysRevLett.111.165002.

[23] W. P. Leemans et al. "Multi-GeV Electron Beams from Capillary-Discharge-Guided Subpetawatt Laser Pulses in the Self-Trapping Regime". In: *Physical Review Letters* 113.24 (2014), p. 245002. ISSN: 0031-9007. DOI: 10.1103/PhysRevLett.113.245002.

[24] A. J. Gonsalves et al. "Petawatt Laser Guiding and Electron Beam Acceleration to 8 GeV in a Laser-Heated Capillary Discharge Waveguide". In: *Physical Review Letters* 122.8 (2019), p. 084801. ISSN: 0031-9007. DOI: 10.1103/PhysRevLett.122.084801.

[25] P. Boisseau and L. Grodzins. "Fluorescence tomography using synchrotron radiation at the NSLS". In: *Hyperfine Interactions* 33.1-4 (1987), pp. 283–292. ISSN: 15729540. DOI: 10.1007/BF02394116.

[26] M. C. Downer et al. "Diagnostics for plasma-based electron accelerators". In: *Reviews of Modern Physics* 90.3 (2018), p. 035002. ISSN: 0034-6861. DOI: 10.1103/RevModPhys.90.035002.

[27] F.F.Chen. *Introduction to plasma physics and controlled fusion*. Vol. 53. 1989, p. 160. ISBN: 9788578110796. DOI: 10.1017/CBO9781107415324.004. arXiv: arXiv:1011.1669v3.

[28] Ulrich Stroth. *Plasmaphysik: Phänomene, Grundlagen, Anwendungen*. 2011. ISBN: 9783834816153. DOI: 10.1007/978-3-8348-8326-1.

[29] T Striker, R J Goldston, and P Rutherford. *Plasmaphysik: Eine Einführung*. Vieweg+Teubner Verlag, 1998. ISBN: 9783528068844.

[30] Paul Bolton. *Applications of Laser-Driven Particle Acceleration*. 2018. DOI: 10.1201/9780429445101. URL: https://www.routledge.com/Applications-of-Laser-Driven-Particle-Acceleration/Bolton-Parodi-Schreiber/p/book/9781498766418 (visited on 08/14/2020).

[31] Victor Malka et al. "Principles and applications of compact laser–plasma accelerators". In: *Nature Physics* 4.6 (2008), pp. 447–453. ISSN: 1745-2473. DOI: 10.1038/nphys966.

[32] E. Esarey, C. B. Schroeder, and W. P. Leemans. "Physics of laser-driven plasma-based electron accelerators". In: *Reviews of Modern Physics* 81.3 (2009), pp. 1229–1285. ISSN: 00346861. DOI: 10.1103/RevModPhys.81.1229.

[33] Simon Bohlen. "Detection of Inverse Compton Scattering in Plasma Wakefield Experiments". Masters Thesis. University of Hamburg, 2016. URL: https://bib-pubdb1.desy.de/record/315263.

[34] Jens Osterhoff. "Stable , ultra-relativistic electron beams by laser-wakefield acceleration". PhD thesis. 2009, p. 157.

[35] Jan-patrick Schwinkendorf. "Sapphire capillaries for laser-driven wakefield acceleration in plasma". Masters Thesis. 2012.

[36] John M. Dawson. "Nonlinear electron oscillations in a cold plasma". In: *Physical Review* 113.2 (1959), pp. 383–387. ISSN: 0031899X. DOI: 10.1103/PhysRev.113.383.

[37] A. Pukhov and J. Meyer-ter Vehn. "Laser wake field acceleration: The highly nonlinear broken-wave regime". In: *Applied Physics B: Lasers and Optics* 74.4-5 (2002), pp. 355–361. ISSN: 09462171. DOI: 10.1007/s003400200795.

[38] R D Ruth et al. *A PLASMA WAKE FIELD ACCELERATOR?* Tech. rep. 1985, pp. 171–189.

[39] Pisin Chen and J. M. Dawson. "The plasma wake field accelerator". In: *AIP Conference Proceedings*. Vol. 130. 1. AIP Publishing, 1985, pp. 201–212. DOI: 10.1063/1.35301. URL: http://aip.scitation.org/doi/abs/10.1063/1.35301.

[40] A. Aschikhin et al. "The FLASHForward facility at DESY". In: *Nuclear Instruments and Methods in Physics Research, Section A: Accelerators, Spectrometers, Detectors and Associated Equipment* 806 (2016), pp. 175–183. ISSN: 01689002. DOI: 10.1016/j.nima.2015.10.005.

[41] R. D'Arcy et al. "FLASHForward: Plasma wakefield accelerator science for high-average-power applications". In: *Philosophical Transactions of the Royal Society A: Mathematical, Physical and Engineering Sciences* 377.2151 (2019). ISSN: 1364503X. DOI: 10.1098/rsta.2018.0392. arXiv: 1905.03693.

[42] Remi Lehe et al. "A spectral, quasi-cylindrical and dispersion-free Particle-In-Cell algorithm". In: *Computer Physics Communications* 203 (2016), pp. 66–82. ISSN: 00104655. DOI: 10.1016/j.cpc.2016.02.007. arXiv: 1507.04790.

[43] S. Jalas et al. "Accurate modeling of plasma acceleration with arbitrary order pseudo-spectral particle-in-cell methods". In: *Physics of Plasmas* 24.3 (2017), p. 033115. ISSN: 10897674. DOI: 10.1063/1.4978569. arXiv: 1611.05712.

[44] Remi Lehe et al. "Elimination of numerical Cherenkov instability in flowing-plasma particle-in-cell simulations by using Galilean coordinates". In: *Physical Review E* 94.5 (2016), p. 053305. ISSN: 24700053. DOI: 10.1103/PhysRevE.94.053305. arXiv: 1608.00227.

[45] M. Kirchen et al. "Stable discrete representation of relativistically drifting plasmas". In: *Physics of Plasmas* 23.10 (2016), p. 100704. ISSN: 10897674. DOI: 10.1063/1.4964770.

[46] FBPICcontributors. *FBPIC Overview*. 2020. URL: https://fbpic.github.io/overview/pic{_}algorithm.html (visited on 05/15/2020).

[47] R. Lehe et al. "Numerical growth of emittance in simulations of laser-wakefield acceleration". In: *Physical Review Special Topics - Accelerators and Beams* 16.2 (2013), p. 021301. ISSN: 10984402. DOI: 10.1103/PhysRevSTAB.16.021301.

[48] Brendan B. Godfrey and Jean Luc Vay. "Numerical stability of relativistic beam multidimensional PIC simulations employing the Esirkepov algorithm". In: *Journal of Computational Physics* 248 (2013), pp. 33–46. ISSN: 10902716. DOI: 10.1016/j.jcp.2013.04.006.

[49] Benjamin M. Cowan et al. "Generalized algorithm for control of numerical dispersion in explicit time-domain electromagnetic simulations". In: *Physical Review Special Topics - Accelerators and Beams* 16.4 (2013), p. 041303. ISSN: 10984402. DOI: 10.1103/PhysRevSTAB.16.041303.

[50] J. L. Vay. "Noninvariance of space- and time-scale ranges under a Lorentz transformation and the implications for the study of relativistic interactions". In: *Physical Review Letters* 98.13 (2007), p. 130405. ISSN: 00319007. DOI: 10.1103/PhysRevLett.98.130405.

[51] S. P.D. Mangles et al. "Self-injection threshold in self-guided laser wakefield accelerators". In: *Physical Review Special Topics - Accelerators and Beams* 15.1 (2012), p. 011302. ISSN: 10984402. DOI: 10.1103/PhysRevSTAB.15.011302.

[52] Kristjan Poder. "Characterisation of self-guided laser wakefield accelerators to multi-GeV energies". PhD thesis. Imperial College London, 2016, p. 264. URL: https://spiral.imperial.ac.uk/handle/10044/1/56216.

[53] A. Modena et al. "Electron acceleration from the breaking of relativistic plasma waves". In: *Nature* 377.6550 (1995), pp. 606–608. ISSN: 00280836. DOI: 10.1038/377606a0.

[54] M. R. Islam et al. "Near-threshold electron injection in the laser-plasma wakefield accelerator leading to femtosecond bunches". In: *New Journal of Physics* 17.9 (2015), p. 093033. ISSN: 13672630. DOI: 10.1088/1367-2630/17/9/093033.

[55] J. Osterhoff et al. "Generation of stable, low-divergence electron beams by laser-wakefield acceleration in a steady-state-flow gas cell". In: *Physical Review Letters* 101.8 (2008), p. 085002. ISSN: 00319007. DOI: 10.1103/PhysRevLett.101.085002.

[56] A. Buck et al. "Shock-front injector for high-quality laser-plasma acceleration". In: *Physical Review Letters* 110.18 (2013), p. 185006. ISSN: 00319007. DOI: 10.1103/PhysRevLett.110.185006.

[57] C. Thaury et al. "Shock assisted ionization injection in laser-plasma accelerators". In: *Scientific Reports* 5.4 (2015), pp. 1–7. ISSN: 20452322. DOI: 10.1038/srep16310.

[58] S. Bulanov et al. "Particle injection into the wave acceleration phase due to nonlinear wake wave breaking". In: *Physical Review E - Statistical Physics, Plasmas, Fluids, and Related Interdisciplinary Topics* 58.5 (1998), R5257–R5260. ISSN: 1063651X. DOI: 10.1103/PhysRevE.58.R5257.

[59] H. Suk et al. "Plasma Electron Trapping and Acceleration in a Plasma Wake Field Using a Density Transition". In: *Physical Review Letters* 86.6 (2001), pp. 1011–1014. ISSN: 0031-9007. DOI: 10.1103/PhysRevLett.86.1011.

[60] Min Chen et al. "Electron injection and trapping in a laser wakefield by field ionization to high-charge states of gases". In: *Journal of Applied Physics* 99.5 (2006), p. 056109. ISSN: 0021-8979. DOI: 10.1063/1.2179194.

[61] E. Oz et al. "Ionization-Induced Electron Trapping in Ultrarelativistic Plasma Wakes". In: *Physical Review Letters* 98.8 (2007), p. 084801. ISSN: 0031-9007. DOI: 10.1103/PhysRevLett.98.084801.

[62] M. Chen et al. "Theory of ionization-induced trapping in laser-plasma accelerators". In: *Physics of Plasmas* 19.3 (2012), p. 033101. ISSN: 1070664X. DOI: 10.1063/1.3689922.

[63] S. Augst et al. "Tunneling ionization of noble gases in a high-intensity laser field". In: *Physical Review Letters* 63.20 (1989), pp. 2212–2215. ISSN: 00319007. DOI: 10.1103/PhysRevLett.63.2212.

[64] Chao Gong et al. "Ion acceleration in a gas jet using multi-terawatt CO2 laser pulses". In: *AIP Conference Proceedings*. Vol. 1507. 1. American Institute of PhysicsAIP, 2012, pp. 791–796. ISBN: 9780735411258. DOI: 10.1063/1.4773799. URL: http://aip.scitation.org/doi/abs/10.1063/1.4773799.

[65] A. Kramida et al. *NIST Atomic Spectra Database (ver. 5.7.1)*. 2019. DOI: 10.18434/T4W30F. URL: http://physics.nist.gov/asd.

[66] A. Pak et al. "Injection and Trapping of Tunnel-Ionized Electrons into Laser-Produced Wakes". In: *Physical Review Letters* 104.2 (2010), p. 025003. ISSN: 0031-9007. DOI: 10.1103/PhysRevLett.104.025003.

[67] C. McGuffey et al. "Ionization Induced Trapping in a Laser Wakefield Accelerator". In: *Physical Review Letters* 104.2 (2010), p. 025004. ISSN: 0031-9007. DOI: 10.1103/PhysRevLett.104.025004.

[68] C. E. Clayton et al. "Self-Guided Laser Wakefield Acceleration beyond 1 GeV Using Ionization-Induced Injection". In: *Physical Review Letters* 105.10 (2010), p. 105003. ISSN: 0031-9007. DOI: 10.1103/PhysRevLett.105.105003.

[69] F. Li et al. "Generating high-brightness electron beams via ionization injection by transverse colliding lasers in a plasma-Wakefield accelerator". In: *Physical Review Letters* 111.1 (2013), p. 015003. ISSN: 00319007. DOI: 10.1103/PhysRevLett.111.015003.

[70] N. Bourgeois, J. Cowley, and S. M. Hooker. "Two-pulse ionization injection into quasilinear laser wakefields". In: *Physical Review Letters* 111.15 (2013), p. 155004. ISSN: 00319007. DOI: 10.1103/PhysRevLett.111.155004.

[71] Ming Zeng et al. "Controlled ionization-induced injection by tailoring the gas-density profile in laser wakefield acceleration". In: *Journal of Plasma Physics* 78.4 (2012), pp. 363–371. ISSN: 00223778. DOI: 10.1017/S0022377812000098.

[72] B. B. Pollock et al. "Demonstration of a narrow energy spread, 0.5GeV electron beam from a two-stage laser wakefield accelerator". In: *Physical Review Letters* 107.4 (2011), p. 045001. ISSN: 00319007. DOI: 10.1103/PhysRevLett.107.045001.

[73] Ming Zeng et al. "Self-truncated ionization injection and consequent monoenergetic electron bunches in laser wakefield acceleration". In: *Physics of Plasmas* 21.3 (2014), p. 030701. ISSN: 1070-664X. DOI: 10.1063/1.4868404.

[74] M. Mirzaie et al. "Demonstration of self-truncated ionization injection for GeV electron beams". In: *Scientific Reports* 5.1 (2015), p. 14659. ISSN: 2045-2322. DOI: 10.1038/srep14659.

[75] J. P. Couperus et al. "Demonstration of a beam loaded nanocoulomb-class laser wakefield accelerator". In: *Nature Communications* 8.1 (2017), p. 487. ISSN: 2041-1723. DOI: 10.1038/s41467-017-00592-7.

[76] A Irman et al. "Improved performance of laser wakefield acceleration by tailored self-truncated ionization injection". In: *Plasma Physics and Controlled Fusion* 60.4 (2018), p. 044015. ISSN: 0741-3335. DOI: 10.1088/1361-6587/aaaef1.

[77] C. D. Decker et al. "The evolution of ultra-intense, short-pulse lasers in underdense plasmas". In: *Physics of Plasmas* 3.5 (1996), pp. 2047–2056. ISSN: 10897674. DOI: 10.1063/1.872001.

[78] W. Lu et al. "Generating multi-GeV electron bunches using single stage laser wakefield acceleration in a 3D nonlinear regime". In: *Physical Review Special Topics - Accelerators and Beams* 10.6 (2007), p. 061301. ISSN: 1098-4402. DOI: 10.1103/PhysRevSTAB.10.061301.

[79] P. Sprangle et al. "Wakefield generation and GeV acceleration in tapered plasma channels". In: *Physical Review E - Statistical, Nonlinear, and Soft Matter Physics* 63.5 II (2001), pp. 564051–5640511. ISSN: 15393755. DOI: 10.1103/PhysRevE.63.056405.

[80] E. Guillaume et al. "Electron Rephasing in a Laser-Wakefield Accelerator". In: *Physical Review Letters* 115.15 (2015), p. 155002. ISSN: 10797114. DOI: 10.1103/PhysRevLett.115.155002.

[81] Alexander Debus et al. "Circumventing the Dephasing and Depletion Limits of Laser-Wakefield Acceleration". In: *Physical Review X* 9.3 (2019), p. 031044. ISSN: 21603308. DOI: 10.1103/PhysRevX.9.031044.

[82] James D Sadler et al. "Overcoming the dephasing limit in multiple-pulse laser wakefield acceleration". In: (2020). DOI: 10.1103/PhysRevAccelBeams.23.021303.

[83] J. P. Palastro et al. "Dephasingless Laser Wakefield Acceleration". In: *Physical Review Letters* 124.13 (2020), p. 134802. ISSN: 10797114. DOI: 10.1103/PhysRevLett.124.134802.

[84] R. D'Arcy et al. "Tunable Plasma-Based Energy Dechirper". In: *Physical Review Letters* 122.3 (2019). ISSN: 10797114. DOI: 10.1103/PhysRevLett.122.034801. arXiv: 1810.06307.

[85] S. Schröder et al. "High-resolution sampling of beam-driven plasma wakefields". In: *Nature Communications* 11.1 (2020). ISSN: 2041-1723. DOI: 10.1038/s41467-020-19811-9.

[86] M. J. Garland et al. "Evolution of longitudinal plasma-density profiles in discharge capillaries for plasma wakefield accelerators". Submitted. 2020.

[87] Alexander Knetsch et al. "Controlled density-downramp injection in a beam-driven plasma wakefield accelerator". In: (2020). arXiv: 2007.12639.

[88] Jean Claude Diels and Wolfgang Rudolph. *Ultrashort Laser Pulse Phenomena*. Elsevier Inc., 2006. ISBN: 9780122154935. DOI: 10.1016/B978-0-12-215493-5.X5000-9.

[89] Martin E. Fermann, Almantas. Galvanauskas, and Gregg. Sucha. *Ultrafast lasers : technology and applications*. Marcel Dekker, 2003, p. 784. ISBN: 9780824708412.

[90] Irl N. Duling. *Compact sources of ultrashort pulses*. Cambridge University Press, 1995, p. 430. ISBN: 9780521461924.

[91] Albert Einstein. "Zur Quantentheorie der Strahlung". In: *Mitteilungen der Physikalischen Gesellschaft Zürich* 18 (1916).

[92] T. H. Maiman. "Stimulated optical radiation in Ruby". In: *Nature* 187.4736 (1960), pp. 493–494. ISSN: 00280836. DOI: 10.1038/187493a0.

[93] *The Nobel Prize in Physics 2018*. 2018. URL: https://www.nobelprize.org/prizes/physics/2018/summary/ (visited on 08/19/2020).

[94] W. Heisenberg. "Über den anschaulichen Inhalt der quantentheoretischen Kinematik und Mechanik". In: *Zeitschrift für Physik* 43.3-4 (1927), pp. 172–198. ISSN: 14346001. DOI: 10.1007/BF01397280.

[95] P. F. Moulton. "Spectroscopic and laser characteristics of Ti:Al_2O_3". In: *Journal of the Optical Society of America B* 3.1 (1986), p. 125. ISSN: 0740-3224. DOI: 10.1364/josab.3.000125.

[96] J. P. Chambaret et al. "Generation of 25-TW, 32-fs pulses at 10 Hz". In: *Optics Letters* 21.23 (1996), p. 1921. ISSN: 0146-9592. DOI: 10.1364/OL.21.001921.

[97] Amplitude. *Pulsar, 10 Hz Femtosecond System*. Tech. rep. 2017.

[98] VENTEON. *PULSE:ONE Oscillator Manual*. Tech. rep. 2014.

[99] D. E. Spence, P. N. Kean, and W. Sibbett. "60-fsec pulse generation from a self-mode-locked Ti:sapphire laser". In: *Optics Letters* 16.1 (1991), p. 42. ISSN: 0146-9592. DOI: 10.1364/OL.16.000042.

[100] Andreas Stingl et al. "Generation of 11-fs pulses from a Ti:sapphire laser without the use of prisms". In: *Optics Letters* 19.3 (1994), p. 204. ISSN: 0146-9592. DOI: 10.1364/ol.19.000204.

[101] A Offner. *Unit Power Imaging Catoptric Anastigmat*. 1973. URL: https://patentimages.storage.googleapis.com/pdfs/US3726323.pdf.

[102] G. Cheriaux et al. "Aberration-free stretcher design for ultrashort-pulse amplification". In: *Optics Letters* 21.6 (1996), p. 414. ISSN: 0146-9592. DOI: 10.1364/ol.21.000414.

[103] Detao Du et al. "Terawatt Ti:sapphire laser with a spherical reflective-optic pulse expander". In: *Optics Letters* 20.20 (1995), p. 2114. ISSN: 0146-9592. DOI: 10.1364/ol.20.002114.

[104] Nikita Khodakovskiy. "Methods of ultra-fast laser contrast diagnostics and optimization". PhD thesis. 2020. DOI: 10.17169/refubium-26448. URL: http://dx.doi.org/10.17169/refubium-26448.

[105] I S Luan et al. *in the UK High dynamic range third-order correlation measurement of picosecond laser pulse shapes*. Tech. rep. 1993, pp. 1426–1429.

[106] Fastlite. "Wizzler manual, V2.0". In: ().

[107] Olle Lundh. *Private communications*. 2018.

[108] T. Oksenhendler et al. "Self-referenced spectral interferometry". In: *Applied Physics B: Lasers and Optics* 99.1-2 (2010), pp. 7–12. ISSN: 09462171. DOI: 10.1007/s00340-010-3916-y.

[109] A. Moulet et al. "Single-shot, high-dynamic-range measurement of sub-15 fs pulses by self-referenced spectral interferometry". In: *Optics Letters* 35.22 (2010), p. 3856. ISSN: 0146-9592. DOI: 10.1364/ol.35.003856.

[110] N. Minkovski et al. "Nonlinear polarization rotation and orthogonal polarization generation experienced in a single-beam configuration". In: *Journal of the Optical Society of America B* 21.9 (2004), p. 1659. ISSN: 0740-3224. DOI: 10.1364/josab.21.001659.

[111] L. Lepetit, G. Chériaux, and M. Joffre. "Linear techniques of phase measurement by femtosecond spectral interferometry for applications in spectroscopy". In: *Journal of the Optical Society of America B* 12.12 (1995), p. 2467. ISSN: 0740-3224. DOI: 10.1364/josab.12.002467.

[112] J.-P. Schwinkendorf. "Electron-beam diagnostics for a laser-driven plasma wakefield accelerator in the framework of FLASHForward". PhD thesis. University of Hamburg, 2018.

[113] Newport. *The Effect of Dispersion on Ultrashort Pulses*. 2020. URL: https://www.newport.com/n/the-effect-of-dispersion-on-ultrashort-pulses (visited on 10/04/2020).

[114] Paul J Wrzesinski et al. "Group-velocity-dispersion measurements of atmospheric and combustion-related gases using an ultrabroadband-laser source". In: (2011). DOI: 10.1002/jrs.2709/abstract.

[115] Jürgen Eichler, Lothar Dünkel, and Bernd Eppich. "Die Strahlqualität von Lasern – Wie bestimmt man Beugungsmaßzahl und Strahldurchmesser in der Praxis?" In: *Laser Technik Journal* 1.2 (2004), pp. 63–66. ISSN: 16137728. DOI: 10.1002/latj.200790019.

[116] D. J. Spence and S. M. Hooker. "Investigation of a hydrogen plasma waveguide". In: *Physical Review E - Statistical, Nonlinear, and Soft Matter Physics* 63.1 II (2001), pp. 1–4. ISSN: 15393755. DOI: 10.1103/PhysRevE.63.015401.

[117] A. Butler, D. J. Spence, and S. M. Hooker. "Guiding of High-Intensity Laser Pulses with a Hydrogen-Filled Capillary Discharge Waveguide". In: *Physical Review Letters* 89.18 (2002), p. 185003. ISSN: 10797114. DOI: 10.1103/PhysRevLett.89.185003.

[118] S. Semushin and V. Malka. "High density gas jet nozzle design for laser target production". In: *Review of Scientific Instruments* 72.7 (2001), pp. 2961–2965. ISSN: 00346748. DOI: 10.1063/1.1380393.

[119] J. Van Tilborg et al. "Active Plasma Lensing for Relativistic Laser-Plasma-Accelerated Electron Beams". In: *Physical Review Letters* 115.18 (2015), p. 184802. ISSN: 10797114. DOI: 10.1103/PhysRevLett.115.184802.

[120] J. H. Röckemann et al. "Direct measurement of focusing fields in active plasma lenses". In: *Physical Review Accelerators and Beams* 21.12 (2018). ISSN: 24699888. DOI: 10.1103/PhysRevAccelBeams.21.122801. arXiv: 1803.06663.

[121] M. Meisel. "Emittance Measurement of Electron Beams from Laser Wakefield Acceleration using an Active Plasma Lens". PhD thesis. University of Hamburg, 2018, p. 91. URL: https://bib-pubdb1.desy.de/record/414292.

[122] T. K Brümmer et al. "Compact all-optical tunable narrowband Compton light source". Submitted. 2020.

[123] D. Lipka et al. "Dark current monitor for the European XFEL". In: *Proceedings of DIPAC2011*. Hamburg, Germany: JACow, 2011, pp. 572–574.

[124] D. Lipka, J. Lund-Nielsen, and M. Seebach. "Resonator for charge measurement at REGEA". In: *Proceedings of IBIC2013*. Oxford, UK: JACow, 2013, pp. 872 –875.

[125] Bergoz. *Integrating Current Transformer, User's Manual, Rev. 4.0*. Tech. rep. 2018.

[126] T. Kurz. "Calibration of scintillation screens in laser wakefield acceleration". PhD thesis. Ludwig Maximilian University Munich, 2016.

[127] Y. Glinec et al. "Absolute calibration for a broad range single shot electron spectrometer". In: *Review of Scientific Instruments* 77.10 (2006), p. 103301. ISSN: 00346748. DOI: 10.1063/1.2360988.

[128] A. Jabłoństski. "Efficiency of anti-stokes fluorescence in dyes". In: *Nature* 131.3319 (1933), pp. 839–840. ISSN: 00280836. DOI: 10.1038/131839b0.

[129] G. G. Stokes. "On the change of refrangibility of light". In: *Philosophical Transactions of the Royal Society of London* 142 (1852), pp. 463–562. ISSN: 0261-0523. DOI: 10.1098/rstl.1852.0022.

[130] Hermann Haken and Hans Christoph Wolf. *Atom- und Quantenphysik*. 1987, p. 534. ISBN: 978-3-642-62142-0. DOI: 10.1007/978-3-642-97025-2.

[131] Friedrich Dierks. *Sensitivity and Image Quality of Digital Cameras*. Tech. rep. 2004.

[132] Thomas Kurz et al. *Calibration and cross-laboratory implementation of scintillating screens for electron bunch charge determination*. 2018. DOI: 10.1063/1.5041755. URL: http://aip.scitation.org/doi/10.1063/1.5041755.

[133] J. P. Schwinkendorf et al. "Charge calibration of DRZ scintillation phosphor screens". In: *Journal of Instrumentation* 14.9 (2019). ISSN: 17480221. DOI: 10.1088/1748-0221/14/09/P09025.

[134] D. Lipka. *Private communications*. 2018.

[135] B. Hidding et al. "Novel method for characterizing relativistic electron beams in a harsh laser-plasma environment". In: *Review of Scientific Instruments* 78.8 (2007), p. 083301. ISSN: 00346748. DOI: 10.1063/1.2775668.

[136] K. Nakamura et al. "Broadband single-shot electron spectrometer for GeV-class laser-plasma-based accelerators". In: *Review of Scientific Instruments* 79.5 (2008), p. 053301. ISSN: 00346748. DOI: 10.1063/1.2929672.

[137] Robert Fearghus Keeble. "Measurement of the electron energy distribution at AWAKE". PhD thesis. University College London, 2020.

[138] J. C. Wood. "Betatron Radiation from Laser Wakefield Accelerators and its Applications". PhD thesis. Imperial College London, 2017, p. 231.

[139] MCIOptonix. *DRZ Screens*. 2020. URL: http://www.mcio.com/Products/drz-screens.aspx (visited on 10/04/2020).

[140] A.-S Müller. "Description of Beam-Matter Interaction in the Covariance Matrix Formalism". In: (2001). ISSN: 2001-0013.

[141] Ralph A Alpher and Donald R White. "Optical Refractivity of High-Temperature Gases. II. Effects Resulting from Ionization of Monatomic Gases". In: *Citation: The Physics of Fluids* 2 (1959), p. 162. DOI: 10.1063/1.1705907.

[142] J. Dyson, R. V. Williams, and K. M. Young. "Interferometric measurement of electron density in Sceptre IV". In: *Nature* 195.4848 (1962), pp. 1291–1292. ISSN: 00280836. DOI: 10.1038/1951291a0.

[143] D. E.T.F. Ashby and D. F. Jephcott. "Measurement of plasma density using a gas laser as an infrared interferometer". In: *Applied Physics Letters* 3.1 (1963), pp. 13–16. ISSN: 00036951. DOI: 10.1063/1.1723556.

[144] J. M. Cole. "Diagnosis and application of laser wakefield accelerators". Dissertation. Imperial College London, 2016. URL: https://spiral.imperial.ac.uk:8443/handle/10044/1/42222.

[145] Paul Pourmoussavi. "Studies on a feedback loop szstem for the optimisation of Laser Wakefield Acceleration". Masters Thesis. University of Hamburg, 2018.

[146] Yannick Ruske. "Präzise spektrale Analyse von Elektronenpaketen aus einem Laser Plasma Wakefield Beschleuniger". Bachelor Thesis. University of Hamburg, 2019.

[147] Simon Bohlen et al. "In-situ measurement of the electron energy evolution in a laser plasma acceleratorusing Thomson scattering". In preparation.

[148] O. Kononenko. "Controlled injection into laser-driven wakefield accelerator". PhD thesis. University of Hamburg, 2018.

[149] T. K Brümmer. "Design Study of a Laser-Driven X-ray Source for Medical Fluorescence Imaging". PhD thesis. University of Hamburg, 2018, p. 171. URL: https://bib-pubdb1.desy.de/record/402600.

[150] Theresa Brümmer et al. "Design study for a compact laser-driven source for medical X-ray fluorescence imaging". In: *Physical Review Accelerators and Beams* 23.3 (2020), p. 031601. ISSN: 24699888. DOI: 10.1103/PhysRevAccelBeams.23.031601.

[151] S. P.D. Mangles et al. "Laser-wakefield acceleration of monoenergetic electron beams in the first plasma-wave period". In: *Physical Review Letters* 96.21 (2006). ISSN: 00319007. DOI: 10.1103/PhysRevLett.96.215001.

[152] J. S. Liu et al. "All-optical cascaded laser wakefield accelerator using ionization-induced injection". In: *Physical Review Letters* 107.3 (2011), p. 035001. ISSN: 00319007. DOI: 10.1103/PhysRevLett.107.035001.

[153] S. Fourmaux et al. "Investigation of the thermally induced laser beam distortion associated with vacuum compressor gratings in high energy and high average power femtosecond laser systems". In: *Optics Express* 17.1 (2009), p. 178. ISSN: 1094-4087. DOI: 10.1364/oe.17.000178.

[154] Vincent Leroux et al. "Wavefront degradation of a 200 TW laser from heat-induced deformation of in-vacuum compressor gratings". In: *2018 Conference on Lasers and Electro-Optics, CLEO 2018 - Proceedings*. Institute of Electrical and Electronics Engineers Inc., 2018. ISBN: 9781943580422. DOI: 10.1364/oe.26.013061.

[155] Jan Lukas Dresselhaus. "Paving the way of high repetition rate laser wakefield acceleration by solving heat induced grating deformation issues". Masters Thesis. University of Hamburg, 2020.

[156] Nasr A.M. Hafz et al. "Stable generation of GeV-class electron beams from self-guided laser-plasma channels". In: *Nature Photonics* 2.9 (2008), pp. 571–577. ISSN: 17494885. DOI: 10.1038/nphoton.2008.155.

[157] S. Banerjee et al. "Stable, tunable, quasimonoenergetic electron beams produced in a laser wakefield near the threshold for self-injection". In: *Physical Review Special Topics - Accelerators and Beams* 16.3 (2013). ISSN: 10984402. DOI: 10.1103/PhysRevSTAB.16.031302.

[158] K. Boháček et al. "Stable electron beams from laser wakefield acceleration with few-terawatt driver using a supersonic air jet". In: *Nuclear Instruments and Methods in Physics Research, Section A: Accelerators, Spectrometers, Detectors and Associated Equipment* 883 (2018), pp. 24–28. ISSN: 01689002. DOI: 10.1016/j.nima.2017.11.022.

[159] Wim Leemans. *KALDERA – High average power laser plasma accelerator project at DESY*. Tech. rep. 4th European Advanced Accelerator Concepts Workshop, 2019. URL: https://agenda.infn.it/event/17304/contributions/97644/.

[160] S. Steinke et al. "Multistage coupling of independent laser-plasma accelerators". In: *Nature* 530.7589 (2016), pp. 190–193. ISSN: 14764687. DOI: 10.1038/nature16525.

[161] Sabine Schindler et al. "Tunable X-ray source by Thomson scattering during laser-wakefield acceleration". In: *Laser Acceleration of Electrons, Protons, and Ions V*. Ed. by Eric Esarey, Carl B. Schroeder, and Jörg Schreiber. Vol. 11037. SPIE, 2019, p. 22. ISBN: 9781510627406. DOI: 10.1117/12.2520354. URL: https://www.spiedigitallibrary.org/conference-proceedings-of-spie/11037/2520354/Tunable-X-ray-source-by-Thomson-scattering-during-laser-wakefield/10.1117/12.2520354.full.

[162] J. M. Krämer et al. "Making spectral shape measurements in inverse Compton scattering a tool for advanced diagnostic applications". In: *Scientific Reports* 8.1 (2018), p. 1398. ISSN: 2045-2322. DOI: 10.1038/s41598-018-19546-0.

[163] Axel Jochmann. "Development and Characterization of a Tunable Ultrafast X-Ray Source Via Inverse-Compton-Scattering". PhD thesis. 2014.

[164] W. J. Brown et al. "Experimental characterization of an ultrafast Thomson scattering x-ray source with three-dimensional time and frequency-domain analysis". In: *Physical Review Special Topics - Accelerators and Beams* 7.6 (2004), pp. 23–34. ISSN: 10984402. DOI: 10.1103/PhysRevSTAB.7.060702.

[165] Hiroaki Utsunomiya et al. "Energy Calibration of the NewSUBARU Storage Ring for Laser Compton-Scattering Gamma Rays and Applications". In: *IEEE Transactions on Nuclear Science* 61.3 (2014), pp. 1252–1258. ISSN: 0018-9499. DOI: 10.1109/TNS.2014.2312323.

[166] K. Khrennikov et al. "Tunable all-optical quasimonochromatic Thomson X-ray source in the nonlinear regime". In: *Physical Review Letters* 114.19 (2015), p. 195003. ISSN: 10797114. DOI: 10.1103/PhysRevLett.114.195003.

[167] N. D. Powers et al. "Quasi-monoenergetic and tunable X-rays from a laser-driven Compton light source". In: *Nature Photonics* 8.January (2014), pp. 28–31. ISSN: 1749-4885. DOI: 10.1038/nphoton.2013.314.

[168] J. Faure et al. "Controlled injection and acceleration of electrons in plasma wakefields by colliding laser pulses". In: *Nature* 444.7120 (2006), pp. 737–739. ISSN: 0028-0836. DOI: 10.1038/nature05393.

[169] K. Poder et al. "Multi-GeV electron acceleration in wakefields strongly driven by oversized laser spots". In: *submitted* (2020).

[170] Y. Ma et al. "Angular streaking of betatron X-rays in a transverse density gradient laser-wakefield accelerator". In: *Physics of Plasmas* 25.11 (2018), p. 113105. ISSN: 1070-664X. DOI: 10.1063/1.5054807.

[171] Paul Scherkl. "High-Quality Radiation from Inverse Compton Scattering using Ultralow-Emittance Electron Bunches". Masters Thesis. 2015, pp. 1–127.

[172] S. G. Rykovanov et al. "Quasi-monoenergetic femtosecond photon sources from Thomson Scattering using laser plasma accelerators and plasma channels". In: (2014). ISSN: 1361-6455. DOI: 10.1088/0953-4075/47/23/234013. arXiv: 1406.1832.

[173] Balsa Terzic et al. "Narrow-band emission in Thomson sources operating in the high-field regime". In: *Physical Review Letters* 112.7 (2014), pp. 1–5. ISSN: 00319007. DOI: 10.1103/PhysRevLett.112.074801. arXiv: arXiv:1307.0895v2.

[174] P Seller et al. "Pixellated Cd(Zn)Te high-energy X-ray instrument." In: *Journal of instrumentation : an IOP and SISSA journal* 6.12 (2011). ISSN: 1748-0221. DOI: 10.1088/1748-0221/6/12/C12009.

[175] M. C. Veale et al. "HEXITEC: A High-Energy X-ray Spectroscopic Imaging Detector for Synchrotron Applications". In: *Synchrotron Radiation News* 31.6 (2018), pp. 28–32. ISSN: 0894-0886. DOI: 10.1080/08940886.2018.1528431.

[176] Kai Siegbahn. *Beta-And Gamma-Ray Spectroscopy*. 1st ed. North-Holland, 1955.

[177] K Bethge, G Walter, and B Wiedemann. *Kernphysik: Eine Einführung*. Springer-Lehrbuch. Springer Berlin Heidelberg, 2013. ISBN: 9783662080610.

[178] E Segrè. *Nuclei and particles: an introduction to nuclear and subnuclear physics*. W. A. Benjamin, 1977. ISBN: 9780805386011.

[179] B Povh et al. *Teilchen und Kerne: Eine Einführung in die physikalischen Konzepte*. Springer-Lehrbuch. Springer Berlin Heidelberg, 2013. ISBN: 9783642378225.

[180] G F Knoll. *Radiation Detection and Measurement*. John Wiley & Sons, 2010. ISBN: 9780470131480.

[181] C Grupen. *Teilchendetektoren*. BI-Wiss.-Verlag, 1993. ISBN: 9783411165711.

[182] K Kleinknecht. *Detektoren für Teilchenstrahlung*. Teubner Studienbücher Physik. Vieweg+Teubner Verlag, 2005. ISBN: 9783835100589.

[183] S. Agostinelli et al. "Geant4—a simulation toolkit". In: *Nuclear Instruments and Methods in Physics Research Section A: Accelerators, Spectrometers, Detectors and Associated Equipment* 506.3 (2003), pp. 250–303. ISSN: 0168-9002. DOI: 10.1016/S0168-9002(03)01368-8.

[184] J. Allison et al. "Geant4 developments and applications". In: *IEEE Transactions on Nuclear Science* 53.1 (2006), pp. 270–278. ISSN: 0018-9499. DOI: 10.1109/TNS.2006.869826.

[185] J. Allison et al. "Recent developments in Geant4". In: *Nuclear Instruments and Methods in Physics Research Section A: Accelerators, Spectrometers, Detectors and Associated Equipment* 835 (2016), pp. 186–225. ISSN: 0168-9002. DOI: 10.1016/J.NIMA.2016.06.125.

[186] Theresa Staufer. *All Geant4 simulations were set up and performed by Theresa Staufer*.

[187] G. Sarri et al. "Ultrahigh brilliance multi-MeV γ-ray beams from nonlinear relativistic thomson scattering". In: *Physical Review Letters* 113.22 (2014), p. 224801. ISSN: 10797114. DOI: 10.1103/PhysRevLett.113.224801.

[188] K. Poder et al. "Experimental Signatures of the Quantum Nature of Radiation Reaction in the Field of an Ultraintense Laser". In: *Physical Review X* 8.3 (2018), p. 031004. ISSN: 21603308. DOI: 10.1103/PhysRevX.8.031004. arXiv: 1709.01861.

[189] D. J. Corvan et al. "Optical measurement of the temporal delay between two ultrashort and focussed laser pluses". In: *Optics Express* 24.3 (2016), p. 3127. ISSN: 1094-4087. DOI: 10.1364/oe.24.003127.

[190] X. Llopart et al. "Medipix2: A 64-k pixel readout chip with 55-μm square elements working in single photon counting mode". In: *IEEE Transactions on Nuclear Science* 49 I.5 (2002), pp. 2279–2283. ISSN: 00189499. DOI: 10.1109/TNS.2002.803788.

[191] I. V. Khutoretsky. "Design of an optimal Ross filter system for x-ray spectra measurements in the range of 8.98-88 keV". In: *Review of Scientific Instruments* 66.1 (1995), pp. 773–775. ISSN: 00346748. DOI: 10.1063/1.1146285.

[192] Felix Horst et al. "A TLD-based ten channel system for the spectrometry of bremsstrahlung generated by laser-matter interaction". In: *Nuclear Instruments and Methods in Physics Research, Section A: Accelerators, Spectrometers, Detectors and Associated Equipment* 782 (2015), pp. 69–76. ISSN: 01689002. DOI: 10.1016/j.nima.2015.02.010.

[193] Y. J. Rhee et al. "Spectral tomographic analysis of Bremsstrahlung X-rays generated in a laser-produced plasma". In: *Laser and Particle Beams* 34.4 (2016), pp. 645–654. ISSN: 1469803X. DOI: 10.1017/S0263034616000604.

[194] D. J. Corvan, G. Sarri, and M. Zepf. "Design of a compact spectrometer for high-flux MeV gamma-ray beams". In: *Review of Scientific Instruments* 85.6 (2014), p. 065119. ISSN: 10897623. DOI: 10.1063/1.4884643.

[195] K. T. Behm et al. "A spectrometer for ultrashort gamma-ray pulses with photon energies greater than 10 MeV". In: *Review of Scientific Instruments* 89.11 (2018), p. 113303. ISSN: 10897623. DOI: 10.1063/1.5056248.

[196] H. Ding et al. "Nonlinear plasma wavelength scalings in a laser wakefield accelerator". In: *Physical review. E* 101.2-1 (2020), p. 023209. ISSN: 24700053. DOI: 10.1103/PhysRevE.101.023209. arXiv: 2001.09507.

[197] David H. Whittum et al. "Electron-hose instability in the ion-focused regime". In: *Physical Review Letters* 67.8 (1991), pp. 991–994. ISSN: 00319007. DOI: 10.1103/PhysRevLett.67.991.

[198] T. J. Mehrling et al. "Mitigation of the Hose Instability in Plasma-Wakefield Accelerators". In: *Physical Review Letters* 118.17 (2017), p. 174801. ISSN: 10797114. DOI: 10.1103/PhysRevLett.118.174801.

[199] A. Martinez De La Ossa, T. J. Mehrling, and J. Osterhoff. "Intrinsic Stabilization of the Drive Beam in Plasma-Wakefield Accelerators". In: *Physical Review Letters* 121.6 (2018), p. 064803. ISSN: 10797114. DOI: 10.1103/PhysRevLett.121.064803. arXiv: 1806.11352.

[200] T. Mehrling et al. "Transverse emittance growth in staged laser-wakefield acceleration". In: *Physical Review Special Topics - Accelerators and Beams* 15.11 (2012), p. 111303. ISSN: 10984402. DOI: 10.1103/PhysRevSTAB.15.111303.

[201] Alexander Aschikhin et al. "Analytical model for the uncorrelated emittance evolution of externally injected beams in plasma-based accelerators". In: *Nuclear Instruments and Methods in Physics Research, Section A: Accelerators, Spectrometers, Detectors and Associated Equipment* 909 (2018), pp. 414–418. ISSN: 01689002. DOI: 10.1016/j.nima.2018.02.065. arXiv: 1802.03968.

[202] L. L. Lucas and M. P. Unterweger. *Comprehensive Review and Critical Evaluation of the Half-Life of Tritium*. 2000. DOI: 10.6028/jres.105.043.

[203] K. Nakamura et al. "Electron beam charge diagnostics for laser plasma accelerators". In: *Physical Review Special Topics - Accelerators and Beams* 14.6 (2011). ISSN: 10984402. DOI: 10.1103/PhysRevSTAB.14.062801.

[204] J. Andruszkow et al. "First observation of self-amplified spontaneous emission in a free-electron laser at 109 nm wavelength". In: *Physical Review Letters* 85.18 (2000), pp. 3825–3829. ISSN: 00319007. DOI: 10.1103/PhysRevLett.85.3825. arXiv: 0006010 [physics].

[205] W. Ackermann et al. "Operation of a free-electron laser from the extreme ultraviolet to the water window". In: *Nature Photonics* 1.6 (2007), pp. 336–342. ISSN: 17494885. DOI: 10.1038/nphoton.2007.76.

[206] S. Schröder et al. "Tunable and precise two-bunch generation at FLASHForward". In: *4th European Advanced Accelerator Concepts Workshop*. 2020. arXiv: 2005.12071 [physics.acc-ph].

[207] B. Hidding et al. "Ultracold electron bunch generation via plasma photocathode emission and acceleration in a beam-driven plasma blowout". In: *Physical Review Letters* 108.3 (2012). ISSN: 00319007. DOI: 10.1103/PhysRevLett.108.035001.

[208] F. Li et al. "Generating high-brightness electron beams via ionization injection by transverse colliding lasers in a plasma-Wakefield accelerator". In: *Physical Review Letters* 111.1 (2013). ISSN: 00319007. DOI: 10.1103/PhysRevLett.111.015003. arXiv: 1301.2950.

[209] A. Martinez De La Ossa et al. "High-quality electron beams from beam-driven plasma accelerators by wakefield-induced ionization injection". In: *Physical Review Letters* 111.24 (2013). ISSN: 00319007. DOI: 10.1103/PhysRevLett.111.245003. arXiv: 1309.1900.

[210] G. Wittig et al. "Optical plasma torch electron bunch generation in plasma wakefield accelerators". In: *Physical Review Special Topics - Accelerators and Beams* 18.8 (2015). ISSN: 10984402. DOI: 10.1103/PhysRevSTAB.18.081304.

[211] A. Martinez De La Ossa et al. "Optimizing density down-ramp injection for beam-driven plasma wakefield accelerators". In: *Physical Review Accelerators and Beams* 20.9 (2017). ISSN: 24699888. DOI: 10.1103/PhysRevAccelBeams.20.091301.

[212] C. A. Lindstrøm et al. "Matching small β functions using centroid jitter and two beam position monitors". In: *Physical Review Accelerators and Beams* 23.5 (2020), p. 052802. ISSN: 24699888. DOI: 10.1103/PhysRevAccelBeams.23.052802. arXiv: 2002.06022.

[213] C. A. Lindstrøm et al. "Emittance Preservation in an Aberration-Free Active Plasma Lens". In: *Physical Review Letters* 121.19 (2018). ISSN: 10797114. DOI: 10.1103/PhysRevLett.121.194801. arXiv: 1808.03691.

[214] Gregor Loisch et al. “Observation of High Transformer Ratio Plasma Wakefield Acceleration”. In: *Physical Review Letters* 121.6 (2018). ISSN: 10797114. DOI: 10.1103/PhysRevLett.121.064801.

[215] Lucas Schaper et al. “Longitudinal gas-density profilometry for plasma-wakefield acceleration targets”. In: *Nuclear Instruments and Methods in Physics Research, Section A: Accelerators, Spectrometers, Detectors and Associated Equipment* 740 (2014), pp. 208–211. ISSN: 01689002. DOI: 10.1016/j.nima.2013.10.052.

[216] J. van Tilborg et al. “Density characterization of discharged gas-filled capillaries through common-path two-color spectral-domain interferometry”. In: *Optics Letters* 43.12 (2018), p. 2776. ISSN: 0146-9592. DOI: 10.1364/ol.43.002776.

Acknowledgements

After all these years it now is time to thank all the people who helped to finish this document and the work described in it. First of all, I want to thank **Jens** for supervising me and helping me, whenever I was stuck and **Brian** for helping to make this thesis a readable and understandable document and **Bernhard** for giving useful advice whenever needed.

I also want to thank **Matt**, **Charlie**, and **John** for designing and setting up the initial experiment, **JP** for helping me to get it to run and **Theresa** and **Martin** for helping to transition it into a turn-key system (and shots on Friday). Many thanks to **Kris** for doing a great job at running 28m and helping me with basically every aspect of the thesis, **Carl** for his infinite wisdom and being a great neighbour in the office, **Jon** for sharing his insight regarding plasmas and X-rays, **Theresa** for fruitful discussions about the theory of Thomson scattering and all of the people mentioned here for good times outside the lab.

The experiments described here would certainly not have been possible without **Kai**, **Andre**, and **Amir**, who helped us to design, build, and maintain the infrastructure in our labs. Thanks to **Sven** and **Sandra** for rescuing servers and installing countless cameras, to **Vladimir** for reviving to DAQ so many times, **Maik** for looking after the laser and making sure we could use it for our experiments and **Iris** for making sure the people in the group look after one another.

I also want to say thanks to all the people from FLA who made the group such a great working environment. Especially **Richard** who trained me in brewing enough beer to survive the stressful PhD life and introduced me to the world of craft beer together with **Sasha** and **Stephan**. I am looking forward to Corona-free times when pub crawls on Saturday afternoons will finally be possible again and the entire group can meet in a bar. I also want to thank **Gabi** for the good times at football and in the lab. Sometimes standing in the cold rain all evening is all it takes to be reminded that there are worse things than being a physicist.

Of course I also want to thank **Jann** for the good times as a roommate throughout the entire undergrad. Without our excellent teamwork, I would probably not have made it this far in my physics studies.

Finally I want to thank my family; my siblings **Hanna**, **Lars**, and **Maren**, their families and especially my parents **Gerd** and **Heike**, who always supported me. And of course I want to thank **Birte**, whose loving support helped me to stay calm in stressful times and always listened to my boring explanations.

Eidesstattliche Versicherung / Declaration on oath

Hiermit versichere ich an Eides statt, die vorliegende Dissertationsschrift selbst verfasst und keine anderen als die angegebenen Hilfsmittel und Quellen benutzt zu haben.

Die eingereichte schriftliche Fassung entspricht der auf dem elektronischen Speichermedium.

Die Dissertation wurde in der vorgelegten oder einer ähnlichen Form nicht schon einmal in einem früheren Promotionsverfahren angenommen oder als ungenügend beurteilt

Hamburg, den 06.10.2020

Simon Bohlen